Review

Black TiO$_2$ Nanomaterials: A Review of Recent Advances

Sanjay Gopal Ullattil[a,b], Soumya B. Narendranath[c], Suresh C. Pillai[d,e,*], Pradeepan Periyat[a,*]

[a] Department of Chemistry, University of Calicut, Kerala 673 635, India
[b] Department of Nanoscience & Technology, University of Calicut, Kerala 673 635, India
[c] Department of Chemistry, Central University of Kerala, 671 314, India
[d] Centre for Precision Engineering, Materials and Manufacturing Research (PEM), Institute of Technology Sligo, Ash Lane, Sligo, Ireland
[e] Nanotechnology and Bio-Engineering Research Group, Department of Environmental Science, School of Science, Institute of Technology Sligo, Ash Lane, Sligo, Ireland

HIGHLIGHTS

- Advances in the synthesis of black TiO$_2$ nanomaterials are described.
- Structure, morphology, electronic structure and their diverse applications are described.
- Presence of defects and their applications in various technological fields are explained.
- Uses in solar photocatalytic water splitting are explained in detail.

GRAPHICAL ABSTRACT
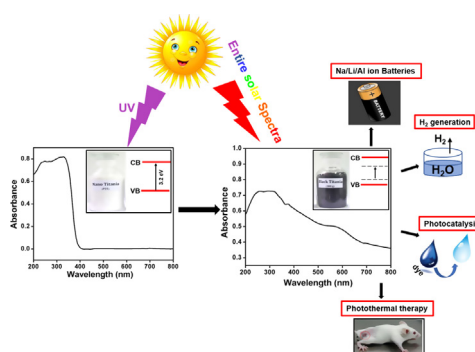
ARTICLE INFO

ABSTRACT

Recently reported black TiO$_2$ nanomaterials are the unequivocally accepted sun light harvesters which facilitate the maximum solar energy absorption from ultraviolet (UV) to infrared (IR) region of the solar spectrum due to their improved optical absorption properties in comparison to the normal white TiO$_2$. The recent advancement in black TiO$_2$ nanomaterials explicitly proved that the structural and morphological features along with the suitable electronic properties are being extensively utilized in many areas of research. The current review focuses on the various synthetic routes for black TiO$_2$ nanomaterials, their structure, morphological variations, electronic structure and their diverse applications related to environmental and technological fields such as photodegradation of organic pollutants, photocatalytic water splitting, dye sensitized solar cells, batteries, super capacitors and photothermal therapy.

1. Introduction

The maximum utilization of renewable energy resources such as sun light, wind, biomass, rain, tides and waves are required to address the energy demand of 21st century [1,2]. Among these renewable sources, solar energy is quite important because sun is the ubiquitous energy source and solar energy is available abundantly with free of cost [3,4].

Diverse pathways that could easily harvest the sunlight to encounter the future energy demands generated significant interest among the scientific community [5,6]. Harnessing the abundant sunlight falling on earth has been a constant challenge to mankind. In this scenario, nanomaterial architectures for solar energy conversion play an important role in harvesting the sunlight. Materials with smaller particle size inhibits the recombination probability of photogenerated electrons and

---

holes on its surface therebyfacilitating their smooth transport. In addition, nanoparticles possess high surface area which contains more active sites on the surface [6]. Among the various nanomaterials reported so far, TiO_2 is the most promising light harvesting material that has been widely investigated [1–10]. The light harvesting potential of white TiO_2 has been experimentally manifested in the fields of photodegradation [7–10], dye sensitized solar cells [11–14], self-cleaning coatings [15–19], solar water splitting [20–25], organic reactions [26–29], photocatalytic sensors [30–35] etc. TiO_2 has been widely accepted as a light harvester because of its chemical and thermal stability, high refractive index, nontoxicity, and wide band gap energy [36–42]. A good portion of the sun's radiation is in the visible (43%) and infra red (52%) range with 5% in ultra violet region [43]. A colorless/white material can only absorb energy from the UV region. Pure TiO_2 is a colorless white crystalline solid which absorbs in the UV region only [44], researchers have imposed doping on TiO_2 for the improvement of its wavelength absorption from UV to visible region [1–10]. Metal doping in TiO_2 nanomaterials generated secondary impurities (*e.g.* Al_2TiO_5, $CeTi_4O_{24}$ and $Ce_2Ti_2O_7$). Presence of these impurity phases decreased the crystallinity of TiO_2 which in turn reduced the efficiency [45] and photocatalytic activity of the material [1–46]. Non-metal doping has also been investigated widely for better light absorption. The light harvesting process using non-metal doped TiO_2 has been successfully implemented without developing any impurity phases after the annealing process [47–50]. However, non-metal doped TiO_2 structures were incapable of absorbing IR region which covers 52% of the solar spectrum [1–51]. In order to harvest sunlight more effectively blue [52–60], yellow [61,62], brown [63,64] red [65–67] and grey [68–70] TiO_2 have also been reported. However, they all possessed limited or even zero absorption in the IR region of the solar spectrum.

In 1950′s Cronzmeyer and Gilleo compared the optical absorption characteristics of bare and hydrogenated rutile single crystals [71]. The hydrogenated rutile became blue in color by extending its absorption from visible to IR region of the electromagnetic spectra. Afterwards extensive works had been carried out to utilize the wide optical absorbance features of TiO_2 which led to the developments of black TiO_2, an ultimate solar light absorber [72–76]. Black TiO_2 is first produced when white TiO_2 was heated at 200 °C under 20.0 bar hydrogen pressure for 5 days by Chen et al. in 2011 [77]. After this discovery of black TiO_2 nanoparticles, the synthesis of black TiO_2 nanostructures for energy applications is found to be a hot area in the current environmental perspective [78]. The current review addresses the latest developments in black TiO_2 nanomaterials. Various synthetic aspects of black TiO_2 nanomaterials and characterization techniques to probe its structural, morphological and optical properties were surveyed. The theoretical basis of color change in black TiO_2 nanomaterials and its correlation with the optical absorption features were discussed in detail. This review gave great emphasis on various functional applications of black TiO_2 nanomaterials [77–192].

1.1. What is black TiO_2?

Pure TiO_2 has a white color with a band gap of 3.0–3.2 eV [79]. The wide band gap in TiO_2 inhibits the proper utilization of entire solar spectrum. Diverse methodologies have been tested for improving the optical and electronic properties of TiO_2, *viz*, dopin [80], dye sensitization [80], metal organic frame works [81], TiO_2 composites [82] etc. All these strategies could red shift the absorption edge of TiO_2, but these modifications on TiO_2 could not harvest the entire solar energy falling on earth. White TiO_2 turns black on reduction through various methods. Presence of Ti^{3+} through self-doping, surface hydroxyl groups, oxygen vacancies and Ti-H bonds in black TiO_2 consequent to the structural modifications were responsible for the black coloration as well as the superior optical, electronic and catalytic properties [83]. As shown in Fig. 1, black TiO_2 nanomaterial has the potential to absorb the entire range of solar spectra.
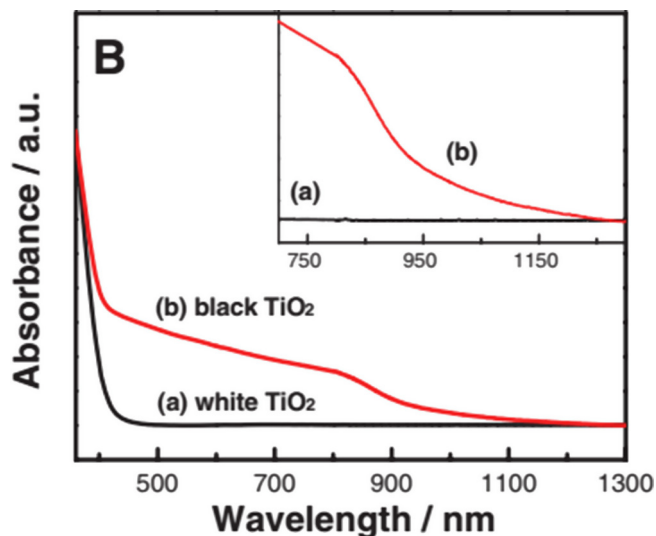

Fig. 1. Absorbance spectra of a) white TiO_2 and b) black TiO_2. Inset shows the extended absorption of black TiO_2 [77]. Reprinted with permission from Ref. [77]. Copyright 2011 AAAS.

Lattice disorder is introduced in the formation of black TiO_2 which has resulted in the creation of mid gap energy levels within the band gap. The wide range of absorption in these nanoparticles consequent to this mid-gap energy levels distribution is the key factor for the optical and catalytic activity.

2. Synthesis of black TiO_2 nanostructures

Different strategies have been employed for the synthesis of black TiO_2 nanomaterial towards various functional applications [77–192]. To date, hydrogenation is the widely used method for synthesizing black TiO_2. High/low pressure hydrogen treatment, hydrogen-argon treatment, hydrogen-nitrogen treatment, argon treatment, hydrogen plasma treatment, electrochemical reduction, chemical oxidation/reduction, hydroxylation and pulsed laser ablation are the main synthetic methods carried out so far. Even though Hydrogenation has been the most employed method for synthesizing black TiO_2, all those hydrogenation. procedures were not ended in black TiO_2 [68,69].

2.1. High/low pressure hydrogen treatment

Synthesis of black TiO_2 was first reported by Chen et al. using hydrogenation of crystalline TiO_2 at a high pressure of 20 bar [77]. The synthesized white TiO_2 nanocrystals were hydrogenated in a 20 bar H_2 atmosphere at 200 °C for 5 days [77]. The reduction in effective band gap was (Fig. 2A) due to the disordered layer on the surface of black TiO_2 induced by hydrogenation, which was beneficial for carrier trapping. The extended disorder present in the nanocrystal creates mid-gap states, instead of discrete donor levels, which will effectively overlap with the conduction band edge. The crystalline state of pristine TiO_2 and the disordered surface of black TiO_2 (Fig. 2B) were also visible from HRTEM images (Fig. 2C and D) [77].

Sun et al. reported the hydrogen incorporation into anatase TiO_2 nanocrystals under high hydrogen pressure and they obtained hydrogenated black TiO_2-(1 0 1) [84]. They synthesized anatase TiO_2 nanocrystals predominantly having (0 0 1) and (1 0 1) separately. Hydrogen adsorption and desorption properties were analyzed by an automated Sievert's apparatus. TiO_2 with (1 0 1) and (0 0 1) surfaces have a hydrogen storage capacity of 1.4% and 1.0% respectively as represented in Fig. 3. Computational calculations based on DFT theory showed that hydrogen occupied the voids created by adjacent titanium-oxygen octahedra and hydrogen incorporation through the anatase (1 0 1) surface
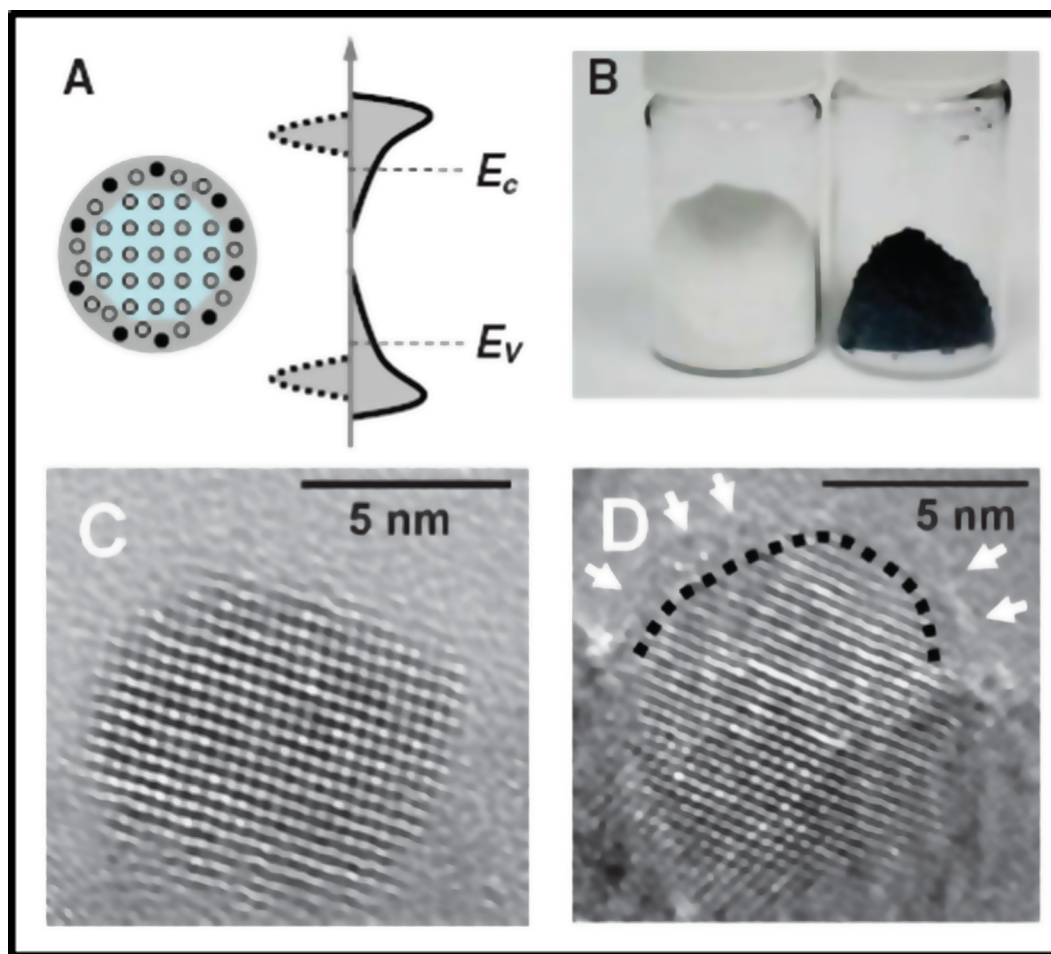
Fig. 2. A) Structure and electronic DOS of black TiO_2 B) photographs of white and black TiO_2 C) HRTEM of TiO_2 and D) disordered black TiO_2 [77]. Reprinted with permission from Ref. [77]. Copyright 2011 AAAS.

is favorable than that of (0 0 1) (Fig. 4) [84].

Leshuk et al. reported hydrogenation of pristine TiO_2 nanoparticles at different temperatures. The color change and a large wavelength absorption was observed for sample hydrogenated at 450 °C under 20 bar pressure for 24 h [85]. The color change observed and the corresponding absorption change (Tauc Plot) are shown in Fig. 5.

All the above methods were carried out at elevated temperatures ranges from 200 to 450 °C under high hydrogen pressure of 20 bar. However, Lu et al. experimented to synthesize black TiO_2 nanoparticles at ambient temperature under high-pressure H_2 treatment on commercial P25 and examined the color change of these TiO_2 nanoparticles over time (0–20 days) [86]. The color of commercial P25 turned to

black after 20 days of hydrogenation (Fig. 6). The optical absorption onset of this black TiO_2 nanoparticle was about 1.0 eV lower compared to P25 [86].

Wang et al. reported the synthesis of black TiO_2 by hydrogenation of rutile TiO_2 nanowire arrays under ultrahigh pure hydrogen atmosphere for 3 h at 200–550 °C [87]. The color of the hydrogenated rutile TiO_2 nanowires turned to yellowish green at 350 °C and black at 450 °C. This hydrogenated rutile TiO_2 nanowires had visible light absorption because of hydrogen treatment [87].

Naldoni et al. attempted to synthesize black TiO_2 nanoparticles by heating amorphous TiO_2 under H_2 flow, followed by rapid cooling in an inert environment [88]. Here they pretreated TiO_2 powder under
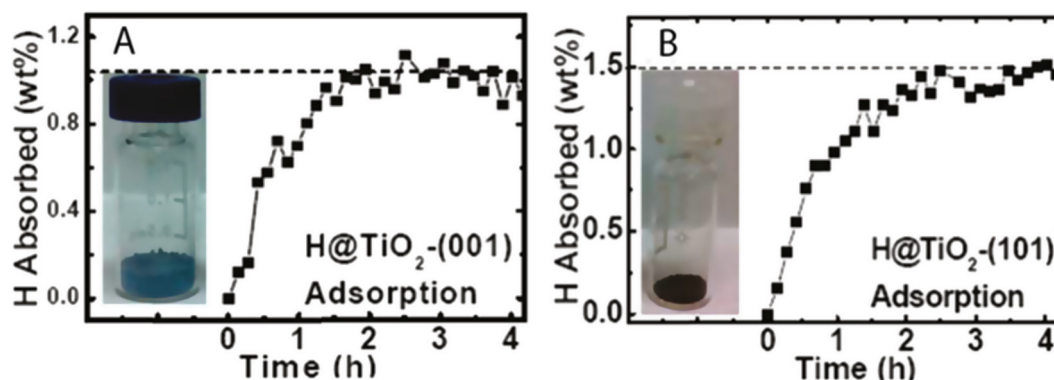

Fig. 3. Hydrogen adsorption profile for A) TiO_2 (0 0 1) and B) TiO_2 (1 0 1) [84]. Reprinted with permission from Ref. [84]. Copyright 2015, American Chemical Society.
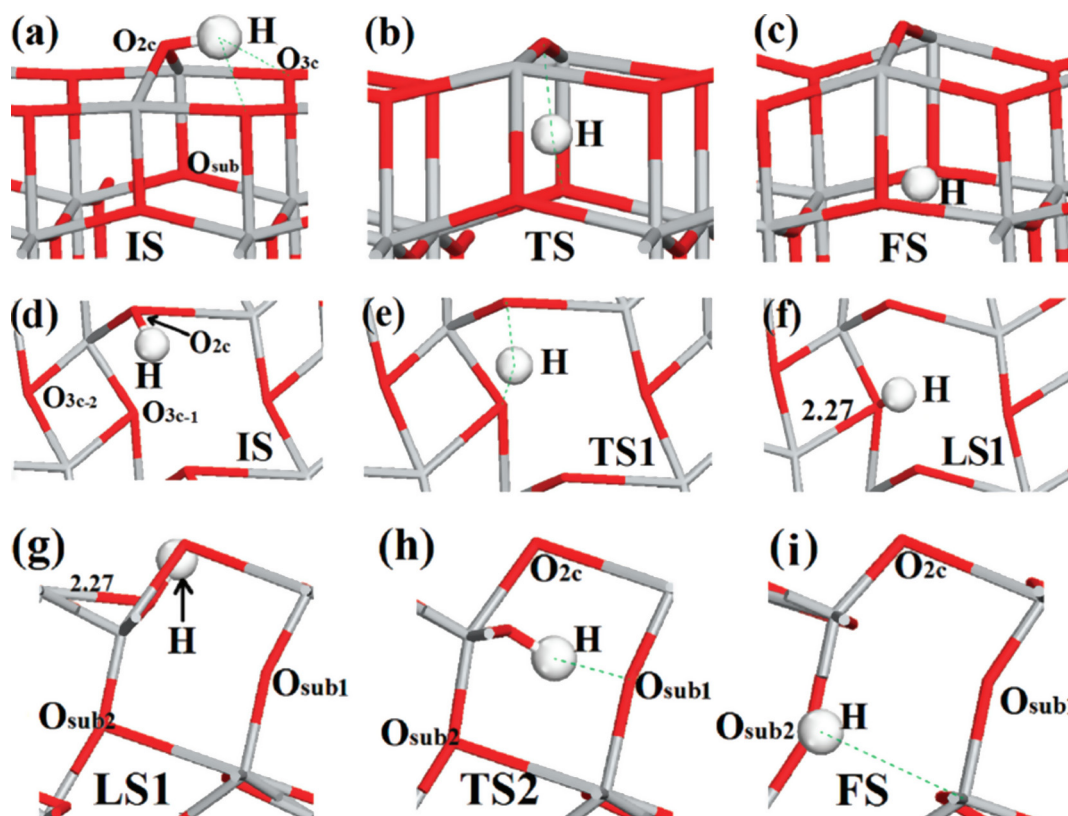
Fig. 4. Optimized geometries of initial, transition, and final states for: (a–c) hydrogen incorporation into anatase TiO$_2$(0 0 1) (side views); (d–f) hydrogen diffusion from O2c to O3$_{c-1}$ on the anatase (1 0 1) surface (top views); (g-i) hydrogen incorporation *via* diffusion from O3$_{c-1}$ to O$_{sub2}$ through the (1 0 1) surface (side views). Titanium and oxygen are presented with sticks and hydrogen with white spheres [84]. Reprinted with permission from Ref. [84]. Copyright 2011, American Chemical Society.
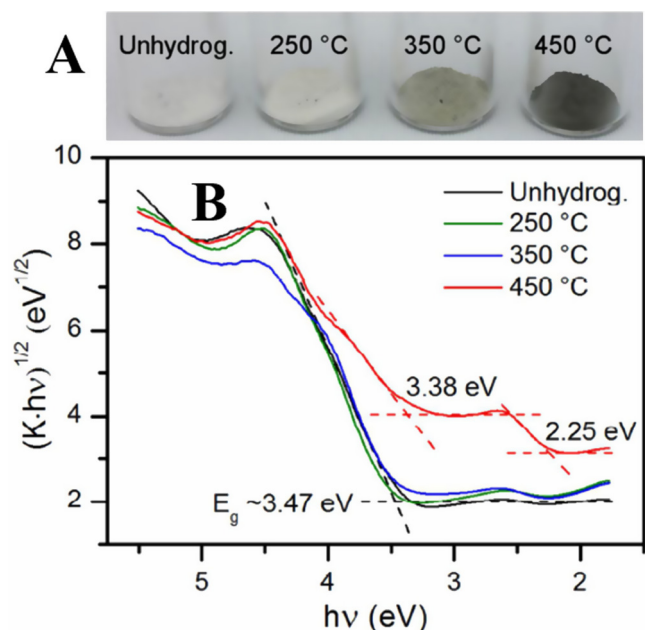

Fig. 5. A) Photographs of TiO$_2$ before and after 24 h hydrogenation at 250, 350 and 450 °C with B) the corresponding Tauc plot [85]. Reprinted with permission from Ref. [85]. Copyright 2013, American Chemical Society.

vacuum followed by heat treatment at 200 °C for 1 h under O$_2$ atmosphere and subsequent reduction at 500 °C for 1 h in hydrogen atmosphere. The amorphous precursor is more viable for black TiO$_2$ with large wavelength absorption compared to that of the crystalline precursors such as P25 [88]. In a similar method, Zhang et al. also employed hydrogenation to obtain the mesoporous black TiO$_2$ nanosheets by using a biotemplate (Typha angustifolia). This scheme is represented in Fig. 7 [89]. Liu et al. reported the synthesis of black TiO$_2$ nanomaterials using anatase TiO$_2$ nanotubes as precursor [90].

2.2. Hydrogen-Argon treatment

Another method of synthesis of black TiO$_2$ was using Hydrogen-Argon treatment. Leshuk et al. compared the color change of TiO$_2$ nanoparticles obtained after reduction under pure H$_2$ and H$_2$-Ar mixture. They inferred that the color change depended upon the preparation methods of precursors [91]. Various anatase nanomorphologies were hydrogenated by Lu et al. under H$_2$-Ar mixture at 450 °C for 1 h [92].

Sinhamahapatra et al. developed a controlled magnesiothermal reduction to synthesize reduced black TiO$_2$ under H$_2$/Ar atmosphere [93]. The material possessed remarkable improved progress in the visible and infrared absorption features. Here the commercially available nano anatase TiO$_2$ was treated under different concentration of Mg followed by 5% H$_2$/Ar treatment to obtain black TiO$_2$ [93].

2.3. Argon-Nitrogen treatment

TiO$_2$-B (TiO$_2$-B structure is comprised of edge- and corner-shared TiO$_6$ octahedra. In fact, TiO$_2$-B could be seen as distorted octahedra structure) nanoparticles were also converted into black TiO$_2$ in an Ar-N$_2$ environment [94]. The monodispersed TiO$_2$-B particles obtained by the hydrolysis of TiCl$_4$ in ethylene glycol were suspended in methanol (20 mL) and then subjected to irradiation under UV light in a sealed container with constant bubbling of N$_2$, turning the solution black in color. The black TiO$_2$-B nanoparticles were obtained by heating the solid product obtained in the above process at 340 °C in Ar atmosphere for 2 h [94]. Wei et al. reported a core-shell black anatase TiO$_2$ with a
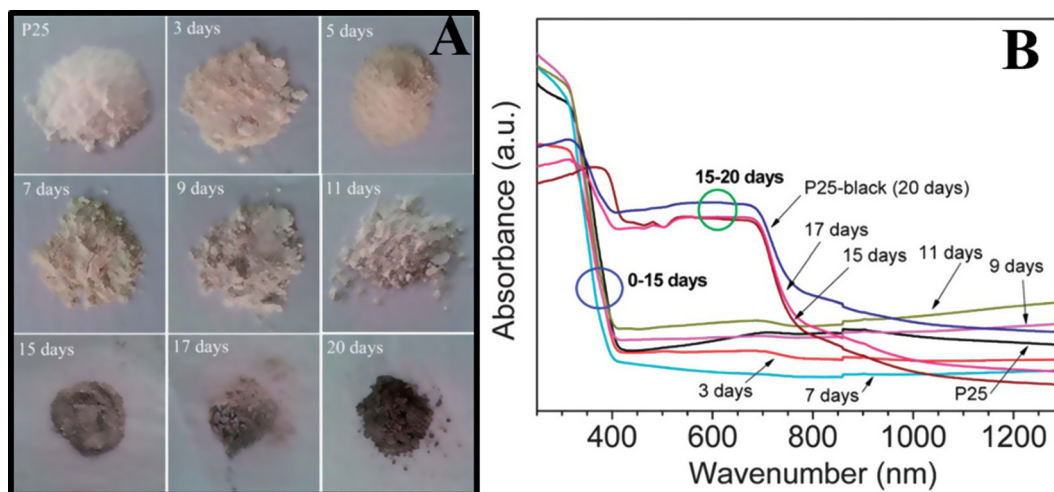
Fig. 6. Photographs of Black TiO_2 synthesized at room temperature under high-pressure H_2 atmosphere and their corresponding absorption spectrum [86]. Reprinted with permission from Ref. [86]. Copyright 2014, Royal Society of Chemistry.
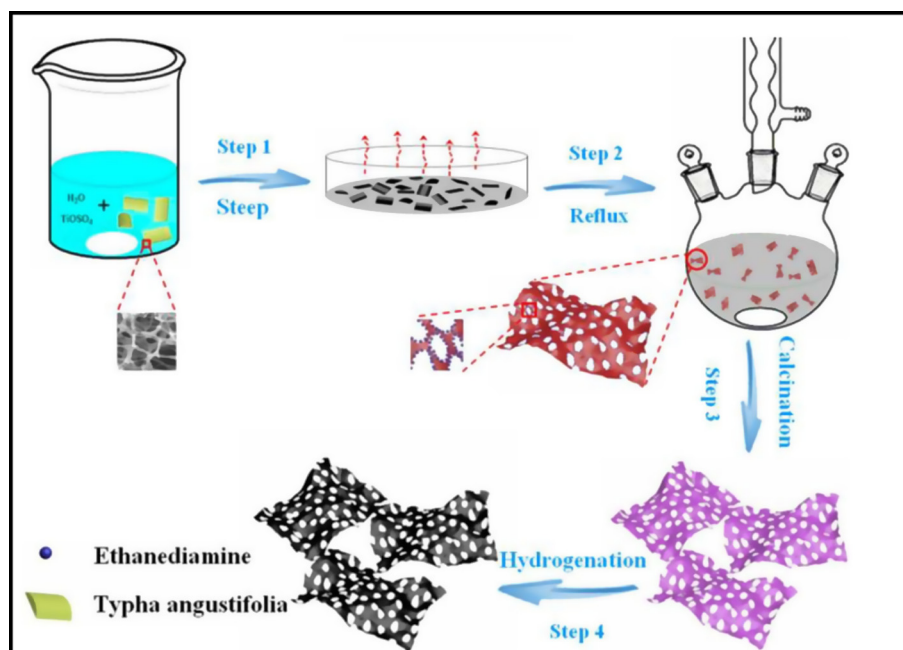

Fig. 7. Schematic representation of synthesis of black TiO_2 nanosheets using a biotemplate (Typha angustifolia) [90] Reprinted with permission from Ref. [90]. Copyright 2016, Royal Society of Chemistry.

high concentration of Ti^{3+} and oxygen vacancy defects by a one-pot synthetic method *viz.* calcination of colloidal TiO_2 precursor under N_2 atmosphere alone. (Fig. 8) [95].

2.4. Hydrogen-Nitrogen treatment

Zhu et al. manipulated black TiO_2 through hydrogen spill in a H_2-N_2 atmosphere at 200–700 °C [96]. They hydrogenated platinum impregnated P25 (Pt-P25) under H_2-N_2 mixture. It could be observed that the reduction started from 160 °C. Further increase in temperature up to 750 °C causes a color change into black due to the hydrogen spillover from Pt to TiO_2. Wu et al. prepared black TiO_2 nanoparticles by combining the sol-gel strategy and H_2-N_2 treatment. Sol-gel derived nanocrystalline TiO_2 was treated under H_2:N_2 environment to obtain black TiO_2 [97]. Thermal treatment at different temperatures (110, 130, 150, 170, 190 and 210 °C) on protonated titanate nanotubes under H_2-N_2 atmosphere resulted to a series of nanotubes and nanobelts [98]. The nanotube morphology was retained at temperature ≤150 °C and above

that temperature, the morphology was changed to nanobelts along with the phase change from anatase to TiO_2-B [98].

2.5. Argon treatment

Zhang et al. reported Ar treatment of sol-gel derived Ni doped TiO_2 leading to the formation of black TiO_2 nanoparticles [99]. The black TiO_2 precursor (Ni doped TiO_2) was mixed with 2 g of $NaBH_4$ and heated at 350 °C under Ar atmosphere for 1 h. Finally allowed to cool naturally until it reaches room temperature. The color of the Ni doped TiO_2 nanoparticles was yellowish. The various samples such as 0, 1.0, 2.0, 3.0, and 4.0 mol% of Ni were denoted as M0, M1, M2, M3, and M4 respectively. These materials are turned from yellowish to black when treated under Ar atmosphere and were denoted as b-M0, b-M1, b-M2, bM3, and b-M4, respectively. The change in color and absorbance spectra along with the Tauc plot before and after 2 mol% Ni doping and Ar treatment are shown in Fig. 9 [99]. Grabstanowicz et al. prepared black TiO_2 powders using a two-step strategy [100]. The Ti precursor
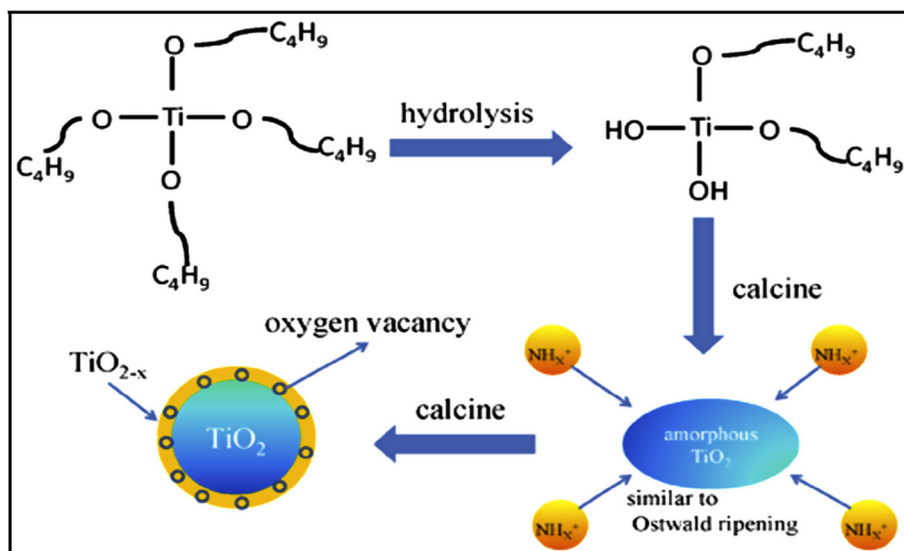
Fig. 8. Formation mechanism of core shell black TiO_2 nanoparticles by calcination of colloid titania precursor (resulted by the hydrolysis of Tetrabutyl titanate and urea mixture) under N_2 flow at atmospheric pressure [95]. Reprinted with permission from Ref. [95]. Copyright 2017 Elsevier.

used was TiH_2 and it was mixed with H_2O_2 to get a slurry. Further the slurry turned yellow on vacuum dessication and drying at 100 °C and finally the yellow powder was heated at 630 °C for 3 h in Ar atmosphere to obtain the black rutile TiO_2 possessed markedly increased absorption in the visible and near-infrared regions [100]. Myung et al. reported hydrogenation under Ar treatment for the synthesis of black TiO_2 by annealing a yellow TiO_2 gel at 400–600 °C for 5 h [101].

2.6. Plasma treatment

Wang et al. prepared hydrogenated black TiO_2 nanoparticles by hydrogen plasma in a thermal plasma furnace using 200 W plasma input power on commercial P25 sample [102]. This hydrogenated black TiO_2 nanoparticles had a notable absorption characteristics in the visible and near infrared region (Fig. 10) [102].

Teng et al. manipulated black TiO_2 nanotubes by hydrogen plasma assisted chemical vapor deposition with hydrogen as reaction gas [103]. Precursor TiO_2 was subjected to heat at 350–500 °C for 3 h under the hot filament (2000 °C) resulted in black colored TiO_2 nanotubes [103]. This method was also used by Yan et al. [104] where the
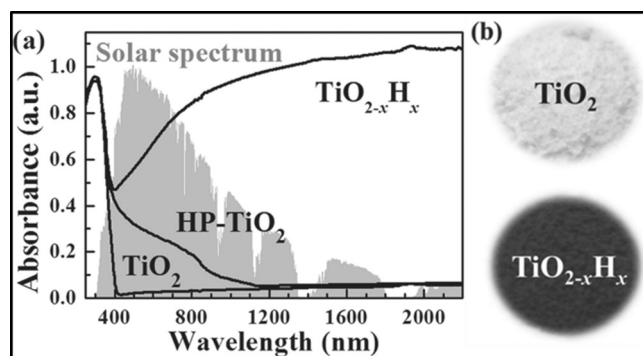

Fig. 10. (a) Absorption spectra of TiO_2, high pressure hydrogenated TiO_2 (HP-TiO_2) and H_2 plasma reduced black TiO_2 ($TiO_{2-x}H_x$) (b) photographs of pristine TiO_2 and $TiO_{2-x}H_x$ [102]. Reprinted with permission from Ref. [102]. Copyright 2014, Wiley-VCH.

processing was carried out at 390 °C for 3 h with the inductively coupled plasma power with H_2 flow. The black TiO_2 nanoparticles obtained had enhanced visible light absorption characteristics [104]. The same group have also employed H_2 plasma treatment on Degussa-P25 drop
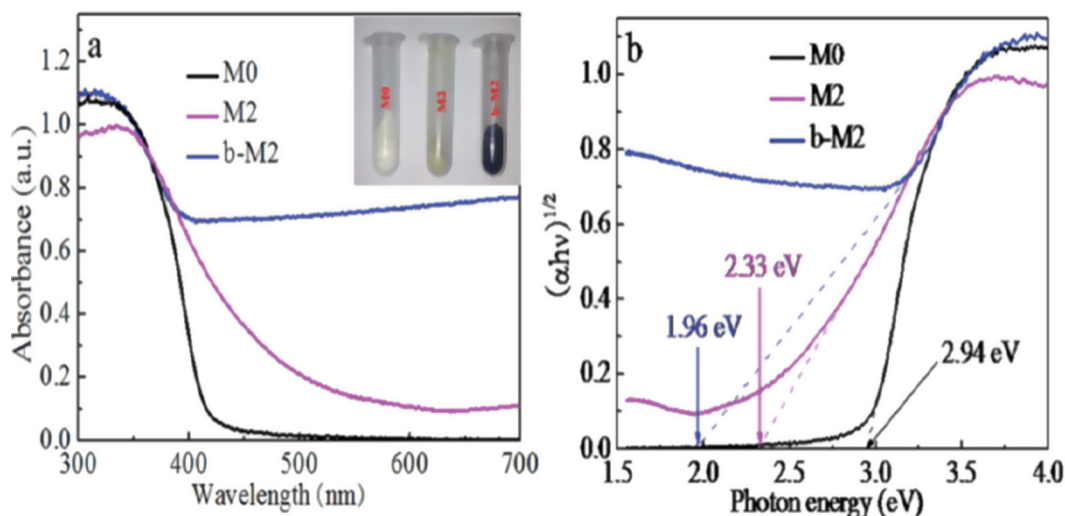

Fig. 9. (a) UV–vis diffuse reflectance absorption spectra of M0, M2, and b-M2 samples, respectively, and (b) corresponding Tauc plot of M0, M2, and b-M2 samples, respectively [99]. Reprinted with permission from Ref. [99]. Copyright 2015, Royal Society of Chemistry.

casted on a silicon wafer and heated at 150 °C for 20 min [105]. The TiO_2 obtained was found black with a good visible wavelength area absorption [105]. Panomsuwan et al. prepared a black $H-TiO_{2-x}$ with plasma generated inside water between two metallic Ti electrodes, which were subjected to high frequency bipolar high voltage pulses [106]. Initially the electrode surface got oxidized by the OH^- and O^{2-} produced from water plasma. Further the bombardment with the atomic hydrogen resulted in black TiO_2. The process was considered as a green route to black TiO_2 [106]. Black TiO_2 nanoparticles were also reported by applying microwave induced plasma over a water soluble titanium complex $(NH_4)_6$ $[Ti_4(C_2H_2O_3)_4(C_2H_3O_3)_2(O_2)_4O_2].4H_2O$ [107].

2.7. NaBH₄ reduction

Kang et al. implemented a chemical reduction for the synthesis of black TiO_2 using $NaBH_4$ [108]. The reduction of TiO_2 nanotube had been carried out with 0.1 M $NaBH_4$ solution at room temperature for an hour. The reduced black TiO_2 nanotubes had strong absorption extending up to near-infrared [108]. Tan et al. employed a solid state synthesis route for black TiO_2. P25 (Anatase and Rutile) was ground thoroughly with $NaBH_4$ and the mixture was heated in a tubular furnace under Ar atmosphere at 300–400 °C for different time intervals up to 1 h. While cooling to room temperature different colored TiO_2 core-shell nanoparticles were obtained (Fig. 11) [109].

2.8. Metal reduction

Black TiO_2 nanoparticles could be synthesized through reduction with various metals. Aluminum, zinc and magnesium are identified as reducing agents to obtain black TiO_2. Wang et al. used Al as a reducing agent in an evacuated two-zone vacuum furnace at 300–500 °C [110]. The driving force behind the formation of black TiO_2 is the release of oxygen from pre-annealed TiO_2 to molten aluminum so that oxygen vacancies are created on TiO_2. In a typical procedure, pre-annealing of aluminum was done at 800 °C for 6 h and that of pristine TiO_2 was done at 500 °C for 20 h respectively. Further the post annealing was carried out at 800 and 900 °C for 12 h respectively. These reduced TiO_2 nanoparticles had black color and traversed absorption through visible-light to near-infrared regions (Fig. 12).

Cui et al. prepared black anatase TiO_2 nanotubes by a similar method in which they used an anodized Ti foil as precursor for Ti [111]. Ti foil was anodized in a mixture of ethylene glycol, 0.4 wt% NH_4F and 3 wt% H_2O under 100 V for 5 min. resulting in TiO_2 nanotubes. The first layer was removed followed by calcination at 500 °C for 4 h in air. The synthesized TiO_2 nanotubes and aluminum powders were heated at 500 and 850 °C in such a way that TiO_2 releases oxygen to molten aluminum

to get reduced black TiO_2. The black anatase TiO_2 nanotubes had extended absorption from visible-light to near infrared regions [111].

Zhi et al. proposed another method for the synthesis of black TiO_2 where the white TiO_2 and aluminum metal were placed separately in a two-zone tube furnace and then evacuated to a base pressure lower than 0.5 Pa where TiO_2 and aluminum were heated for 6 h at 500 and 800 °C respectively under NH_3 atmosphere. After cooling to room temperature, black TiO_2 powders were formed [112]. Lin et al. synthesized a set of nonmetal-doped black TiO_2 with a more or less similar two-step strategy [113]. Here Al reduction was first carried out to introduce oxygen vacancies on the amorphous surface layer over the crystalline core of TiO_2 (Degussa P25) and then nonmetal elements such as H, N, S and I were introduced into the oxygen-deficient amorphous layers of Al-reduced TiO_2 nanocrystals (TiO_{2-x}) paved the way to color change. All these non-metal doped black TiO_2 nanoparticles have shown large wavelength absorption extended up to near-infrared region (Fig. 13) [113].

2.9. ZnCl₂/KCl molten salt assisted synthesis

In this method black TiO_2 hexagonal nanosheets were manipulated by mixing TiH_2 with a eutectic composition of $ZnCl_2/KCl$ melt followed by grinding with ethanol for homogenization [114]. The homogenized powder was heated at 400 °C for 3 h. The product was cooled and dried to get black TiO_2. When the calcination temperature changes from 400, 450 to 500 °C, the morphology was changed from nanosheets, nanotubes and finally to nanorods [114].

2.10. Microwave assisted manganese reduction

Oxygen rich yellow anatase with visible light absorption and oxygen vacancy rich black anatase TiO_2 with NIR absorption have been synthesized [115]. In this method a sol has been synthesized using titanium butoxide, manganese acetate and water as precursors. Doping and hydroxylation were carried out simultaneously during the sol preparation and the sol was then put through microwave irradiation at 150 °C with stirring speed of 1200 rpm for 5 min followed by drying at 80 °C to obtain black anatase TiO_2 nanomaterials (Fig. 14).

2.11. Solvothermal synthesis

Shah et al. employed ascorbic acid as both reductant and structure directing agent to synthesis black TiO_2 [116]. Here different amounts of aqueous solution of L-ascorbic acid added to $TiCl_3$ and the pH was maintained to be 4 by adding NaOH solution. The mixture was heated at 180 °C for 12 h in an autoclave [116]. A one step solvothermal method for the synthesis of black TiO_2 on Ti foils with visible light
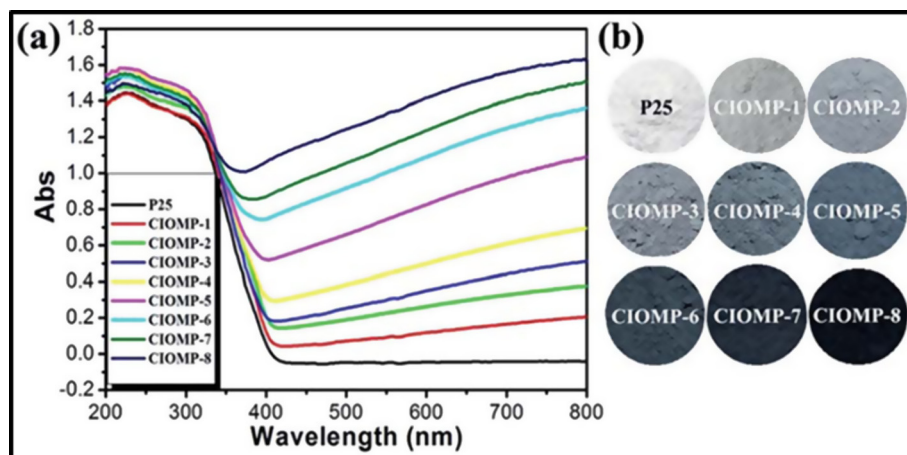

Fig. 11. (a) The UV–visible absorbance spectra of colored TiO_2 and (b) photographs of colored TiO_2 and pristine P25. CIOMP-1 at 300 °C for 5 min, CIOMP-2 at 300 °C for 10 min, CIOMP-3 at 300 °C for 20 min, CIOMP-4 at 300 °C for 30 min, CIOMP-5 at 300 °C for 40 min, CIOMP-6 at 300 °C for 50 min, CIOMP-7 at 300 °C for 120 min, CIOMP-8 350 °C for 60 min [109]. Reprinted with permission from Ref. [109]. Copyright 2014, Royal Society of Chemistry.
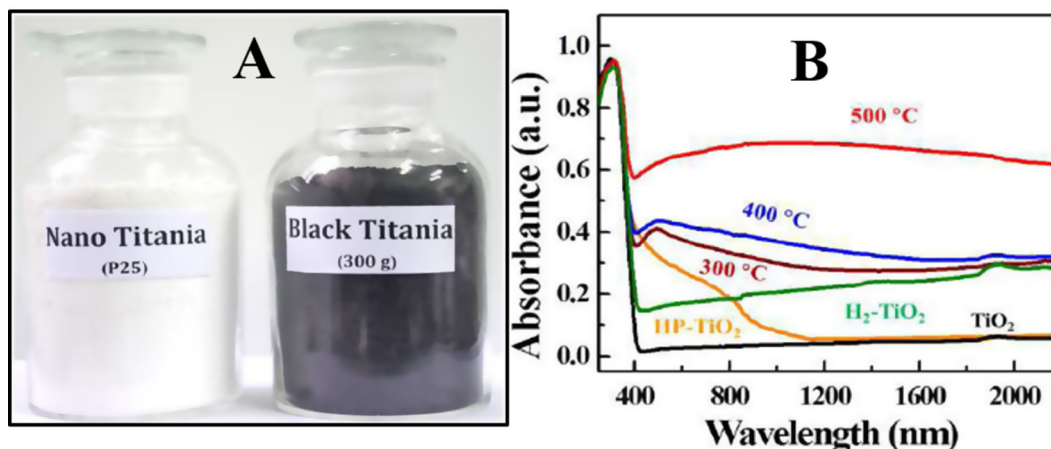
Fig. 12. (A) Photograph of P25 and Al reduced black TiO_2 and (B) absorption spectra of TiO_2 (P25), High Pressure hydrogenated TiO_2 (HP-TiO_2) and Al reduced TiO_2 [110]. Reprinted with permission from Ref. [110]. Copyright 2013, Royal Society of Chemistry.
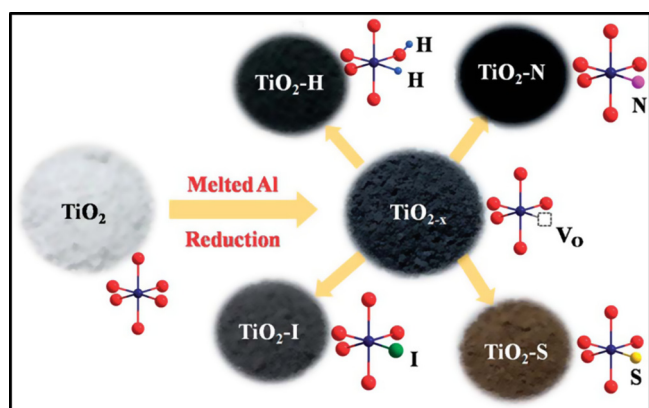

Fig. 13. Schematic illustration for the formation of black TiO_{2-x} from pristine white TiO_2 and the occupation of dopants in the oxygen vacancy sites [113]. Reprinted with permission from Ref. [113]. Copyright 2014, Royal Society of Chemistry.
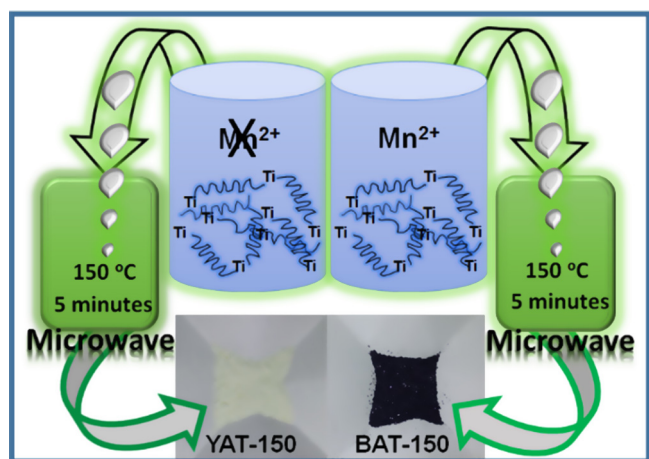

Fig. 14. Schematic representation for the synthesis of oxygen rich yellow anatase TiO_2 and oxygen vacancy rich black anatase TiO_2 [115]. Reprinted with permission from Ref. [115]. Copyright 2015, Royal Society of Chemistry. (For interpretation of the references to color in this figure legend, the reader is referred to the web version of this article.)

absorption was also reported recently [117]. In the experiment, a piece of Ti foil was immersed in a mixture of aqueous NaOH and ethylene glycol in an autoclave and heated at 220 °C for 24 h. The product obtained was a black film of $Na_2Ti_2O_4(OH)$. HCl solution was used to replace any Na^+ with H^+. Further annealing at 500 °C yielded black

TiO_2 [117].

2.12. Ionothermal method

Single crystalline black Ti^{3+} doped TiO_2 was prepared using Ionothermal method by Li et al. for efficient photocatalysis under solar illumination [118]. A buffer solution was made using Lithium acetate dihydrate along with glacial acetic acid and it was mixed in DMF solvent. A piece of cleaned Ti foil in an ionic liquid was placed in an autoclave along with the buffer solution in DMF. The autoclave was heated at 200 °C for 24 h and washed with ethanol followed by drying at 80 °C for 12 h [118].

2.13. Electrochemical Reduction-anodization

A two-step electrochemical reduction process (anodization technique) was performed by Xu et al. for the preparation of black TiO_2 nanotubes [119]. The anodization was carried out at 150 V for 1 h in ethylene glycol electrolyte containing 0.3 wt% NH_4F and 10 vol% H_2O_2 with a carbon rod as cathode and Ti as anode. TiO_2 nanotubes formed in the first was removed and subjected to second anodization and subsequent heating at 150 and 450 °C for 3 and 5 h respectively. The electrochemical reductive doping process was performed at room temperature under 5 V for 5–40 s in 0.5 M Na_2SO_4 aqueous solution where nanotubes as cathode and a Pt electrode as anode to obtain the black TiO_2 nanotube.

Zhang et al. implemented the similar strategy for fabricating black TiO_2 nanotubes [120]. The strategy is given in Fig. 15. Similarly, Li et al. also achieved black TiO_2 nanomaterials by the electrolytic reduction of TiO_2 nanotubes prepared by the anodization of Ti foil [121]. Zhou and Zhang synthesized black TiO_2 nanotubes with highly ordered nanotube arrays and appreciable optical absorbance [122]. A multipulse anodization strategy was introduced by Zheng et al. for the synthesis of black TiO_2 films [123].

Chen et al. implemented hydrothermal treatment on anodic TiO_2 nanotubes in deionised water, HCl and in NH_4OH [124]. The dissolution-precipitation of TiO_6^{2-} octahedra paved the way to crystalline anatase TiO_2 from the amorphous TiO_2 (Fig. 16). The polymorphs of TiO_2 (anatase, rutile and brookite) are composed of TiO_6^{2-} octahedra, and they differ only in their shared corners and edges. During the hydrothermal treatment a hydrated octahedral complex was formed on the surface of amorphous TiO_2which contained Ti-OH and Ti-OH_2^+ groups. The neighboring Ti-OH and Ti-OH_2^+ groups underwent condensation through olation–oxolation processes to create Ti-O-Ti bridges which are the backbones of all TiO_2 structures. Anatase structure
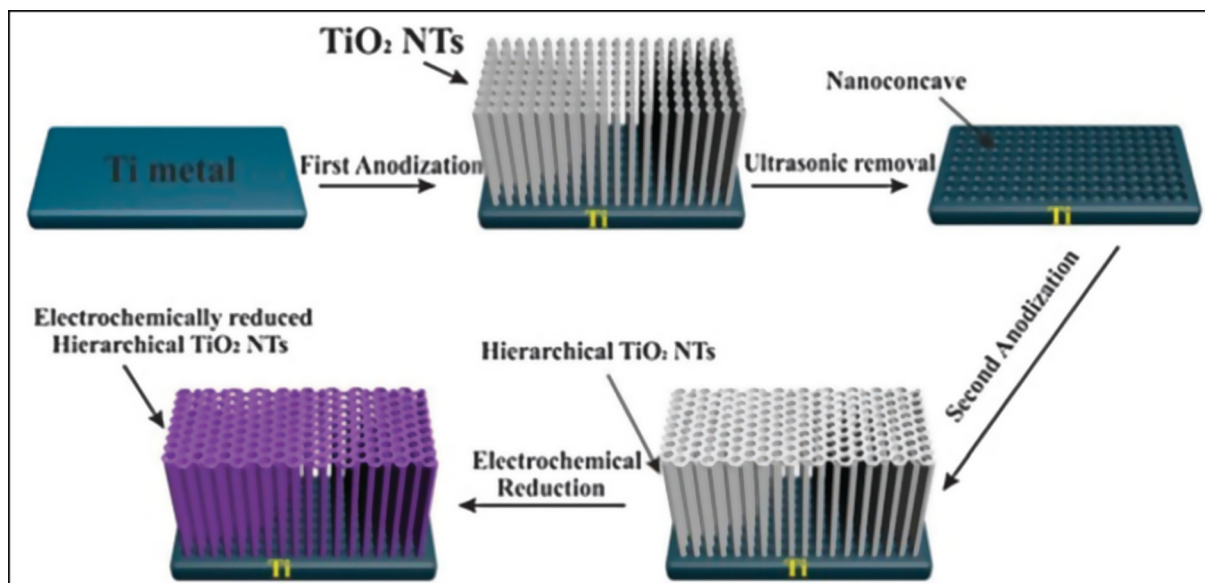
Fig. 15. Schematic representation of preparation of Ti^{3+} self doped black TiO$_2$ through electrochemical reduction [120]. Reprinted with permission from Ref. [120]. Copyright 2013 Royal Society of Chemistry.

formation is energetically more favorable than that of other TiO$_2$ frameworks [124].

Dong et al. prepared black TiO$_2$ nanotubes by anodization followed by annealing [125]. The anodized Ti foil washed with ethanol and distilled water, dried at 150 °C and sintered at 450 °C for 1 h in ambient atmosphere. After removing the top oxide layer, a layer of black TiO$_2$ was obtained on the substrate [125].

2.14. Hydroxylation followed by ultrasonication

Recently Fan et al. observed the formation of black TiO$_2$ through prolonged ultrasonication [126]. They started with the simple procedure of making TiO$_2$ sol followed by ultrasonication for several hours and drying at 80 °C. It was also noted that with long duration of ultrasonication, the intensity of black color increases.

2.15. Pulsed laser ablation

A pulsed laser ablation technique was implemented by Chen et al. for the synthesis of black TiO$_2$ [127]. In this method an aqueous suspension of TiO$_2$ was taken into a cuvette. Nd:YAG pulsed laser was then used to irradiate TiO$_2$ inside the cuvette for different time intervals. The

sample after 120 min irradiation was found to be black [127,128]. Pulsed laser irradiation on pristine TiO$_2$ led to oxygen release (oxygen vacancy production) leading to the formation of black TiO$_{2-x}$ was also reported recently [129].

2.16. Si quantum dot (QD) assisted chemical etching

Mesoporous black TiO$_2$ were prepared by Si QD assisted chemical etching [130]. The hydrogen terminated Si QD, were electrodeposited at the surface of Ti foil followed by chemical etching with HF. The H terminated Si QD facilitate the formation of Ti^{3+} states and mesoporous black TiO$_2$ structure were formed [130].

2.17. Self doping via gel combustion

A one pot gel combustion strategy has been developed recently by our group (Fig. 17) [131]. A gel formed out of Titanium butoxide, diethylene glycol and water was heated at 300 °C for 2 h. Subsequently cooled rapidly. This aqueous mediated process led to the formation of anatase crystal phase at relatively low calcination temperatures [131].
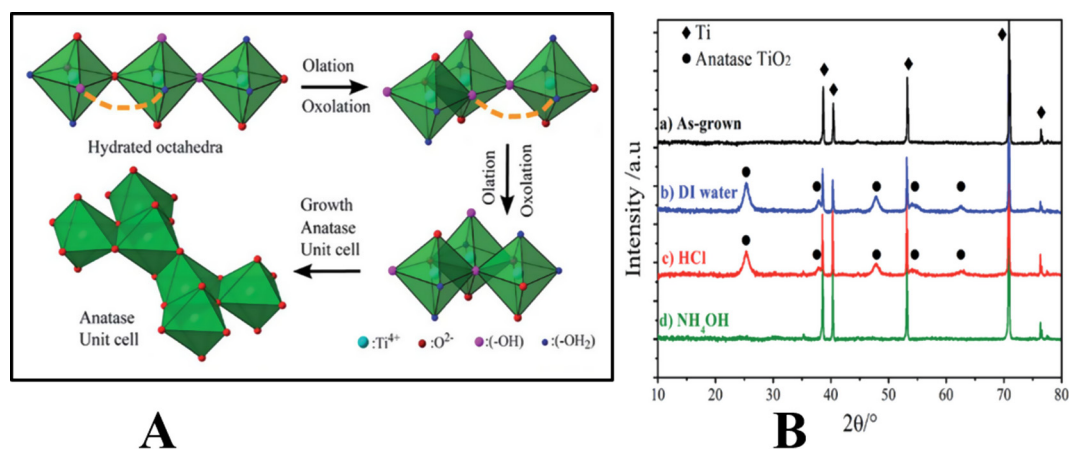

Fig. 16. A) Schematic illustration of phase evolution during hydrothermal treatment of anodic TiO$_2$ nanotube and B) XRD patterns of as grown TiO$_2$ nanotubes at different hydrothermal conditions [124]. Reprinted with permission from Ref. [124]. Copyright 2014, Royal Society of Chemistry.
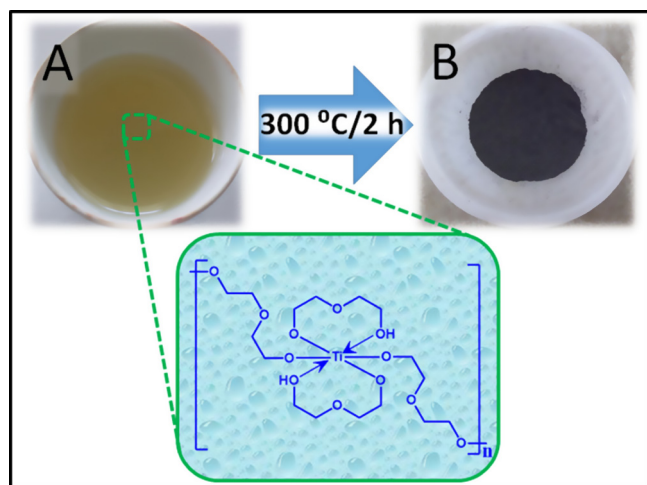
Fig. 17. Schematic illustration of the one pot gel combustion strategy [131]. Reprinted with permission from Ref. [131]. Copyright 2016, Royal Society of Chemistry.

2.18. Hydrogen treatment of $K_2Ti_2O_5$

Li et al. reported black TiO_2 (B)/anatase bicrystalline nano fibers [132]. Initially synthesized potassium dititanate ($K_2Ti_2O_5$) was treated with acid solution to reduce the concentration of K^+ and further washed with distilled water. The dried hydrated titanate was calcined under pure H_2 at 600 °C for 2 h to form the black TiO_2(B)/anatase bicrystalline nanofibers.

Table 1 summarizes the various synthesis methods available for black TiO_2 nanomaterials so far. Moreover, it explains the phase produced during the synthesis, morphology, structural, optical and electronic properties of TiO_2. Finally application of the as synthesized black TiO_2 were also shown in the Table 1.

3. Color transition and structural stability

In general the color of the white TiO_2 materials are transformed into black. The extent of the transformation is determined by various factors such as extent of hydrogenation, extend of hydroxylation, doping, various synthesis parameters such as amount of reductants (*e.g.* Al, Zn, $NaBH_4$, Ar, N_2) used, reduction temperature, duration of reaction *etc* [71,91,94,96,99,102,108–112,115,116,126,127,13]. Color variations in TiO_2 nanoparticles were observed in many cases in which the modifications affected the electronic structure [44,147–149]. Nitrogen doping in pristine TiO_2 results in a yellow coloration due to the slight reduction of band gap [150]. The valence band edge of N doped TiO_2 is shifted upwards due to the creation of new valence band levels as a result of intermixing of 2p orbitals of nitrogen and oxygen. In a similar sense one can think of the band structure modification of black TiO_2 after hydrogen doping where the mid gap band states can be tailored by hydrogenation [151,154]. Here intermixing of orbitals of hydrogen and oxygen is not energetically favorable compared to the case of nitrogen and oxygen. So the extreme coloration of black TiO_2 in view of the extended absorption towards IR region of electromagnetic spectra were studied in different aspects such as oxygen vacancy, presence of Ti^{3+} *etc* [152,153]. Pristine TiO_2 has a fixed band gap which is constituted from valence band composed of O 2p orbitals and conduction bands formed by the Ti 3d orbitals. The enhanced optical absorption features of black TiO_2 can be due to the formation and distribution of additional midgap energy levels or donor levels as a result there is an effective decrease in the band gap energy [77].

In the initial studies D. C. Cronzmeyer measured the concentration of oxygen vacancies in rutile single crystals on the basis of weight loss and Hall coefficient measurement showed that the number of conduction electron was approximately twice the number of oxygen vacancies

[153]. Further this model was simulated to a helium atom thereby calculated the first and second ionization energies to be 0.75 eV and 1.64 eV respectively. This result was in corroboration with the experimental observation of two visible band tails extending up to IR region of the electromagnetic spectra. It was also observed that as the number of oxygen vacancies increased, the thermal ionization energy decreased due to the interaction of closely spaced donor centers. However Cronzmeyer could not give much evidence for the decrease in thermal ionization energy with oxygen vacancies [71,153].

Chen et al. followed spectroscopic analysis of high pressure and high temperature annealed hydrogenated black TiO_2 as well as ab initio DFT calculations based on a model of hydrogenated large TiO_2 cluster, $Ti_{218}O_{436}H_{70}$ [154]. They compared the spectroscopic data with pristine TiO_2 and DFT outputs with that of a less hydrogenated system, $Ti_{210}O_{420}H_{12}$. It was reported that the surface of the $Ti_{218}O_{436}H_{70}$ cluster had a disorder layer consisting of partial Ti-O and O-H bonds retaining a crystalline anatase core. In the XPS spectra the presence of pristine TiO_2 exactly resembled that of black TiO_2 indicating that black TiO_2 did not possess Ti^{3+}. This result pointed that the valence band maximum was not contributed by Ti^{3+} instead the additional energy levels were formed by the presence of hydrogen. Much more evidences of absence of Ti^{3+} was also confirmed with soft X-ray absorption and X-ray emission spectroscopy. ^1H NMR spectra of pristine TiO_2 and black TiO_2 were slightly differed with two additional peaks at a chemical shift around 0 ppm corresponded to the extra hydrogen in the disordered surface layer of black TiO_2. In the FTIR spectra of black TiO_2 a signal at $4500 \, cm^{-1}$ was observed corresponded to H-H stretching vibrations indicative of trapped H_2 molecules in the crystal core or in the disordered surface. Computational and experimental calculations point to the sole contribution of hydrogen induced disordered layer which created additional mid gap levels responsible for the extended absorption up to IR region [154]. Raghunath et al. also observed the similar band structure modifications using DFT + U calculations [155]. Apart from these many reports point to the formation of Ti^{3+} which was also responsible for the enhanced absorption. Incorporation of hydrogen on TiO_2 surface bound to the lattice oxygen and formed Ti-OH groups thereby an electron was trapped in Ti site [156]. This extra electron contributed to the formation of Ti^{3+} and gave rise to mid gap energy levels. Finazzi et al. studied effect of this extra electron and that of oxygen vacancy in band structure modifications of black TiO_2. They concluded that the conduction band minimum was lowered to about 1 eV which was associated with Ti 3d orbitals [156]. Wang et al. investigated the effect of Ti^{3+} in reduced rutile TiO_2 which possesses a blue color [157]. In pristine rutile TiO_2, Ti ions are in slightly distorted octahedral site leading to the splitting of 3d orbitals into t_{2g} (lower energy) and E_g (higher energy). Here t_{2g} contributes to the conduction band minimum while O 2p contributes to valence band minimum. On the other hand the t_{2g} orbitals of Ti^{3+} self-doped system of the reduced rutile TiO_2 experience Jahn Teller distortion, consequently split into two energy levels (Fig. 18a). The lower energy level (dxy) constitutes one electron act an excitation center near the conduction band minimum. The corresponding d-d transition contributed to the visible light absorption and consequent blue color (Fig. 18b) [157].

Recently Nandasiri et al. systematically studied the thermal stability of H-implanted black TiO_2 [158]. At low temperature (~373 K), hydrogen implanted into rutile TiO2 (1 1 0) diffused into the surface and is completely depleted from the near-surface region (≤800 nm) by 523 K. The outward diffusion and depletion of H from TiO_2 is accompanied by extensive surface reduction within the probe depths of X-ray photoelectron spectroscopy (XPS) and ultraviolet photoelectron spectroscopy (UPS). Due to reduction, most likely, the reaction of H with surface oxygen occurs followed by formation and desorption of water. The presence of surface Ti^{3+} persists until the thermally induced surface-to-bulk diffusion of Ti^{3+} interstitials is initiated above 550 K. Nuclear reaction analysis (NRA) determines the hydrogen depth profiles as a function of annealing temperatures as shown in Fig. 19. The as

Table 1
Synthesis, properties and applications of black TiO$_2$.

Sl. No	Strategy	Phase	Morphological Nature	Defects	Application	Refs.
1	High pressure H$_2$ treatment	Anatase	Core-shell	Ti^{3+}, V$_o$	Photodegradation of Methylene Blue (MB) and phenol	[77]
2	Solvothermal method followed by high pressure H$_2$ treatment	Anatase	NSM	Ab	Hydrogen storage	[84]
3	High pressure H$_2$ treatment	Anatase	NSM	V$_o$	Photodegradation of MB	[85]
4	High pressure H$_2$ treatment at room temperature	Mixed (Anatase + Rutile + Ti$_2$O$_3$)	NSM	Ti^{3+}	Photocatalytic H$_2$ generation	[86]
5	Low pressure H$_2$ treatment on rutile	Rutile	Nanowire arrays	V$_o$	Photoelectrochemical water splitting	[87]
6	H$_2$ flow followed by rapid cooling under inert atmosphere	Anatase	Core-shell	Ti^{3+}, V$_o$	NS	[88]
7	Biotemplate assisted H$_2$ treatment	Anatase	Mesoporous, Nanosheets	Ti^{3+}	Photocatalytic H$_2$ generation	[89]
8	H$_2$-Ar treatment	Anatase	Nanotube arrays	Ti^{3+}, V$_o$	Cocatalyst free Photocatalytic H$_2$ generation	[90]
9	H$_2$-Ar treatment	NM	NSM	NM	Photodegradation of MB	[91]
10	H$_2$-Ar treatment	Mixed (Anatase + Rutile)	Nanorods	Ti^{3+}, V$_o$	Li ion batteries	[92]
11	Magnesiothermal H$_2$-Ar treatment	Anatase	NSM	Ti^{3+}, V$_o$	Photocatalytic H$_2$ generation	[93]
12	UV irradiation followed by Ar treatment	Anatase, TiO$_2$ (B)	NSM	Ti^{3+}, V$_o$	Photodegradation of Methyl Orange (MO)	[94]
13	N$_2$ flow under atmospheric pressure	Anatase	Core-shell	Ti^{3+}, V$_o$	Photodegradation of MO	[95]
14	Hydrogen spill in H$_2$-N$_2$ environment	Mixed (Anatase + Rutile)	Core-shell	V$_o$	Photocatalytic water splitting	[96]
15	Heat treatment in low partial pressure H$_2$ and H$_2$-N$_2$ treatment	Anatase and Rutile	NSM	Ti^{3+}, V$_o$	Photodegradation of MO	[97]
16	H$_2$-N$_2$ mixed flow on protonated titanate nanotubes	Anatase(< 150 °C) and TiO$_2$-B (> 150 °C)	Core-shell, Nanotube, Nanobelt	Ti^{3+}, V$_o$	Photodegradation of phenol	[98]
17	Ni^{2+} doping followed by Ar treatment	Anatase	Core-shell	Ti^{3+}, V$_o$	Photodegradation of MO and RhB	[99]
18	Oxidizing TiH$_2$ in H$_2$O$_2$ followed by calcinations in Ar gas	Rutile	NSM	Ti^{3+}, V$_o$	Photodegradation of MB	[100]
19	Ar treatment	Anatase	NSM	Ti^{3+}, V$_o$	Li ion batteries	101
20	Hydrogen plasma on P25	Anatase	Core-shell	Ti^{3+}, V$_o$	Photocatalytic H$_2$ generation	[102]
21	Hydrogen plasma assisted chemical vapor Deposition	Mixed (Na$_{0.23}$TiO$_2$ + Ti$_2$O$_3$)	Core-shell	V$_o$	Photodegradation of RhB	[103]
22	Hydrogen plasma	Anatase	Core-shell	Ti^{3+}, V$_o$	Li ion battery	[104]
23	Hydrogen plasma	Anatase	Core-shell	Ti^{3+}, V$_o$	Photodegradation of MB	[105]
24	Water Plasma	Mixed (Anatase + Rutile)	Nano/microspheres	Ti^{2+}, Ti^{3+}, V$_o$	Photodegradation of MB	[106]
25	Microwave-induced Plasma	Mixed (Anatase + Rutile + Brookite)	NSM	NM	NS	[107]
26	NaBH$_4$ Reduction	Mixed (Anatase + Rutile)	Core-shell	Ti^{3+}, V$_o$	Photocatalytic H$_2$ generation	[108]
27	NaBH$_4$ Reduction	Anatase	NSM	Ti^{3+}, V$_o$	Photocatalytic H$_2$ generation	[109]
28	Al reduction	Anatase	Core-shell	Ti^{3+}, V$_o$	Photodegradation of MO and Photocatalytic H$_2$ generation	[110]
29	Melted Al reduction of pristine anodized and air-annealed TiO$_2$ nanotube arrays	Anatase	Nanotube arrays	Ti^{3+}, V$_o$	Photoelectrochemical water splitting	[111]
30	Al reduction on Degussa P25	Mixed (Anatase + Rutile)	Core-shell	Ti^{3+}, V$_o$	Photodegradation of MO and Photocatalytic H$_2$ generation	[113]
31	ZnCl$_2$/KCl molten-salt assisted annealing under Ar atmosphere	Mixed (Anatase + Rutile)	Hexagonal nanosheets	Ti^{3+}, V$_o$	Photodegradation of MO	[114]
32	Sol-Microwave processing for 5 min	Anatase	NSM	Ti^{3+}, V$_o$	Photodegradation of MB	[115]
33	Solvothermal ascorbic acid reduction	Mixed (Anatase + Rutile)	NSM	Ti^{3+}, V$_o$	Photodegradation of MB and phenol	[116]
34	Solvothermal method	Mixed (Anatase + Rutile)	Seeds	Ti^{3+}, V$_o$	NS	[117]
35	Ionothermal method	Anatase	Single crystal	Ti^{3+}, V$_o$	Photodegradation of Rhodamine B and aniline	[118]
36	Electrochemical hydrogenation	Anatase	Nanotube	V$_o$	Photoelectrochemical water splitting	[119]
37	Electrochemical reduction	Mixed (Anatase + Ti$_4$O$_7$ + Ti$_6$O$_{11}$)	Nanotube arrays	Ti^{3+}	Water splitting	[120]
38	Electrochemical doping	Anatase	Nanotubes	Ti^{3+}, V$_o$	Supercapacitor, Photodegradation of a textile dye, RB	[121]
39	Electrochemical self-doping	Anatase	Nanotube arrays	Ti^{3+}, V$_o$	Supercapacitor	[122]
40	Hydrothermal treatment of anodic TiO$_2$ nanotube arrays	Anatase	Wire in tube architectures	Ti^{3+}, V$_o$	Photodegradation of MB	[124]
41	Electrochemical anodization	Anatase	Hexagonally dimpled layer	Ti^{3+}, V$_o$	Photodegradation of RhB	[125]
42	Hydroxylation-ultrasonication	Amorphous	NSM	Ti^{3+}, V$_o$	Photodegradation of Acid fuchsin	[126]
43	Pulsed laser ablation	Anatase	Nanospheres	Ti^{3+}, V$_o$	Photodegradation of RhB	[127]

Table 1 (*continued*)

Sl. No	Strategy	Phase	Morphological Nature	Defects	Application	Refs.
44	Pulse Laser Ablation	Mixed (Anatase + Rutile)	NSM	NS	Microwave absorbing material	[128]
45	Pulsed UV laser irradiation	Mixed (Anatase + Rutile)	NSM	Ti^{3+}, V_o	Solar water splitting	[129]
46	Si quantum dot assisted chemical etching	Anatase	Mesoporous	Ti^{3+}, V_o	Photodegradation of MO	[130]
47	One pot Gel combustion	Anatase	Defective core	Ti^{3+}, V_o	Photodegradation of MB	[131]
48	Minimizing K^+ in $K_2Ti_2O_5$ followed by H_2 treatment	Bicrystalline TiO_2(B)/anatase	Nanofibres	V_o	Photodegradation of MO	[132]
49	In situ electrochemical self-doping of TiO_2 NT was performed *via* chronoamperometry	NM	Nanotubes	Ti^{3+}	Anode for lithium ion battery	[133]
50	H_2 plasma	Anatase + brookite	Nanoporous	V_o, Ti^{3+}	phenol (Ph), reactive black 5(RB 5), rhodamine B (Rho B) and methylene blue (MB)	[134]
51	Microwave	NM	Core-shell	Ti^{3+}	Photocatalytic Decomposition of Rhodamine B (RhB)	[135]
52	Combined EISA (evaporation induced self-assembly) Method and CASH (combined assembly of soft and hard) method	TiO_2-B	Mesoporous	NM	Photocatalytic H_2 generation, Degradation of MB and 4-CP	[136]
53	Hydrothermal method with Chemical reduction	Anatase + Rutile	3D Flower-like Black N-TiO_{2-x}@MoS_2	$Ti3+$	Photodegradation of MO, Photocatalytic H_2 generation	[137]
54	Magnesium reduction of white P25 nanocrystals	Anatase + Rutile	Core-shell	NM	Solar Water Evaporation	[138]
55	Ultrasonic irradiation	Anatase	Core-shell	NM	Photodegradation of acid fuchsin (AF)	[139]
56	Hydrogen plasma assisted reduction	TiO_2-B	Nanowires	V_o	Photoelectrochemical water splitting	[140]
57	Hydrogen plasma treatment of pristine TiO_2 nanowire arrays	Rutile	Nanowire arrays	V_o	Photodegradation of methylene blue solution	[141]
58	Aluminum reduction of $H_2Ti_3O_7$ nanobelts: Pd is also deposited	Anatase	Nanobelts	$Ti3+$	Oxygen Reduction Reaction (ORR)	[142]
59	Uniform Black TiO_2 Nanothorns/Graphene/Black TiO_2 Nanothorns Sandwichlike Nanosheets	Anatase	Nanothorns	Ti^{3+}	Photocatalytic decomposition of Atrazine ($C_6H_{14}ClN_5$)	[143]
60	Hydrogenation at 500 °C	Anatase	Nanosheets	Ti^{3+}, V_o	Lithium-ion Battery Anode	[144]
61	Magnesium Reduction of P25	Pure or Mixed anatase and Rutile phase depends on Mg dosage	Core-Shell	Ti^{3+}	Photoelectrochemical water splitting	[145]
62	Aluminum Reduction	Anatase	Nanocage	Ti^{3+}, V_o	Solar Desalination	[146]
63	H_2 treatment	Anatase	Core-shell	Ab	NS	[154]
64	Al reduction and post annealing	Mixed (Anatase + Rutile)	Core-shell	Ti^{3+}, V_o	Photodegradation of MO	[160]
65	Solvothermal reaction of a Ti^{3+} precursor followed by annealing	Anatase	NSM	Ti^{3+}, V_o	Photodegradation of MB	[161]
66	Solvothermal Zn reduction	Anatase, Mixed (Anatase + Rutile)	Truncated octahedron	Ti^{3+}, V_o	Photocatalytic H_2 generation	[162]
67	H_2 reduction of white TiO_2 inverse opals	Anatase	Core-shell, Inverse opals	NM	Photodegradation of MB	[164]
68	Hydrogen plasma	Anatase	Nano fibers	Ti^{3+}, V_o	Photoelectrochemical performance	[171]
69	H_2 treatment on protonated titanate nanotube	Anatase	Microsphere	NM	Photocatalytic H_2 generation	[178]
70	Al reduction	Brookite	Core-shell, Flower like particles	Ti^{3+}, V_o	Photodegradation of MB and MO	[180]
71	Hydrothermal method	Mixed (Anatase + Rutile)	Porous thin films	Ti^{3+}	Photocatalytic CO_2 reduction	[181]
72	Hydrogenation at 500 °C	Anatase	Ordered mesoporous arrays	Ti^{3+}	Photocatalytic H_2 generation	[184]
73	Electrochemical method under H_2 atmosphere	Anatase	Nanotube arrays	Ti^{3+}, V_o	Li ion battery	[185]
74	$NaBH_4$ reduction followed by Ar treatment	Mixed (Ti_2O_3 + Ti_3O_5+TiO_2)	Nanobelts	Ti^{3+}, V_o	Photodegradation of MO and Photocatalytic H_2 generation	[187]
75	Template free solvothermal method	Anatase	Mesoporous, Hollow spheres	Ti^{3+}	Photocatalytic H_2 generation	[189]
76	Solution plasma synthesis	Mixed (Anatase + Rutile)	Mesoporous Nanoleaves	Ti^{3+}, V_o	Al ion battery	[190]
77	H_2 flow on TiO_2 crystal at 1 atm	Mixed (Anatase + Rutile)	Core-shell	Ti^{3+}, V_o	Photodegradation of atrazine	[201]
78	Molten Al treatment-H_2S treatment	Anatase, Rutile	Core-shell	Ti^{3+}, V_o	Photodegradation of MO, Photocatalytic H_2 generation	[209]
79	High energy proton implantation	Anatase	Nanotube arrays	Ti^{3+}	Photocatalytic H_2 generation	[210]
80	$NaBH_4$ treatment followed by annealing under N_2 atmosphere	Anatase	NSM	Ti^{3+}, V_o	Photocatalytic H_2 generation	[212]
81	Cu treatment-H_2 flow	Anatase	NSM	V_o	CO_2 photoreduction	[213]
82	Hydrogenation on nanotube array	Mixed (Anatase + Rutile)	Nanotube arrays	Ti^{3+}, V_o	Electrocatalytic water disinfection	[214]
83	Hydrothermal method combined with post annealing under N_2 flow	Brookite	Single crystal	Ti^{3+}, V_o	Photocatalytic CO_2 reduction	[215]
84	Ar treatment on TiO_2 gel precursor	Anatase	NSM	V_o	Counter electrode in dye sensitized solar cell	[216]
85	Mn^{2+} assisted Sol-solvothermal strategy	Anatase	NSM	Ti^{3+}, V_o	Photoanode material in DSSC	[217]
86	Ar treatment	Anatase	NSM	Ti^{3+}, V_o	Li ion battery	[221]
87	$NaBH_4$ treatment followed by Ar treatment	Anatase	Core-shell	Ti^{3+}, V_o	Na ion battery	[222]

Table 1 (*continued*)

Sl. No	Strategy	Phase	Morphological Nature	Defects	Application	Refs.
88	Electrochemical self-doping	Anatase	Nanotube arrays	Ti^{3+}, V_o	Supercapacitor and oxidant generating anode	[224]
89	Hydrogenation followed by Ag decoration	Anatase	Core-shell, Nanowires	Ti^{3+}, V_o	Surface enhanced Raman spectra (SERS) Substrates	[225]
90	Hydrogen plasma	NM	NM	NM	Photothermal therapy	[226]
91	Al reduction	NM	NM	NM	Photothermal/Photodynamic therapy	[227]
92	Reduction using lithium-ethylene diamine (Li-EDA) at room temperature under anhydrous and N_2 atmospheric condition	Anatase, Rutile and mixed (anatase + rutile)	NSM	V_o	Photocatalytic disinfection	[228]

NM: Not Mentioned, NSM: No Specific Morphology.

implanted hydrogen profile was peaked at a depth of 300 nm [159]. The hydrogen profile was altered or more clearly the peak at 300 nm was diminished by the annealing treatment at 373 K. During this, little or no hydrogen was lost from the crystal into the vacuum as shown by the integrated NRA signal (inset to Fig. 19). Significantly a notable amount of hydrogen was lost into the vacuum after annealing at 473 K (inset to Fig. 19). After 473 K annealing, a remnant of the original profile remained and this signal points to the presence of trapped H at the structural defects generated during the implantation process. Within the sampling depth of the NRA experiment, all of the implanted H were removed after further annealing treatment at 523 K. Due to the rapid bulk diffusion of hydrogen to its interfaces, followed by desorption (as H_2O and H_2) and surface reduction, the limited stability of H-TiO_2 was demonstrated. Also according to their previous results the kinetics of the removal of surface hydrogen (as water) into vacuum, exceeds that of the diffusion into TiO_2 (1 1 0) bulk which emphasizes the limitation of the thermal processing of H-TiO_2 in visible light applications [158].

Experimental evidences point to the dependence of black coloration on synthetic strategy. For example Wang et al. synthesized black TiO_2 using Al as reductant at different temperatures 400, 500 and 600 °C [160]. The black TiO_2 at 500 °C possessed intense black color, absorbance and photoactivity. When the reductant is the same, the intensity of black color will depend upon the gas used. For example. when $NaBH_4$ used as a reductant to produce black TiO_2, the sample treated at 350 °C showed maximum black color in presence of Ar gas flow [109] whereas intense black color was observed at a temperature of 500 °C for N_2 gas flow [161]. The so formed defective TiO_{2-x} was treated at various temperatures (300–700 °C) under 150 sccm N_2 gas flow for 3 h (Fig. 20). As shown in figure, the transition of color occurred and the maximum blackness was observed for TiO_2-500. In addition as the temperature increased the intensity of anatase peaks increased.

Another important observation was when Zn used as a reductant, rutile black TiO_2 nanorods were formed instead of the formation anatase black TiO_2, The black coloration was increased with the increasing amount of Zn (from 0.5 to 2.5 mmol) [162]. The color intensity of TiO_2 can be varied using laser ablation method with respect to the time interval (Fig. 21) selected. Here the color changes from white to dark blue as time varies from 0 to 120 min of laser irradiation [127]. It has been also proved that, by varying the ultrasonication time period, the color of TiO_2 nanomaterial can be varied from white to black [126].

4. Phase, defect states and morphology of black TiO_2

The phase and defect states are generally observed by using XRD, Raman, XPS, EPR, FTIR, NMR, synchrotron X-ray absorption spectroscopic techniques [127–132,158–196]. Recently HRTEM images are also used in detecting the surface defects present on a nanomaterial along with the morphology [127]. Ti^{3+} ions and oxygen vacancies are the common defects which are observed in the surface of a black TiO_2 crystal. XRD depicts the crystal phase of TiO_2 and some extent of crystallinity and the incorporation of elements into the crystal lattice can also be perceived from XRD. We have recently proposed anatase phase pure TiO_2 and the peaks were lesser in number. Interestingly after the Mn^{2+} reduction, the XRD peaks were found to be shifted towards higher 2θ. Additionally, the peak texturing in all existing planes along with new anatase peak formation (Fig. 22) was occurred and revealed the phase purification activity of Mn^{2+}. It was due to the synergistic effects of the thermodynamic and kinetic factors which control crystal nucleation. In addition, the Mn^{2+} modification tends to specifically lower the Gibbs free energy in the high index anatase (1 0 5) orientation, and thus stabilizes the distinct atomic configuration along the (1 0 5) plane [115]. The black TiO_2 nanoparticles synthesized through Mg reduction has resulted in anatase/rutile mixed phase along with other non-stoichiometric titanium oxide phases depends on the amount of Mg used [138]. As the amount of Mg increased the
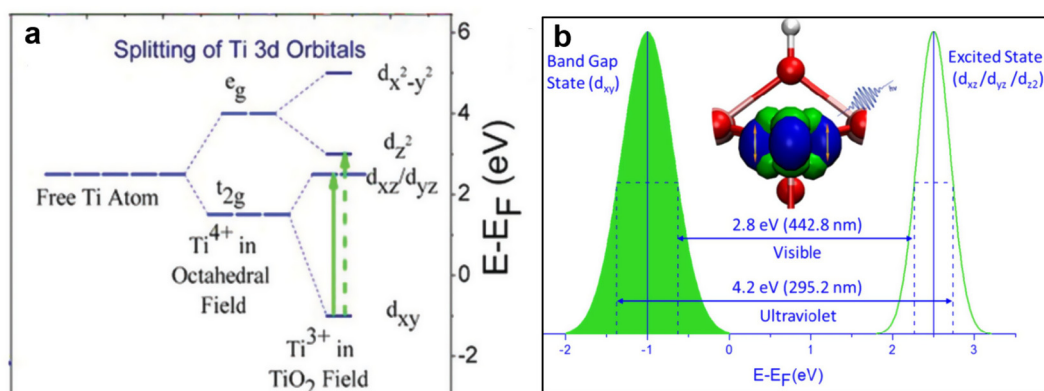
Fig. 18. a) Crystal feld splitting of Ti 3d orbitals on TiO_2 (1 1 0) b) Schematic of the enhanced and extended photoabsorption via 3d → 3d transitions from the $3d^1$ bandgap state to the excited resonant state [157]. Reprinted with permission from Ref. [157]. Copyright 2015, Americal Chemical society.
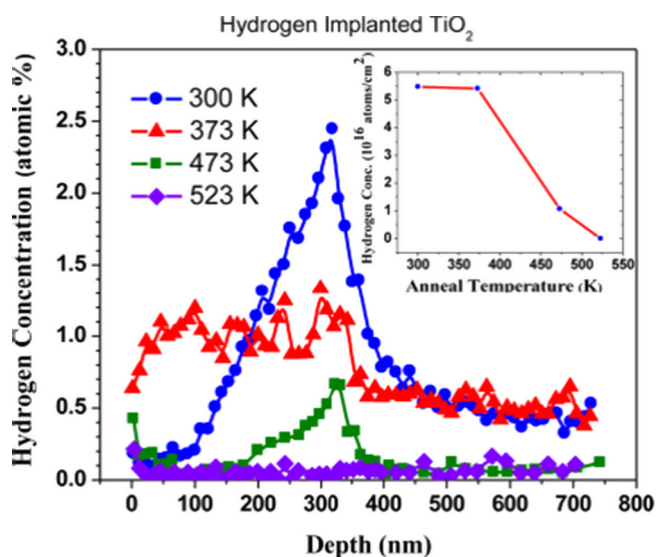

Fig. 19. Hydrogen depth profiles measured by the resonant ^1H (^{19}F, αγ) ^{16}O for H-implanted TiO_2 (1 1 0) single crystal after annealing in vacuum. Inset displays the integrated area in the profile as a function of annealing temperature [158]. Reprinted with permission from Ref. [158]. Copyright 2015, American Chemical Society.

Fig. 20. a) Ti^{3+} self-doped TiO_2 samples prepared by post annealing treatment in the 300–700 °C temperature range for 3 h under N_2 gas flow and b) the corresponding XRD pattern [161]. Reprinted with permission from Ref. [161]. Copyright 2015, Elsevier.

Fig. 21. Suspended TiO_2 solution before and after laser modification at different time intervals [127]. Reprinted with permission from Ref. [127]. Copyright 2015, American Chemical Society.

crystallinity of the sample decreased. H-R. An et al. observed anatase/brookite bicrystalline phase using XRD analysis [134]. They synthesized the bicrystalline nanoporous black TiO_2 through H_2 plasma treatment. Later Z. Tian et al. reported hydrogenated TiO_2-B phase and it was confirmed through XRD that TiO_2-B phase maintained its actual framework even after hydrogenation [140] C-C. Wang et al. synthesized black TiO_2 nanowires through hydrogen thermal as well as hydrogen plasma treatment and the resultant phases were purely rutile [141].

Wang et al. reported that as the temperature increased the intensity of XRD peaks increased which is due to the decrease in defect states and/or increase in crystallinity of TiO_{2-x} [160,163]. Fan et al. synthesized amorphous TiO_2 nanoparticles by hydroxylation followed by ultrasonication but the XRD patterns showed no characteristic peaks of TiO_2 under any sonication time interval [126]. Apart from these, no change in XRD pattern was observed between white and black TiO_2 reported by Xin et al. (Fig. 23A) [164]. Also for the same materials, no change in Raman spectra were also observed (Fig. 23B) indicating that no modification of the main crystal phase was occurred even though the color of the TiO_2 material was changed from white to black [165]. The disordered surface layer present in black TiO_2 which is undetectable in XRD can be effectively characterized through Raman spectroscopy.

Leshuk et al. showed the high amount of hydrogenation using Raman spectra [85] where an intense peak at 1354 cm^{-1} for black TiO_2
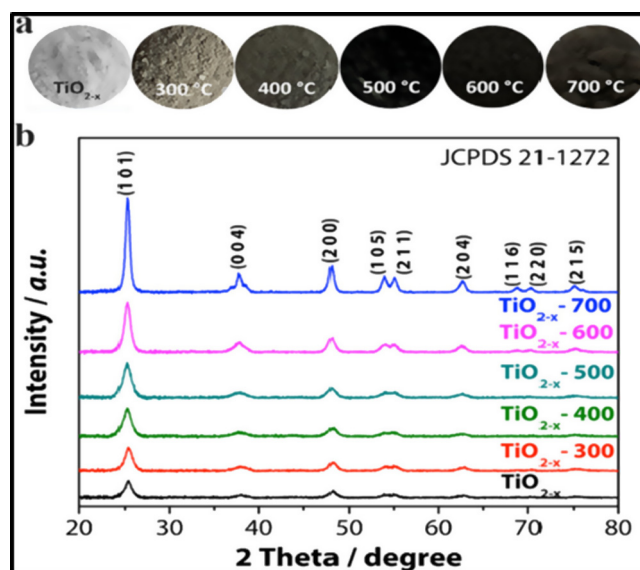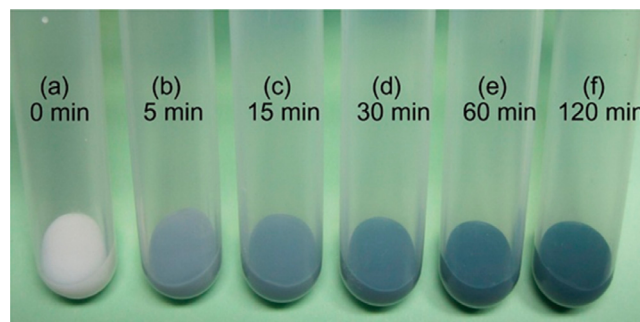
is ascribed to the Ti-H mode of vibration (Fig. 24A) [166]. Another important study using Raman spectra by Zhang et al. confirmed the presence of lattice disorder in black TiO_2 resulting from phonon confinement and non-stoichiometry due to the oxygen vacancy (V_o) doping (Fig. 24B) in black TiO_2 which was evidenced by the blue shift of main Raman peak at 147.8 cm^{-1} to higher wave number, 153 cm^{-1} along with peak broadening as indicated [167].
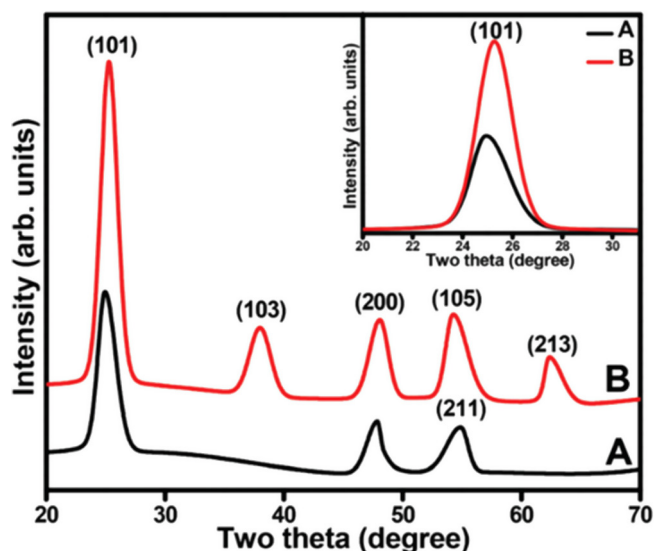
Fig. 22. XRD pattern of A) yellow anatase TiO_2 and B) black anatase TiO_2. Inset displays the shifted (1 0 1) peak of anatase due to Mn^{2+} incorporation [115]. Reprinted with permission from Ref. [115]. Copyright 2015, Royal Society of Chemistry. (For interpretation of the references to color in this figure legend, the reader is referred to the web version of this article.)

In the Raman spectra of magnesiothermal Ar treated black TiO_2 (Fig. 25), the peak exhibited a blue shift along with peak broadening compared to the commercially available TiO_2 annealed in Ar atmosphere [93]. These features were observed earlier in the case of modified TiO_2 nanoparticles where non-stoichiometry and defects states attributed with the structure [168].

In the Raman spectra of black TiO_2 (B)/anatase bicrystalline nano fibers, six Raman active modes of the anatase phase ($3Eg + 2B1g + A1g$) were detected indicating that anatase phase is the main component of these TiO_2 samples [132]. In addition to these peaks, two weak bands are also seen from 220 to $260 \, cm^{-1}$ which corresponded to Raman active modes of TiO_2 (B) and is shown inset of Fig. 26[169,170].

Existence of defects such as Ti^{3+} and oxygen vacancies present in a material can be more clearly perceived from X-ray photoelectron spectroscopy (XPS) [77,115], electron spin resonance spectroscopy (ESR spectroscopy) [90] and synchrotron X-ray absorption–emission photoelectron spectroscopic [154] techniques. In the most of the XPS studies conducted so far, Ti^{3+} defects in black TiO_2 are seen as a result of hydrogen treatment [77], chemical reduction, electrochemical reduction [125], microwave treatment [115], Al reduction [110], gel combustion strategy [131] and hydrogen plasma treatment [171]. During H_2 plasma treatment on electrospun nanofibers along with Ti^{4+}

and Ti^{3+}, Ti^{2+} has also been detected at the surface of black TiO_2 [171].

Wang et al. manipulated the higher wavelength solar absorbing black $TiO_{2-x}H_x$ (~83%) which was further characterized by FTIR and NMR spectroscopic techniques to confirm the structural changes that has been formed due to hydrogenation [102]. In the FTIR analysis (Fig. 27a) the presence of Ti-O-Ti bond of TiO_2 is clearly visible and in the longer wavelength range new peaks were originated at 3645, 3670 and $3685 \, cm^{-1}$ due to hydrogenation (Fig. 27b). These results were attributed to tetrahedral coordinated vacancies and are assigned to the presence of Ti^{4+}-OH. Another new peak located at $3710 \, cm^{-1}$ was ascribed to the terminal -OH groups indicating the embedded H atoms with in the TiO_2 network [172–173].

Comparatively large band width was observed for hydrogenated TiO_2 may be due to incorporation of H at the bridging sites of TiO_2 or due to the change in environment of bridging sites at different planes [174]. The additional signals at chemical shifts, $\delta = 0.4$ and $0.01 \, ppm$ are due to respectively terminal and internal hydroxyl groups of anatase (Fig. 27c and d) [175]. According to Chen et al. [154] the chemical shift values of terminal and internal hydroxyl groups of anatase were $\delta = 0.73$ and $-0.03 \, ppm$ respectively. The peaks were of low intensity indicated the low concentration of H that has been incorporated and the new peaks were possibly due to dynamic exchange mechanisms such as rapid isotropic diffusion and rapid exchange between similar proton environments [176].

Almost similar XPS (both Ti2p and O1s) were observed for both pristine and hydrogenated TiO_2 [102]. The Ti2p centered at 458.5 and 464.3 eV ($Ti2p_{3/2}$ and $Ti2p_{1/2}$) typical for Ti^{4+}-O bond of TiO_2 [177]. An additional broad peak at 457.1 eV was also observed which is attributed to surface Ti-H bonds [178]. Interestingly negligible effect on band edge position (2.05 eV) was also noticed [179]. In addition the PL spectra showed a notable decrement in PL intensity for $TiO_{2-x}H_x$ as compared to the pristine TiO_2 confirmed the incorporation of H into the crystal lattice of TiO_2 (Fig. 28). Similarly the VB spectra showed the same fashion *i.e.* the same band edge position was explained by Leshuk et al. According to them hydrogenation followed by annealing had no effect at the band edge position of TiO_2 even though they had explained the disordered structure using Raman spectra [85]. Similarly no effect on Ti2p spectra was observed after hydroxylation ultrasonication reported by Fan et al. [126].

According to our previous report we have developed oxygen richness at the surface of yellow TiO_2 and was evident from XPS [115]. Whereas on Mn reduction the yellow oxygen rich TiO_2 transformed into oxygen vacancy rich black anatase TiO_2. The $Ti2p_{3/2}$ peak (460.05 eV) of oxygen rich TiO_2 was colossally decreased to 457.65 eV which suggested the oxygen vacancy richness forcefully applied on oxygen rich environment (Fig. 29) [115].

Naldoni et al. introduced surface defects on P25 TiO_2 with band gap energy 3.25 eV. The Density of States showed that the reduction in band
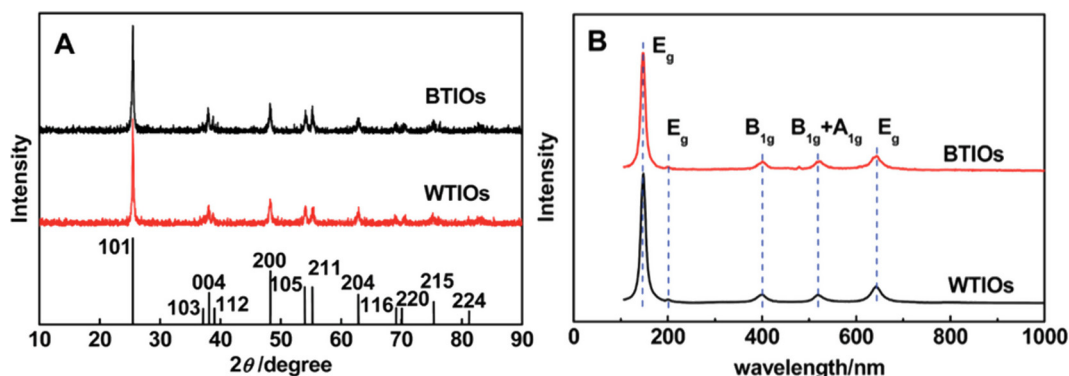

Fig. 23. A) XRD and B) Raman spectra of white TiO_2 inverse opals (WTIOs) and black TiO_2 inverse opals (BTIOs) [164]. Reprinted with permission from Ref. [164]. Copyright 2015, Royal Society of Chemistry.
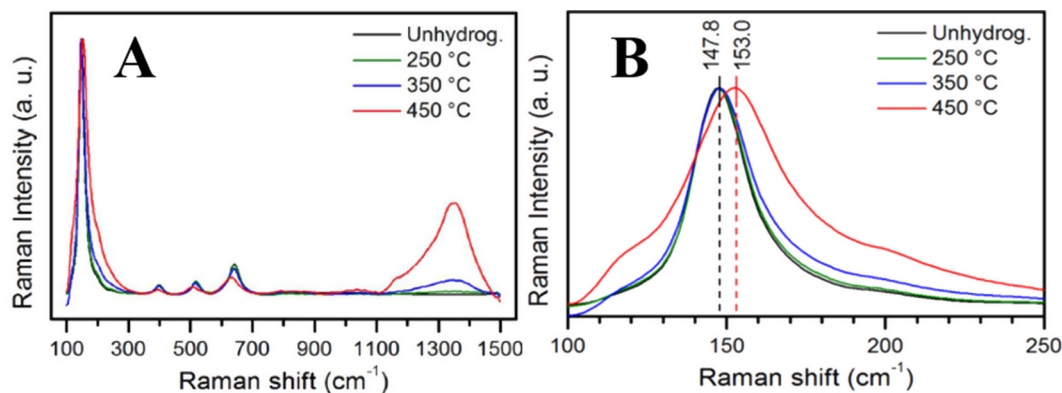
Fig. 24. A) Wide area Raman spectra and B) Raman spectra justifying the main peak shift [85]. Reprinted with permission from Ref. [85]. Copyright 2013, American Chemical Society.
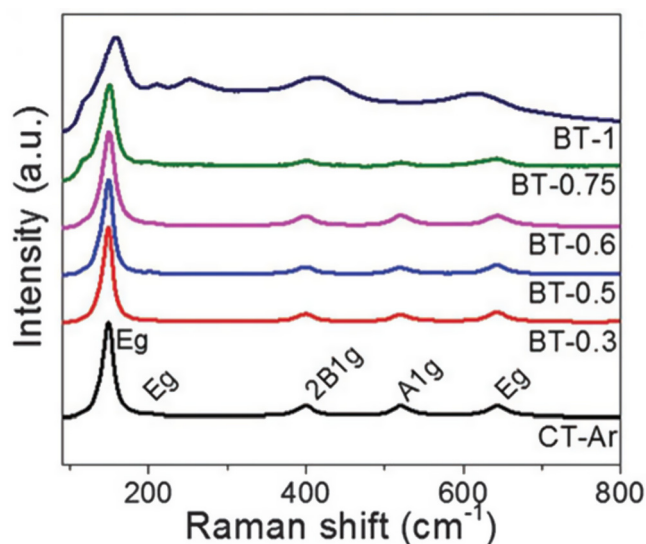

Fig. 25. Raman spectra of argon treated commercial TiO_2 (CT-Ar) and Mg reduced black TiO_2 [93] Reprinted with permission from Ref. [93]. Copyright 2015, Royal Society of Chemistry.
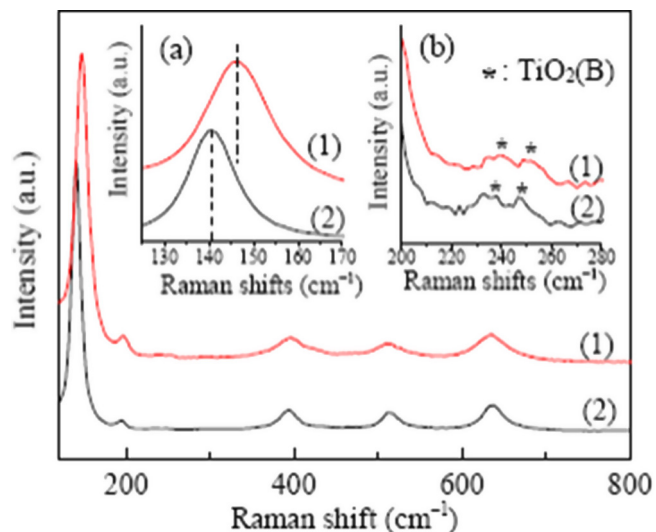

Fig. 26. Raman spectra of black bicrystalline TiO_{2-x} (1) and white bicrystalline TiO_2 (2). Inset shows a) the red shift of the main Raman peak at 141 cm^{-1} and b) peaks assigned to TiO_2 (B) [132]. Reprinted with permission from Ref. [132]. Copyright 2015, Elsevier. (For interpretation of the references to color in this figure legend, the reader is referred to the web version of this article.)

gap energy of black anatase TiO_2 owing to the creation of mid gap energy levels within the band gap [88]. They explained that the major absorption onset of black TiO_2 was located at 0.6 eV. Also the band tail was blue shifted towards -0.3 eV. These observations pointed that surface disorder induced a striking band gap narrowing of 1.85 eV (Fig. 30) [88].

Microscopic techniques (SEM and TEM) were used to derive the morphology and defect states in black TiO_2. Different type of morphology such as mesoporous, nanoporous and core-shell nanostructures morphologies comprising nanotubes [124,98], plates [180], sheets [114,212,215], wires [140,141,225], films [117,129,181–183], fibers [171,184], inverse opals [164], spheres [106] arrays [185], cage [146], flower [137], leaves, spike [186], thorns [143], and belt [187], of black TiO_2 were formed as a result of different synthesis methods used for preparation. Some important morphologies obtained were shown in Fig. 31.

Black TiO_2 nanoparticles prepared through high pressure hydrogenation and high temperature aluminum reduction distinctly possessed a crystalline core/amorphous shell structure [154,110]. The amorphous shell consists of disordered surface layer containing oxygen vacancies whereas the crystalline core has trivalent titanium ions dispersed in it. The excellent optical absorption features correspond to the disordered surface layer and the consequent photocatalytic activities on crystalline core are the outcome of the synergy between the shell and the core [188]. The first report on black TiO_2 by Chen et al. clearly explained the defective surface layer of hydrogenated TiO_2 by using HRTEM (Fig. 1) [77]. Since then most of the researchers applied TEM and HRTEM as a supporting tool to explain the core-shell structure, usually crystalline core-amorphous shell structure [86,105,110]. *i.e.* the defects generally associated with the shell of a nanoparticle. Recently L. Li et al. observed microwave absorption features on black TiO_2 nanoparticles which possessed a unique core-shell structure. Prof. Geoffrey A. Ozin and coworkers reported comparatively thicker amorphous shell of TiO_{2-x} through Mg reduction method than that resulted in hydrogenation or aluminum reduction [138]. Our group have found the defect state within the core of the black TiO_{2-x} nanoparticle using HRTEM as shown in Fig. 32.

Xia et al. explained the surface defect states using HRTEM along with the line analysis [188]. From HRTEM image (Fig. 33A), white TiO_2 is completely crystalline with well-defined lattice fringes and the lattice fringe distance was found to be 3.536 Å which is characteristic of anatase phase and is uniform throughout the nanocrystals [188]. The statement is evident from the line analysis (Fig. 33C), whereas the black TiO_2 nanocrystal has a crystalline core and amorphous shell structure (Fig. 33B). The core shows clearly resolved (1 0 1) lattice plane of anatase with lattice fringe distance of 3.515 Å, which is consistent with the line analysis diagram (Fig. 33D). At the amorphous outer layer, the distances between adjacent lattice planes are highly distorted, *e.g.* 2.983 Å, 4.203 Å, and 6.747 Å (Fig. 33D) [188].

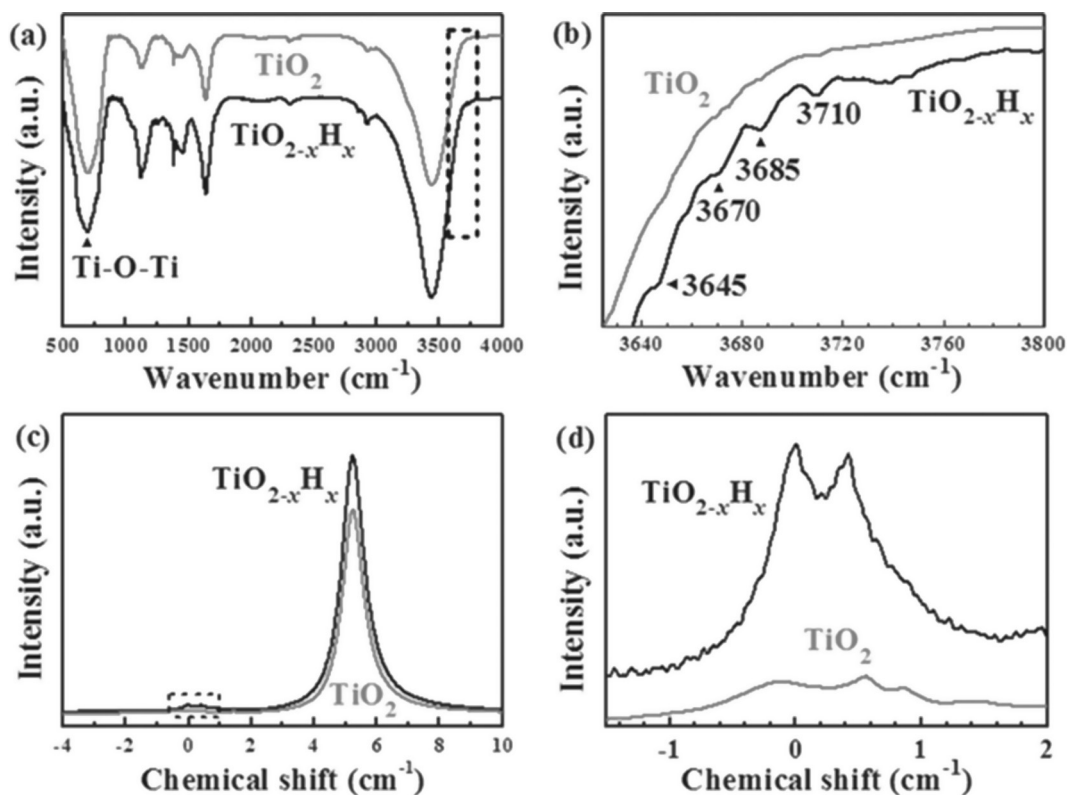**Fig. 27.** a & b) FTIR, c & d) ^{1}H NMR of pristine TiO_2 and $TiO_{2-x}H_x$ [102]. Reprinted with permission from Ref. [102]. Copyright 2013, Wiley-VCH.

W. Hu et al. could synthesize mesoporous black TiO_2 hollow nano spheres with highly crystalline pore-walls and surface disorders [189]. Surface disordered shell and Ti^{3+} dispersed in hollow structure frameworks imparted the enhanced optical absorption as well as suppression of recombination of charge carriers. Similar observations were also reported by K. Zang in which the mesoporous black TiO_2 nanosheets were synthesized using a low cost biotemplate [89]. Electro-conducting mesoporous anatase black TiO_2 nanoleaves were reported
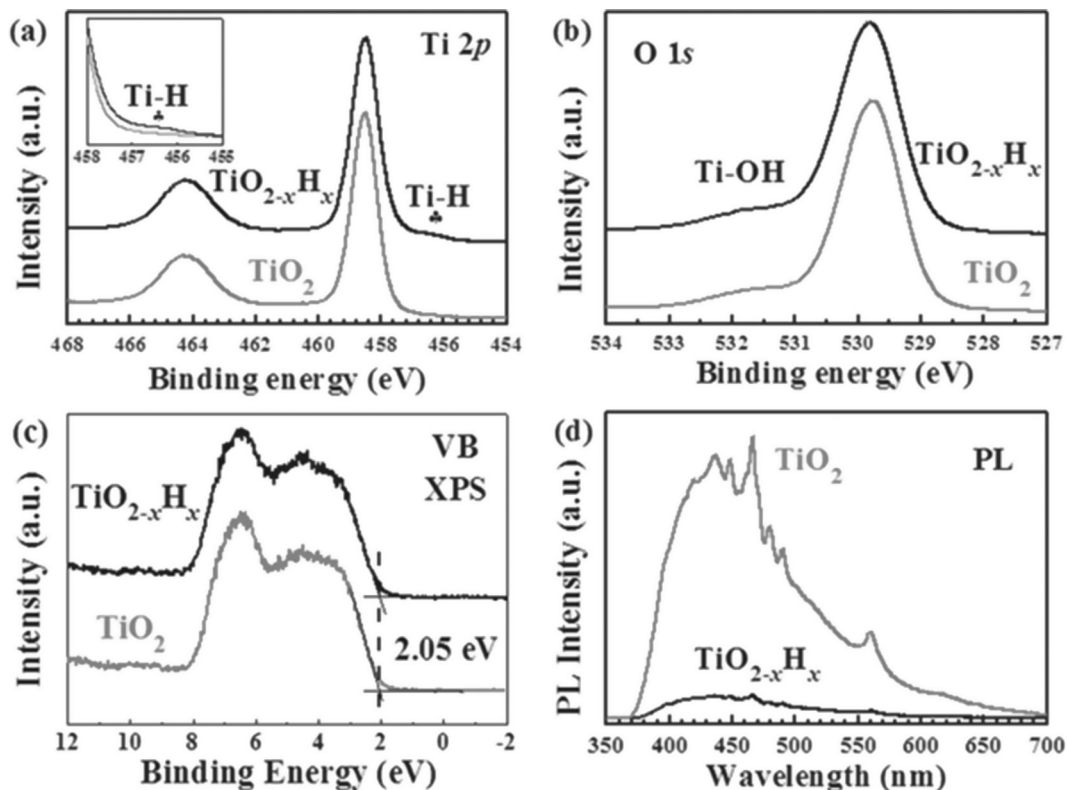
Fig. 28. a) Ti2p, b) O1s, c) VB XPS and d) PL spectra of pristine (TiO_2) and black ($TiO_{2-x}H_x$) [102]. Reprinted with permission from Ref. [102]. Copyright 2013, Wiley-VCH.
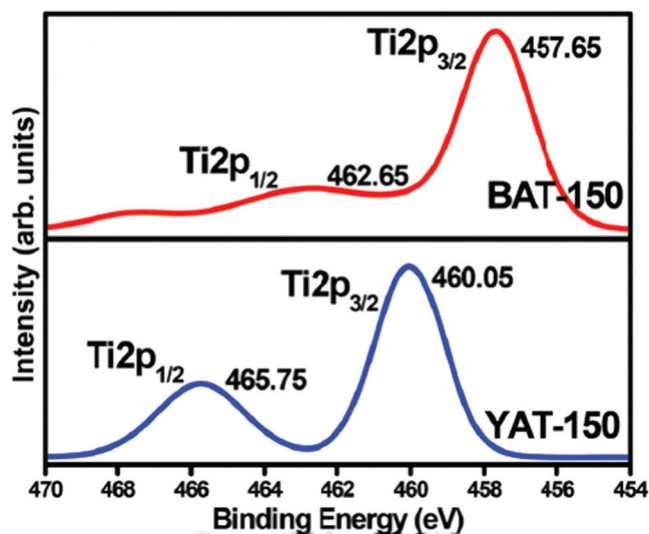
Fig. 29. Ti2p XPS of yellow anatase TiO_2 (YAT-150) and black anatase TiO_2 (BAT-150) synthesized by microwave irradiation [115]. Reprinted with permission from Ref. [109]. Copyright 2015, Royal Society of Chemistry. (For interpretation of the references to color in this figure legend, the reader is referred to the web version of this article.)

intertwined with each other losing their molecular hydrogen incorporation capability leading to a nanobelt morphology. Zhu et al. designed black TiO_2 nanocages having supreme optical absorption features consequent to the internal light trapping effect [146]. Additionally these nanocages possessed mesopores which facilitates the permeation of water vapor. Recently MoS_2 nanoflower coated nitrogen doped TiO_2 was reported [191]. It has a nanoflower ball morphology with core-shell structure. The effective separation of photogenerated charge carriers in N-TiO_{2-x}@MoS_2 was attributed to the synergistic effect of dopants and introduction of MoS_2.

Presence of Ti^{3+} in the crystal structure of black TiO_2 nanoparticles contributes to the enhanced the light harvesting capability [193–195]. As evidenced in several reports, the amorphous shell that surrounds the crystalline core is due to Ti^{3+} and/or V_o's [86,105]. Generally at higher temperature these defects states may disappear and the light harvesting capability, in particular the photocatalytic efficiency may be decreased. Recently an advanced TEM analysis was used by Tian et al. for investigating the structure and formation of black TiO_2 [196] where they used a pulsed laser vaporization (PLV) technique to synthesize amorphous ultra-small rutile nanoparticles followed by annealing at 970 K leading to rutile core-black Ti_2O_3 shell nanostructure (Fig. 34) [196]. From the atomic-resolution high-angle annular dark-field (HAADF) image of a rutile NP viewed in the (0 0 1) direction (Fig. 34. 1) showed that there was a transition region, connecting the disordered Ti_2O_3 shell to the perfect rutile core [196]. Nano beam electron diffraction (NBED) was also employed for further structural investigations (Fig. 34.2) and the rutile core structure exhibited a 4-fold symmetry which is the characteristic of perfect rutile. As the surface approached, both kinetically and dynamically forbidden reflections in pure rutile ({1 0 0} in the {0 0 1} zone axis) was appeared 2–4 nm away from the vacuum undoubtedly indicated the deviation of Ti from the octahedral symmetry and a trace amount of oxygen vacancies. Furthermore increased oxygen vacancy at the surface led towards the deviation from rutile phase represented by the rotation of (0 2 0) and (0 2 0) reflections [196].

Tominaka et al. has reported a topotactic reaction for the transformation of rutile-type TiO_2 to corundum-type Ti_2O_3 during low-temperature reduction [197]. This reaction successfully retained the crystal habit of the rutile parent as demonstrated by the conversion of TiO_2 nanorods into Ti_2O_3 nanorods. Unlike the Ti_2O_3 synthesized by conventional route, topotactically synthesized Ti_2O_3 exhibited a semi-metallic/metallic electronic conduction, which indicated that the method is promising to access narrow- or zero band gap titanium-based oxide materials which can be used in a variety of electronic applications [197].
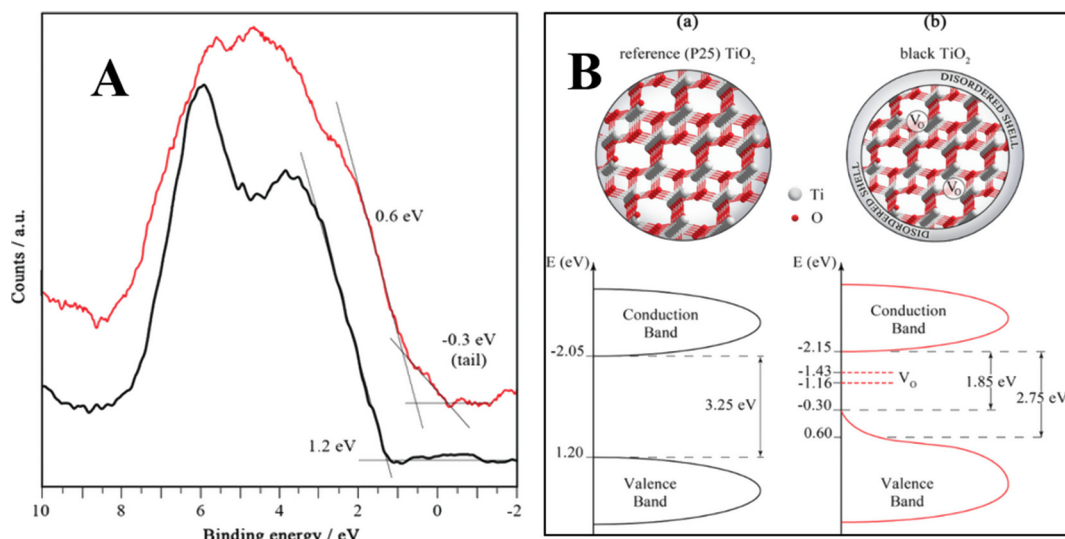
by Y. J. He [190]. They focused on its electrochemical applications and pointed out that the enhanced electro-conductivity is due to the presence of trivalent titanium ion. Prof. W. Zhou and coworkers fabricated three dimensional nanosheets formed out of MoS_2 sandwiched between black TiO_2 nanosheets [191]. The introduction of a layered oxide within the framework of the nanosheets significantly contributed to the efficient charge separation of photogenerated charge carriers [191].

Black TiO_2 nanowires were particularly noted for their large specific surface area and minimalized recombination rate for the photogenerated charge carriers due to limited diffusion distance as well as fast charge transport with the added advantage of enhanced optical absorption properties [192]. Black TiO_2 nanomaterials with a tubular morphology can be easily obtained even at low temperature and ambient pressure because pristine TiO_2 nanotubes have the capacity to store molecular hydrogen [98]. L. Han et al. synthesized anatase black TiO_2 nanotubes using hydrothermal method [98]. When the synthesis temperature was beyond 150 °C the anatase nanotubes started converted to black TiO_2-B nanobelts and at 210 °C complete transformation could be observed. As the temperature increases the nanotubes

Fig. 30. VB XPS, electronic structure and DOS of a) P25 b) black TiO_2 [88]. Reprinted with permission from Ref. [88]. Copyright 2012, American Chemical Society.
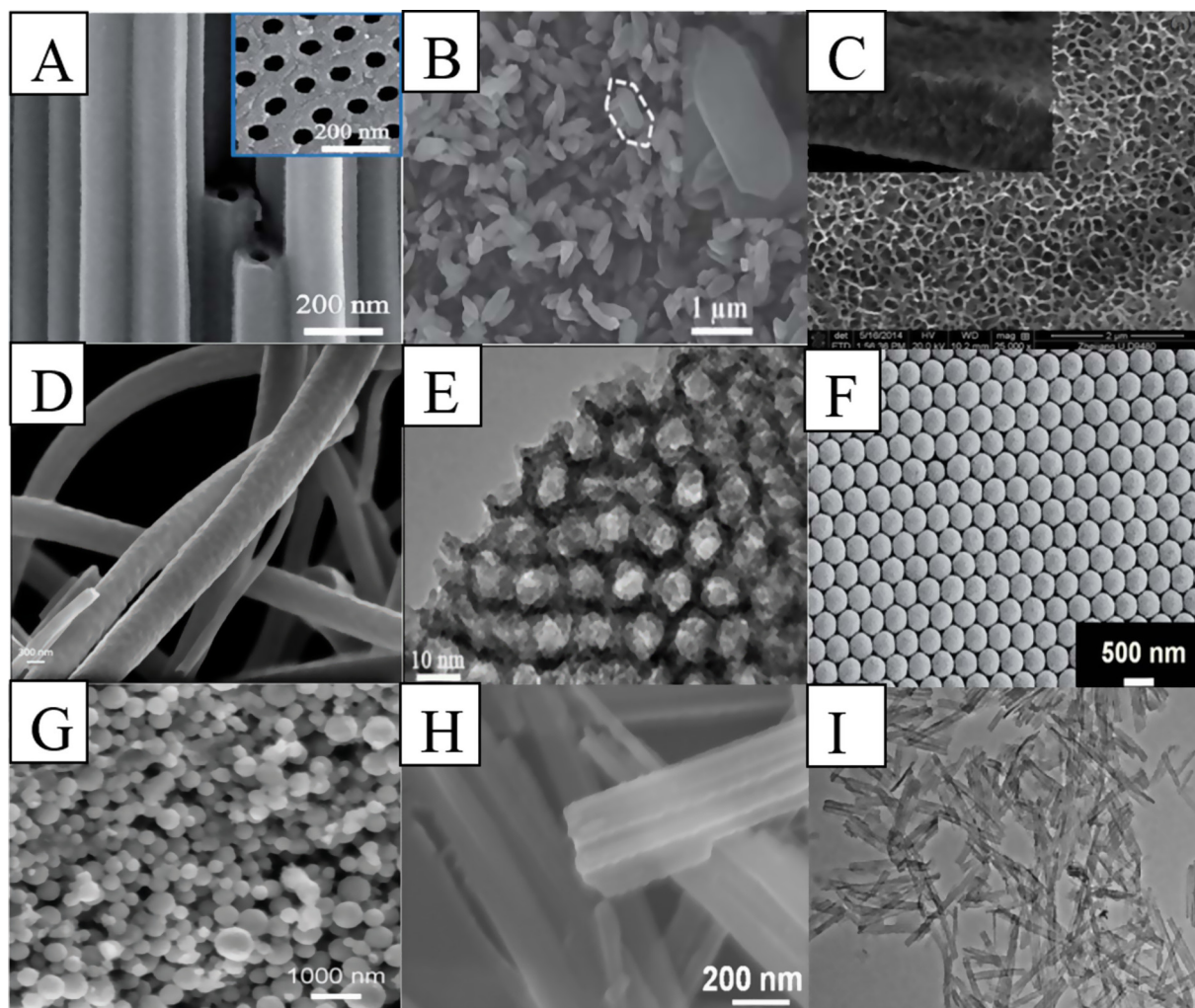
Fig. 31. SEM/TEM images of black TiO_2 with different morphologies. A) Nanotubes [124]. Reprinted with permission from Ref. [124]. Copyright 2014, Royal Society of Chemistry. B) Plates [180]. Reprinted with permission from Ref. [180]. Copyright 2013, Royal Society of Chemistry. C) films [181]. Reprinted with permission from Ref. [181]. Copyright 2015, Elsevier. D) fibers [171]. Reprinted with permission from Ref. [171]. Copyright 2015, American Chemical Society. E) core-shell nanostructure [184]. Reprinted with permission from Ref. [184]. Copyright 2014, American Chemical Society. F) inverse opals [164]. Reprinted with permission from Ref. [164]. Copyright 2015, Royal Society of Chemistry. G) spheres [106]. Reprinted with permission from Ref. [106]. Copyright 2014, Royal Society of Chemistry. H) belts [187]. Reprinted with permission from Ref. [187]. Copyright 2016, Elsevier. I) tubular structure [98]. Reprinted with permission from Ref. [98]. Copyright 2016, Royal Society of Chemistry.

5. Applications of black TiO_2

Nano TiO_2 and its modifications were studied extensively for its various functional applications [198–200]. Black TiO_2 is now one of the most attractive candidate in the area of photocatalysis, dye sensitized solar cells, supercapacitors, batteries and even in photothermal therapy mainly due to their wide area absorption and thereby narrowed band gap energy. Since it is one of the unequivocally established candidate in
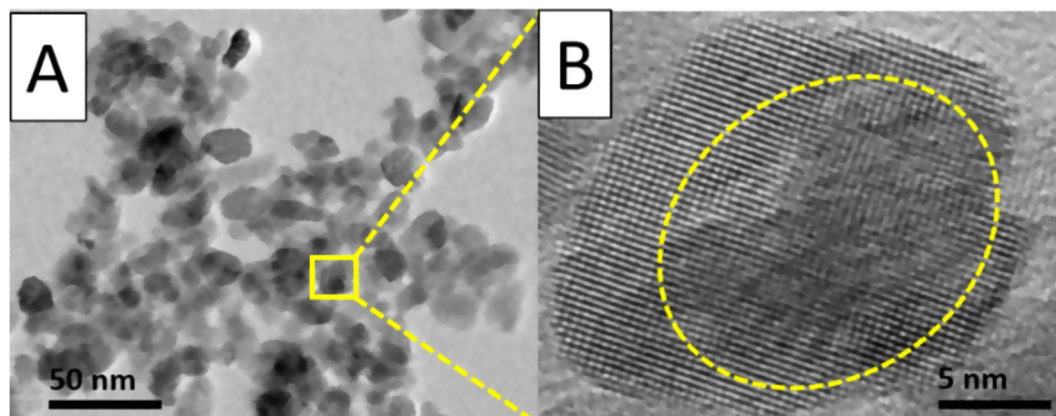

Fig. 32. A) TEM and B) HRTEM images of black TiO_{2-x} (defect is shown in the HRTEM image with black highlighting) [131]. Reprinted with permission from Ref. [131]. Copyright 2016, Royal Society of Chemistry.
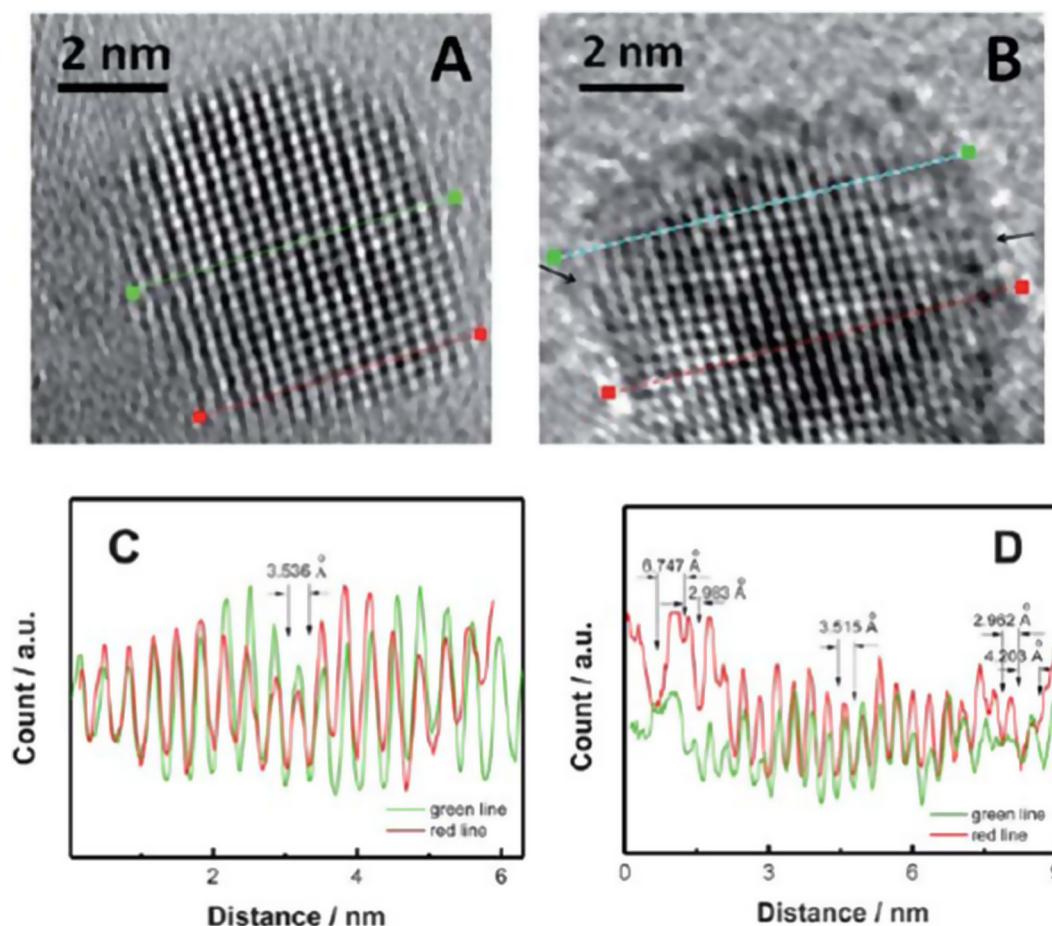
Fig. 33. HRTEM images of A) white TiO$_2$ and B) black TiO$_2$; line analysis of white TiO$_2$ (C) and line analysis of black TiO$_2$ (D). The red and green lines correspond to those in (A) and (B) [188]. Reprinted with permission from Ref. [188]. Copyright 2013, Royal Society of Chemistry. (For interpretation of the references to color in this figure legend, the reader is referred to the web version of this article.)

several applications, to date applications that has been reported on black TiO$_2$ are explicitly explained in the following sections.

5.1. Photodegradation

The first reported black TiO$_2$ by hydrogenation was employed in photodegradation of phenol and methylene blue [77]. Leshuk et al. also used methylene blue (MB) as model system for photocatalysis [85]. Ullattil et al. have demonstrated the oxygen vacancy rich black anatase TiO$_2$ for solar photocatalysis [115]. All these studies experimentally proved that the black anatase TiO$_2$ that has been synthesized was highly active than the commercially available photocatalyst Degussa-P25 for MB degradation. For example, Xin et al. reported a 30-fold enhancement in visible-light decomposition of methylene blue compared with the commercial sample P25 using black TiO$_2$ prepared by solvothermal assisted method [161].

The black plate like brookite TiO$_2$ with core/disordered shell structure (TiO$_2$ @ TiO$_{2-x}$) through Al reduction by Zhu et al. facilitated photodegradation under visible light towards the photodegradation of methylene blue (MB) and methyl orange (MO) [180]. MO degraded completely within 20 min under solar light irradiation and MB degraded 50% in 3 h under visible light using black brookite TiO$_2$ photocatalyst, points to the enhanced activity arised due to the modifications in TiO$_2$. Black TiO$_2$-B and black anatase TiO$_2$ have shown enhanced MO photodegradation as compared to commercially available P25 under visible light irradiation [94]. Wang et al. examined the photoactivity of black TiO$_2$ by using MO as model system in both acidic (pH 1) and in neutral (pH 7) media [160]. They have found that the

degradation rate in acid medium was more than to that in neutral medium as shown in Fig. 35. They have also analyzed the recyclability of the most efficient photocatalyst, T500 and found their intact activity even after five consecutive cycles [160].

Lin et al. have presented a series of nonmetal doped black TiO$_2$ nanoparticles for the photodegradation of methyl orange and H$_2$ generation [113]. Laser modified black TiO$_2$ nanostructures have shown enhanced photodegradation of rhodamine B dye whereas P25 has no photoactivity under the same experimental condition using a light source of green LED with 3.7 V voltage, 25 mA current and 520 nm wavelength [127]. By using a red LED (Voltage = 2 V, Current = 45 mA) result was the same but the photoactivity was decreased to a large extent for the black TiO$_2$ [127]. The same model system has been degraded by black TiO$_2$ that has been prepared by hydrogen plasma assisted chemical vapor deposition [103].

Samsudin et al. successfully employed the hydrogenated black TiO$_2$ nanoparticles for atrazine degradation [201]. The Al reduced black TiO$_2$ has found a tremendous photocatalyst for the degradation of MO and phenol [110]. According to Fan et al. hydroxylated TiO$_2$ prepared through ultrasonication demonstrated high photocatalytic activity for the degradation of acid fuchsin [126].

5.2. Hydrogen generation

Generating hydrogen, most ecofriendly fuel, from water using abundant solar radiation assisted by the complete solar spectrum absorption features of TiO$_2$ can be considered as a sustainable energy solution and many attempts were made to address its basic limitations,
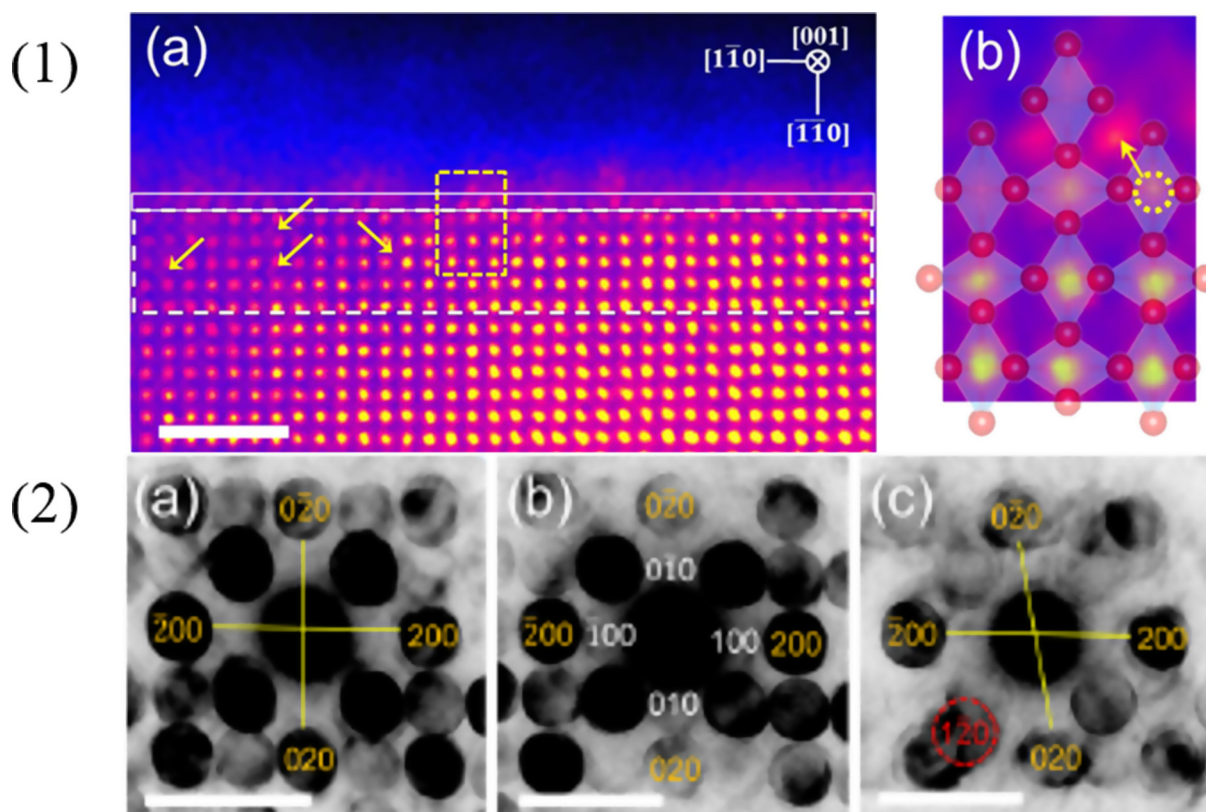
Fig. 34. (1a) HAADF image of a rutile NP viewed in the [0 0 1] direction (1b) magnified image from the area highlighted by dashed yellow rectangle in (a) (2a) NBED pattern of the core 2–4 nm away from vacuum of the rutile NP (b) NBED pattern of the near surface area showing the appearance of reflections forbidden in rutile designated by the white indices (c) NBED pattern of the surface area shows deviations from a standard rutile diffraction pattern in the rotation of the (0 2 0) and (0 $\bar{2}$ 0) reflections. An example of extra reflections marked by the red circle is attributed to defective Ti_2O_3 [196]. Reprinted with permission from Ref. [196]. Copyright 2015, American Chemical Society. (For interpretation of the references to color in this figure legend, the reader is referred to the web version of this article.)

viz, as wide band gap and rapid charge carrier recombination [202,203]. Black TiO_2 has been an unequivocally established as a potential candidate in the process of hydrogen generation *via* photocatalytic as well as photoelectrochemical route. Black TiO_2 possesses suitable band structure for hydrogen generation. The conduction band minimum of the black TiO_2 nanoparticles is thermodynamically and kinetically favorable for water reduction.

5.2.1. Photocatalytic water splitting by black TiO_2

After the identification of black TiO_2 as a potential candidate for photocatalysis, extensive studies were carried out to utilize its wide absorption features and efficient charge separation properties in hydrogen generation [204–208]. According to Wang et al. as the Al reduction temperature was increased, the amount of H_2 generation increased [110]. More specifically the hydrogen gas produced was 8.5 times to that of pristine TiO_2. The same black TiO_2 was found excellent photo electrochemical electrode that exhibited 1.7% solar to hydrogen efficiency [110]. Atmospheric H_2/Ar annealing was applied by Liu et al. for the synthesis of black TiO_2 nanotubes that showed a high open circuit photocatalytic hydrogen production rate [90]. After 20 days of high pressure hydrogen treatment on Degussa P25 paved the way to 3.94 mmol $g^{-1}h^{-1}H_2$ evolution rate in methanol solution [86].

Zhao et al. demonstrated black rutile nanorods through Zn reduction and the catalyst was generated H_2 from the water-methanol solution both under UV and visible light irradiation [162]. Zhou et al. achieved ordered mesoporous black TiO_2 with high thermal stability [184]. Here larger pore size and higher surface area of mesoporous black TiO_2 paved the way to high solar driven hydrogen production rate. The pristine mesoporous TiO_2 had shown a hydrogen production rate of 76.6 µmol h^{-1} whereas the ordered mesoporous black TiO_2

showed a larger production rate of 136.2 µmol h^{-1} which was almost twice to that of pristine mesoporous TiO_2. The cycling tests of the photocatalytic hydrogen generation under AM 1.5 and under visible light were also conducted to confirm the reusability of the photocatalyst. Lepcha et al. reported electro spun black TiO_2 nano fibers by hydrogen plasma treatment [171]. These nano fibers showed 10-fold more photo electrochemical performance than pristine TiO_2. Yang et al. reported an excellent H_2 production by S doping on a core-shell nanostructured black rutile TiO_2 [209]. The photocatalyst showed 1.67% solar to hydrogen conversion efficiency (Fig. 36) [209].

Black TiO_2 nanotube synthesized by Liu et al. introduced an effective and selective H implantation method on anatase TiO_2 and are highly beneficial for H_2 evolution [210]. Due to H implantation on these anatase single crystal (0 0 1) surfaces, specific defects were formed in addition to the defect states originated on nanotubes. Thereby a synergistic effect between implanted and implant free region was obtained. The ability of H implanted black TiO_2 nanotubes showed noble metal co-catalyst free photocatalytic hydrogen evolution. As the length of the nanotube increased, H_2 generation was also increased (Fig. 37) [210].

5.2.2. Photoelectrochemical (PEC) water splitting

The black TiO_2 nanowires prepared by Wang et al. showed notable photoelectrochemical water splitting property with Ag/AgCl system. Here also improved hydrogen generation was attributed to the enhanced charge separation and high charge density [87]. Core-shell black TiO_2 nanosheets obtained by NH_3 plasma had significant photocurrent density [211]. Similarly TiO_2 produced by electrochemical method and chemical reduction method reported to high photocurrent density and photoconversion efficiency [89,108].
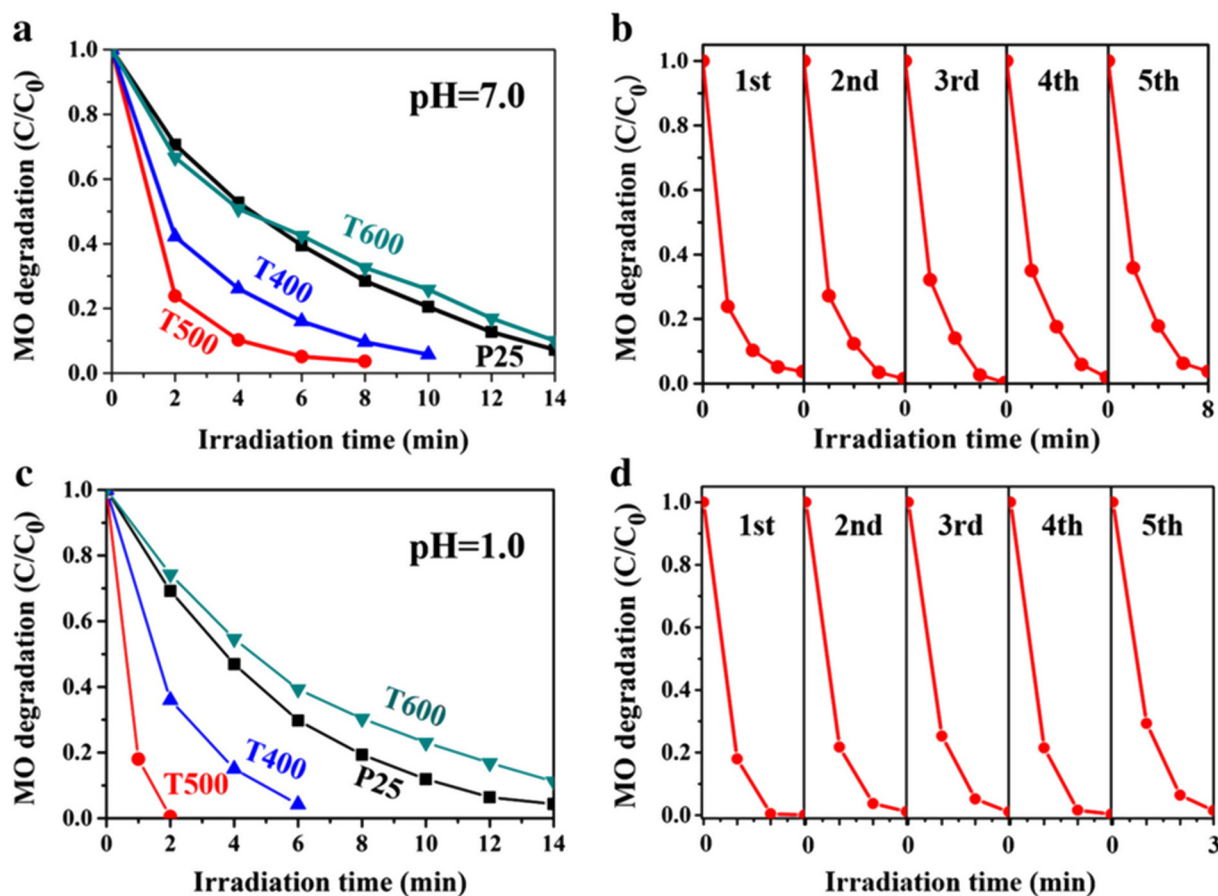
Fig. 35. Solar photocatalytic MO degradation using Black TiO₂ a) in neutral medium and b) corresponding recyclability c) in acid medium and d) corresponding recyclability [160]. Reprinted with permission from Ref. [160]. Copyright 2015, Elsevier.
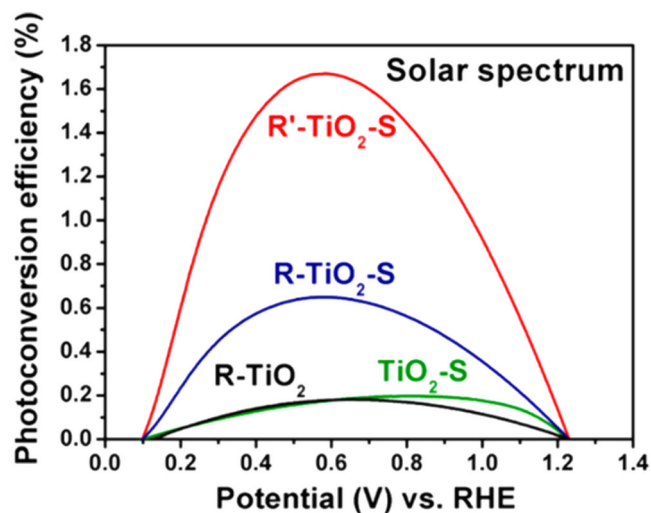

Fig. 36. Photoconversion efficiency *Vs* applied potential for R-TiO₂ (commercial rutile TiO₂), TiO₂-S (Sulphided commercial rutile TiO₂), R-TiO₂-S (obtained by Al reduction followed by H₂S treatment) and R'-TiO₂-S (obtained by Al reduction followed by H₂S treatment on anatase TiO₂) [209]. Reprinted with permission from Ref. [209]. Copyright 2013, American Chemical Society.

Fig. 37. (A) Photocatalytic H₂ production under open circuit conditions in methanol/water (50/50 vol%) of TiO₂ nanotube layers of different thickness illumination before and after H-implantation (measured under AM 1.5, 100 mW/cm²) (inset: photocatalytic H₂ production of (0 0 1) single crystal anatase before and after H-implantation), (gray box represent no detected hydrogen evolution, red box represents detectable amount of hydrogen evolution) [210]. Reprinted with permission from Ref. [210]. Copyright 2015, American Chemical Society. (For interpretation of the references to color in this figure legend, the reader is referred to the web version of this article.)

Apart from photoelectrochemical water splitting, black TiO₂ films were used for the photoreduction of CO₂ by Quingly et al. [181]. Due to wide area absorption and defect states present (Ti³⁺ and oxygen vacancies) of black TiO₂, selective formation of CO and CH₄ were occurred hundred times higher as compared to conventional TiO₂ (Degussa P25) (Fig. 38) [181]. Another important study is by pursuing
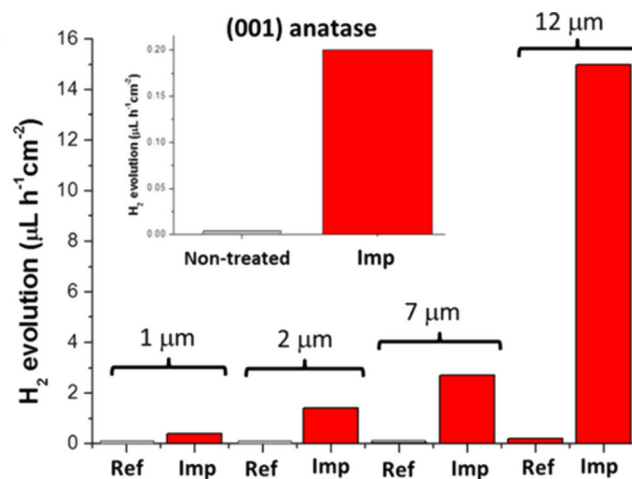
disorder engineering at the surface of 2D nanosheets of white TiO₂ by NaBH₄ treatment followed by calcination at 220–300 °C in N₂ atmosphere resulted black TiO₂ nanomaterials. Its photocurrent (80 μA cm⁻²) was four times more than that of the white TiO₂ and it
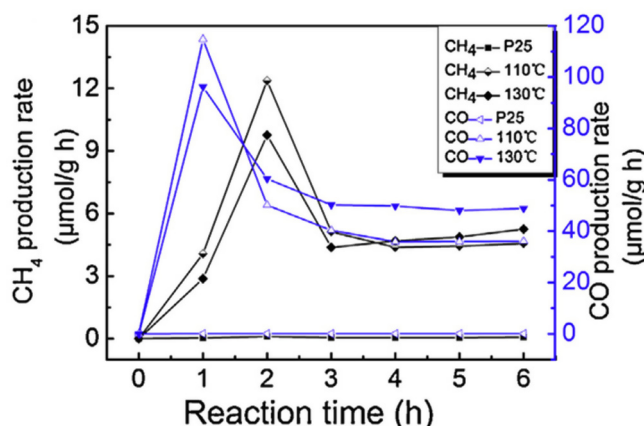
Fig. 38. CO and CH$_4$ production rates for TiO$_2$ (Degussa-P25) and TiO$_2$ film obtained on Ti plates treated at 110 °C and 130 °C [181]. Reprinted with permission from Ref. [181]. Copyright 2015, Elsevier.

presented a higher solar-driven hydrogen production rate of 400 µmol h^{-1} [212]. Hu et al. demonstrated a stable mesoporous black TiO$_2$ hollow spheres with relatively high surface area as compared to black TiO$_2$ nanoparticle has shown 241 mmol h^{-1} 0.1 g^{-1} solar driven hydrogen generation which was twofold and three fold more active than that of black TiO$_2$ nanoparticles and pristine TiO$_2$ hollow spheres respectively [189].

Recently black TiO$_2$ nanomaterials was used as a coating on Cu for improving CO$_2$ photoreduction [213]. The coating was used to restrain the rapid oxidation of Cu with surroundings. The photocatalytic activity for Cu@TiO$_2$ (~4%Cu) reaches 1.7 times of that for its counterpart, bare black TiO$_2$. The improved photoactivity is attributed to Cu embedded in TiO$_2$, which created oxygen vacancy sites within the lattice through metal-oxide interaction [213].

Annealing in air, annealing in nitrogen and balanced annealing using H$_2$-N$_2$ treatment on TiO$_2$ nanotube arrays were carried out by Carlson et al. for the bacterial disinfection of waterborne bacteria [214]. The absorption and efficiency was found more in the case of H$_2$-N$_2$ treated nanotube arrays (black TiO$_2$ nanotube) [214]. Black brookite single crystalline nanosheets were also employed in photocatalytic CO$_2$ reduction [215]. Here the excess Ti^{3+} defect states in the bulk of brookite nanosheets led the way to increased solar energy absorption and thereby increased photocatalytic activity [215].

5.3. Dye sensitized solar cells (DSSC)

Another important application of black TiO$_2$ was in field of DSSC. Recently black TiO$_{2-x}$ was employed in DSSC as a counter electrode individually and as composite of black TiO$_2$-x with carbon nanotube [216]. A photoconversion efficiency of 5.71% was achieved. The defective black TiO$_{2-x}$ showed wide area absorption (Fig. 39) and oxygen vacancies of TiO$_{2-x}$ extended the photo response of TiO$_2$ from the UV to the visible light region helped to improve the photoconversion efficiency. These defective black TiO$_{2-x}$ and composite TiO$_{2-x}$/CNT can be used as an effective alternative to the traditional Pt counter electrode in DSSC [216]. A very recent report showed that Mn^{2+} incorporation in TiO$_2$ nanoparticles has a black color and the resulted black TiO$_2$ alone has been efficiently worked as a photoanode material in DSSC [217].

5.4. Li ion batteries

Surface amorphized TiO$_2$ nanomaterials significantly contributed to enhance the performance of Li ion rechargeable battery [218–220]. Black TiO$_2$ nanomaterials are also considered as potential candidates for electrode material for Li ion batteries. Black TiO$_2$ obtained by the hydrogenation on normal white TiO$_2$ improved the electronic

conductivity and oxygen vacancy richness for its better application in Li ion batteries [92]. Yan et al. investigated the performance of fast Li storage of Ti^{3+} doped hydrogenated black TiO$_2$ [104]. The fast Li ion storage was due to the pseudocapacitive Li storage at the surface and the pseudocapacitive effect was due to the presence of defect states such as Ti^{3+} and oxygen vacancy states [104]. Myung et al. achieved black anatase TiO$_2$ with an electro-conducting Ti^{3+} (incorporation of H and N) [101]. This black anatase nanomaterial showed a very high electrical conductivity of 8×10^{-2} S cm^{-1}. The presence of the Ti^{3+} ion narrowed the band gap towards 1.8 eV that enabled a quick lodging of Li$^+$ into the anatase TiO$_2$ structure and subsequent extraction. The material shows promising retention percentage of discharge capacity in charge-discharge cycles [101].

Bae et al. reported different weight percentage of TiO$_{2-x}$ coated Si/SiO$_x$ nanosphere as anode material for Li ion battery [221]. The electroconductive TiO$_{2-x}$ coating enabled high coulombic efficiency, thermal reliability and reversible capacity. A very high reversible capacity of 1200 mAh g^{-1} with an extraordinary recycling rate up to 100 cycles was achieved. The TiO$_{2-x}$ layer art on the surface of Si/SiO$_x$ nanosphere can further take up more oxygen from the Si/SiO$_x$ phase leading to increase in coulombic efficiency and reversible capacity of the TiO$_{2-x}$ @ Si/SiO$_x$ nanosphere. This reductive nature enabled narrowed band gap that ensures sufficient electrical conductivity leading to higher efficiency (Fig. 40) [221].

TiO$_{2-x}$ nanotube arrays have been synthesized by Eom et al. through thermal conversion treatment of amorphous TiO$_2$ nanotubes under hydrogen atmosphere were implemented as an efficient material for Li ion batteries due to their high electronic conductivity facilitated by increased defect states of oxygen vacancies and Ti^{3+} ions [185].

5.5. Na ion batteries

Resembling high concentration of oxygen vacancy sites and Na ion diffusion length in the nanostructure, black TiO$_2$ was employed as an anode in sodium-ion batteries [222]. The black TiO$_2$ that has been synthesized was occupied with oxygen vacancies both at the surface and in bulk. A high reversible specific capacity of 207.6 mAh g^{-1} at 0.2C, retained 99.1% over 500 cycles at 1C and still maintained 91.2 mAh g^{-1} even at the high rate of 20C. After the charge-discharge process of over 500 cycles at 1C, the capacity of 185.1 mAh g^{-1} was maintained with a retention of as high as 99.1%, indicating a long cycling stability. Here lower sodiation energy barrier of anatase with oxygen vacancies enabled a more favorable Na intercalation into black anatase TiO$_2$ [222].

5.6. Al ion batteries

Black mesoporous anatase TiO$_2$ nanoleaves synthesized *via* solution plasma processing was employed in Al ion batteries by He et al. [190]. The initial charge capacity of TiO$_2$ nanoleaves corresponding to Al$_{0.27}$TiO$_2$ was comparatively higher (278.1 mA h g^{-1}) than that of anatase TiO$_2$ nanotube arrays. Black TiO$_2$ nanoleaves possessed a high Al^{3+} storage performance as a consequence of ordered nanoparticles which enhances the bulk intercalation and the interfacial storage capacities. In addition to this, they compared the rate performance of commercial white anatase TiO$_2$ and black anatase TiO$_2$ nanoleaves at a current density of 0.1 A g^{-1}, the reversible rate capacity of commercial white TiO$_2$ is 62.6 mA h g^{-1} and that of black TiO$_2$ nanoleaves is 259.7 mA h g^{-1} with excellent recyclability (Fig. 41). This superior reversible rate capacity of black TiO$_2$ was associated with the conductive Ti^{3+} which enables the fast electron transfer [190].

5.7. Supercapacitors

Highly ordered black TiO$_2$ nanotube arrays demonstrated a highly efficient electrode material for supercapacitors [122]. Self-doped black
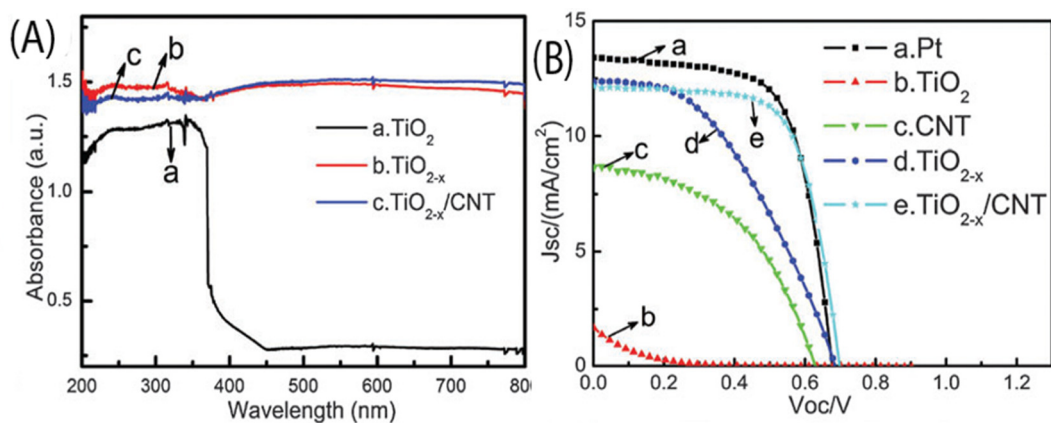
Fig. 39. Absorption spectra and B) photocurrent-voltage (J-V) curves of DSSC based on TiO_2, TiO_{2-x}, TiO_{2-x}/CNT, CNT and Pt [216]. Reprinted with permission from Ref. [216]. Copyright 2015, Royal Society of Chemistry.

TiO_2 with narrowed band gap energy and thus low resistivity enabled highly efficient supercapacitor. Here as a result of this electrochemical doping, a nearly rectangular-shaped cyclic voltagramme were obtained for the TiO_2 samples comparable with ideal capacitors [223]. Black TiO_2 nanotube arrays synthesized by Kim et al. used as a supercapacitor as well as an oxidant generating anode [224]. The comparison of pristine TiO_2 with this black TiO_2 using cyclic voltammograms (Fig. 42) revealed a significantly higher charging current for black TiO_2 than the pristine TiO_2. It is well clear that oxygen was evidently generated on the black TiO_2 under a potential of 1.2 V, whereas no oxygen evolution reaction was observed on the pristine TiO_2. These studies proved that the potential of black TiO_2 both as a supercapacitor and an oxidant generating anode [224]. Zhi et al. fabricated a solid state super-capacitor (ASSSC) using black $TiO_{2-x:N}$ decorated 2D NiO nanosheets

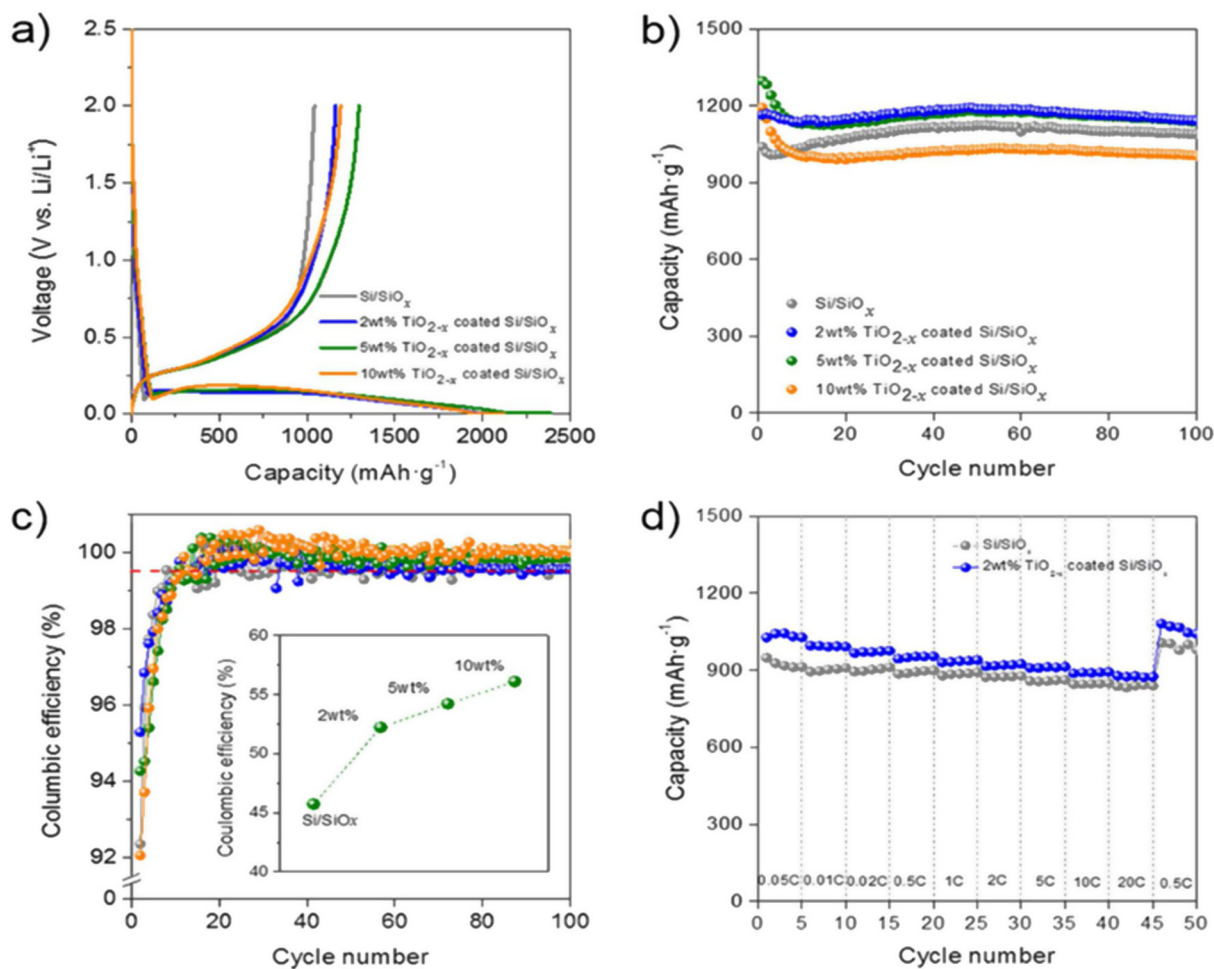**Fig. 40.** Electrochemical performance of TiO_{2-x} coated Si/SiO_x nanospheres compared to pristine Si/SiO_x nanosphere (a) galvanostatic voltage profiles in the voltage range of 0.01–2.0 V *Vs* Li/Li^+ at a constant current density of 0.05C (50 mAg^{-1}) for first cycle (b) cycle performance and (c) Coulombic efficiencies of TiO_{2-x} coated Si/SiO_x nanospheres during 100 cycles compared to pristine Si/SiO_x nanosphere and (d) rate capabilities of 2 wt% TiO_{2-x} coated Si/SiO_x nanosphere and pristine Si/SiO_x nanosphere at different current densities (1C = 1000 mAg^{-1}) [221]. Reprinted with permission from Ref. [221]. Copyright 2016, American Chemical Society.
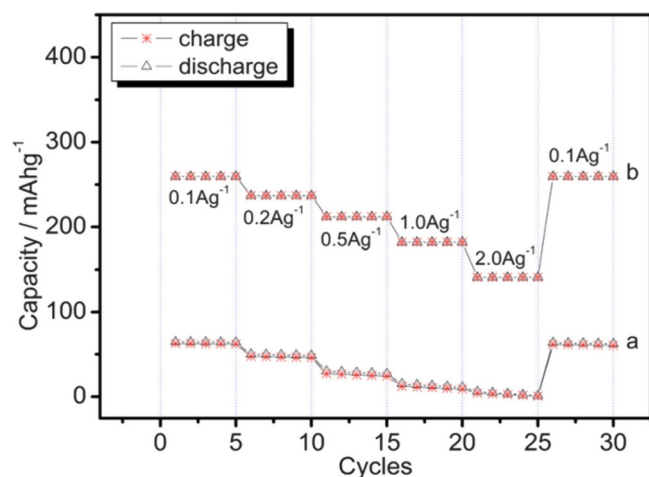
Fig. 41. Rate performance of (a) commercial white anatase TiO_2 and (b) black anatase TiO_2 nanoleaves electrodes at different current rates [190]. Reprinted with permission from Ref. [190]. Copyright 2014, Royal Society of Chemistry.
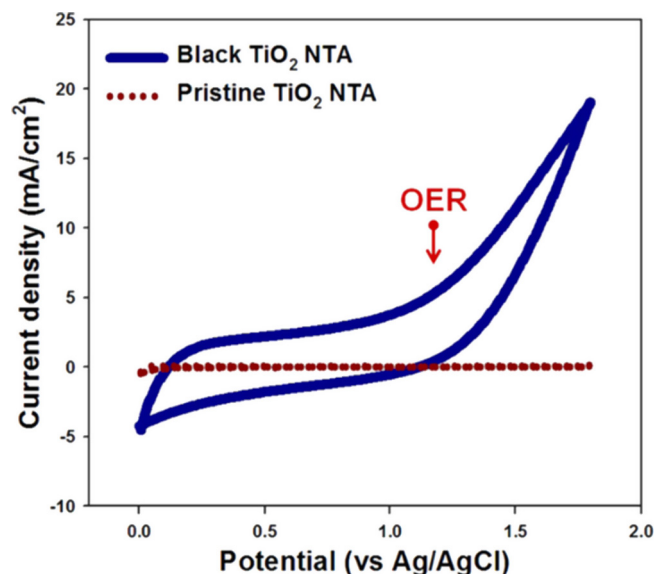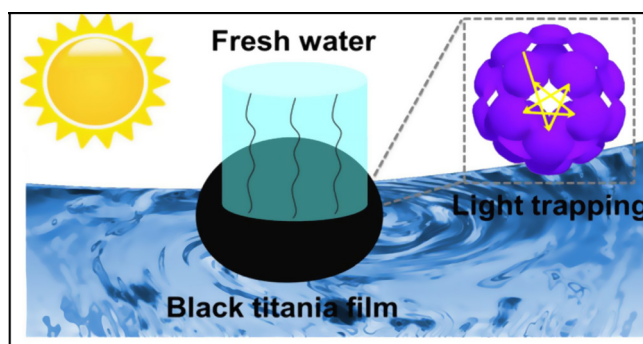

Fig. 44. Schematic representation of solar desalination [146]. Reprinted with permission from Ref. [146]. Copyright 2016, American Chemical Society.

as positive electrode and mesoporous graphene as negative electrode (Fig. 43) [112]. The 2D NiO nanosheets were pseudocapacitive material and black $TiO_{2-x:N}$ as conductive agent. This flexible ASSSC possessed a high energy density of 47 Wh kg^{-1} in a voltage region 0–1.6 V [112].

5.8. Surface enhanced Raman active Scattering (SERS) substrate

Y. Shan et al. introduced wafer scale silver deposited black TiO_2 nanowires as substrates for Surface-Enhanced Raman Scattering (SERS) technique [225]. The material induced superior chemical enhancement compared to other semiconductors and comparable to the noble metal substrates.

5.9. Solar desalination

G. Zhu et al. designed black TiO_2 nanocages with mesopores for water desalination. Solar desalination is the universal accepted method which will effectively address water scarcity problem [146]. Solar desalination works on the principle air-water interface solar heating. Here solar irradiation is selectively absorbed by the air-water interface thereby eliminating bulk heating of water. These material possessed enhanced absorption due to light trapping effect of the nanocage morphology. The well crystallized nanograins associated with the nanocages promoted heat transfer from titania to water. Along with the mesopores induced the permeation of water vapor with an added advantage of light to heat conversion. The process is schematically represented in Fig. 44. M. Ye et al. also developed black TiO_2 nanoparticles for desalination through solar water evaporation [138]. They conducted experiment with black TiO_2 coated on a stainless steal mesh followed by superhydrophobization through fluoroalkylation and finally solar water evaporation was achieved [138].
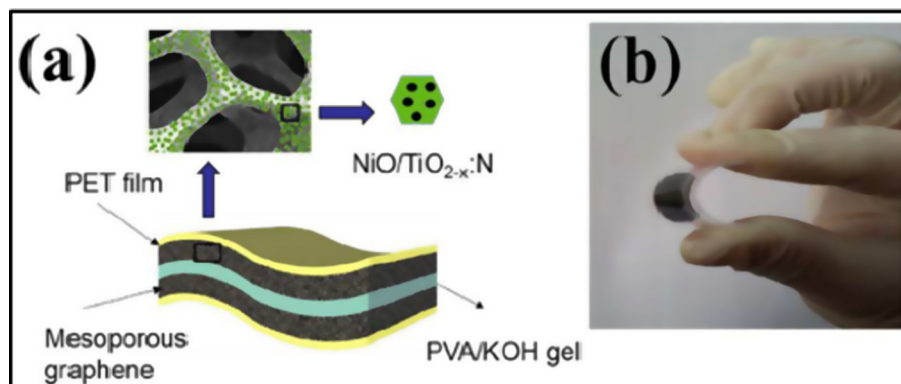

Fig. 42. Cyclic voltammograms of black TiO_2 NTA and pristine TiO_2 NTA obtained at a scan rate of 100 mV/s ([KH_2PO_4]$_o$ = 1 M with NaOH (pH = 7.2)) [224]. Reprinted with permission from Ref. [224]. Copyright 2015, American Chemical Society.

Fig. 43. (a) Schematic illustration of a flexible supercapacitor using as NiO/TiO_{2-x}:N composites and mesoporous graphene as positive and negative electrodes (b) Photo of the fabricated flexible supercapacitor in bending states [112]. Reprinted with permission from Ref. [112]. Copyright 2016, Royal Society of Chemistry.
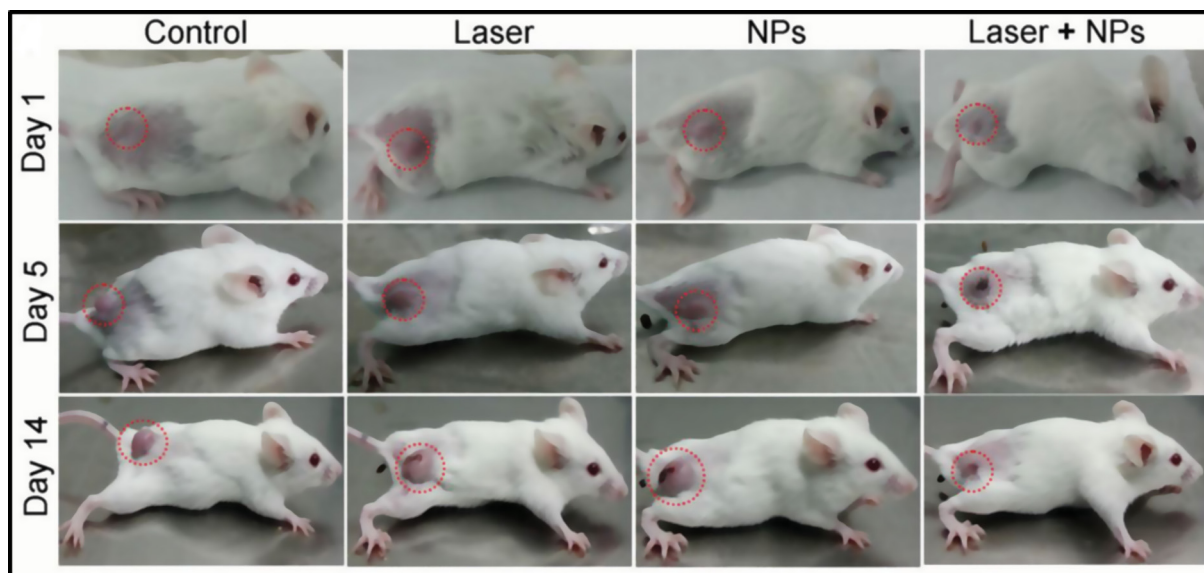
Fig. 45. Photos of 4 T1 tumor-bearing mice at 1st, 5th and 14th day after treatment with and without black TiO$_2$ nanoparticles (NPs) in the presence/absence of laser irradiation [226] Reprinted with permission from Ref. [226]. Copyright 2015, Wiley-VCH.

5.10. Photothermal therapy

Ren et al. used black hydrogenated TiO$_2$ as photothermal agent for cancer photothermal therapy [226]. To increase its stability in physiological environment, polyethylene glycol (PEG) coating was implemented and a photothermal conversion efficiency of 40.8% was achieved. The toxicity and cancer therapy effect of polyethylene glycol (PEG) coated black TiO$_2$ was evaluated *in vitro* and *in vivo*. Systematic studies revealed that the infrared-irradiated PEG coated black TiO$_2$ exhibited low toxicity, high efficiency as a photothermal agent for cancer therapy. Its toxicity was evaluated *in vivo* in mice and found no significant changes in its routine and internal organs. By applying tumor cells (4T1 cell line of murine breast cancer) in mice, the PTT activity was examined and found interestingly that the tumor cells were disappeared after 14 days of treatment using PEG coated black TiO$_2$ along with laser (Fig. 45) [226]. Another important study in this field was reported by Mou *et. al.* where a single NIR laser (wavelength = 808 nm, power density = 1 Wcm^{-2}) induced multifunctional theranostic nano platform based on black TiO$_{2-x}$ has been constructed for dual-modal imaging-guided cancer therapy both *in vitro* and *in vivo* [227]. The tumor was completely eliminated in 2 days with no recurrence for 20 days investigation, attributed to the photothermal-photodynamic synergistic effect [227].

6. Summary and outlook

As the growing interest of the scientific community towards the renewable energy resources, especially sun light, fueled the exploration of black TiO$_2$ as an excellent sunlight harvester. Its applications in many other areas are also emerged. Various synthetic strategies of black TiO$_2$ nanomaterials have been developed and each method has its own advantage in designing its morphology, optical and functional properties. Origin of black coloration, presence of defects and their applications in various fields such as photodegradation, solar water splitting for hydrogen generation, dye sensitized solar cells, supercapacitors, batteries and therapeutics have been reviewed. Irrespective of the presence or absence of defective surface layer of black TiO$_2$, it can obviously act as a light harvester due to its wide area absorption from UV region to IR region. In addition, its use in medicinal applications namely in photothermal and photodynamic theranostics may lead to an effective and tremendous material having applications in all hot areas. Black TiO$_2$

nanomaterials is appeared as the right candidate which can absorb the entire solar spectrum from UV to IR region, may in future will lead towards the maximum technological development, particularly in the area of sunlight harvesting. In addition, the confinement of midgap states in black TiO$_2$ provides trapping centres for photogenerated charge carriers which inhibits the recombination, thereby enhancing the catalytic activity beneficial for the environmental and energy related applications. Novel applications of black TiO$_2$ are arising continuously. Black TiO$_2$ is identified as Microwave Absorbing Materials (MAMs). The symbiosis of crystalline-core and amorphous-shell in black TiO$_2$ attributes the origin of microwave absorption [128]. The similar feature was also utilized in designing Surface Enhanced Raman Scattering (SERS) Substrate in which the enhancement of the photogenerated charge carrier density reinforces the chemical and electromagnetic characteristics [225]. Another remarkable achievement is in the field of Self-Cleaning Coatings through photocatalytic disinfection [228]. Since the ultimate utilization of the universal energy source, sunlight, is a tedious one, we hope that a black TiO$_2$ material can be able to fulfill the energy needs of the present scenario. Therefore, further attention should be given to the performance of black TiO$_2$ in real industrial practice to develop new technologies.

Acknowledgements

References

[1] P. Moriarty, D. Honnery, Renewable Sustainable Energy Rev. 16 (2012) 244.
[2] N. Lior, Energy 35 (2010) 3976.
[3] A. Blakers, Asian Perspect. 39 (2015) 559.
[4] V. Balzani, A. Credi, M. Venturi, ChemSusChem 1 (2008) 26.
[5] S. Chu, A. Majumdar, Nature 488 (2012) 294.
[6] P.V. Kamat, J. Phys. Chem. C 111 (2007) 2834.
[7] J. Schneider, M. Matsuoka, M. Takeuchi, J. Zhang, Y. Horiuchi, M. Anpo, D.W. Bahnemann, Chem. Rev. 114 (2014) 9919.
[8] F. Zang, J. Zhao, T. Shen, H. Hidaka, E. Pelizzetti, N. Serpone, Appl. Catal. B: Environ. 15 (1998) 147.
[9] C. Chen, X. Li, W. Ma, J. Zhao, J. Phys. Chem. B 106 (2002) 318.
[10] W. Li, D. Li, Y. Lin, P. Wang, W. Chen, X. Fu, Y. Shao, J. Phys. Chem. C 116 (2012) 3552.
[11] J. Tian, Z. Zhao, A. Kumar, R.I. Boughton, H. Liu, Chem. Soc. Rev. 43 (2014) 6920.
[12] P. Roy, D. Kim, K. Lee, E. Spiecker, P. Schmuki, Nanoscale 2 (2010) 45.
[13] F. Sauvage, F. Di Fonzo, A. Li Bassi, C.S. Casari, V. Russo, G. Divitini, C. Ducati,

C.E. Bottani, P. Comte, M. Graetzel, Nano Lett. 10 (2010) 2562.

[14] W.-Q. Wu, B.-X. Lei, H.-S. Rao, Y.-F. Xu, Y.-F. Wang, C.-Y. Su, D.-B. Kuanga, Sci. Rep. 3 (2013) 1352.

[15] S. Banerjee, D.D. Dionysiou, S.C. Pillai, Appl. Catal. B: Environ. 176 (2015) 396.

[16] M.J. Powell, R. Q-Cabrera, A. Taylor, D. Teixeira, I. Papakonstantinou, R.G. Palgrave, G. Sankar, I.P. Parkin, Chem. Mater. 28 (2016) 1369.

[17] A. Khataee, L. Moradkhannejhad, V. Heydari, B. Vahid, S.W. Joo, Pigm. Resin Technol. 45 (2016) 24.

[18] G. Doganli, B. Yuzer, I. Aydin, T. Gultekin, A. Con, H. Selcuk, S. Palamutcu, Coat. Technol. Res. 13 (2016) 257.

[19] Y. Lai, J. Huang, Z. Cui, M. Ge, K.-Q. Zhang, Z. Chen, L. Chi, Small 12 (2016) 2203.

[20] Y.H. Hu, Angew. Chem. Int. Ed. 51 (2012) 12410.

[21] A.J. Cowan, J. Tang, W. Leng, J.R. Durrant, D.R. Klug, J. Phys. Chem. C 114 (2010) 4208.

[22] B. Chen, J. Hou, K. Lu, Langmuir 29 (2013) 5911.

[23] J. Yu, L. Qi, M. Jaroniec, J. Phys. Chem. C 114 (2010) 13118.

[24] J. Galińska, J. Walendziewski, Energy Fuels 19 (2005) 1143.

[25] J.H. Park, S. Kim, A.J. Bard, Nano Lett. 6 (2006) 24.

[26] X. Lang, X. Chen, J. Zhao, Chem. Soc. Rev. 43 (2014) 473.

[27] A. Haarstrick, O.M. Kut, E. Heinzle, Environ. Sci. Technol. 30 (1996) 817.

[28] Y. Lin, D. Li, J. Hu, G. Xiao, J. Wang, W. Li, X. Fu, J. Phys. Chem. C 116 (2012) 5764.

[29] T.V. Pho, M.V. Sheridan, Z.A. Morseth, B.D. Sherman, T.J. Meyer, J.M. Papanikolas, K.S. Schanze, K.R. Reynolds, ACS Appl. Mater. Interfaces 8 (2016) 9125.

[30] J. Chen, J. Zhang, Y. Xian, X. Ying, M. Liu, L. Jin, Water Res. 39 (2005) 1340.

[31] C.C. Evans, C. Liu, J. Suntivich, ACS Photonics 3 (2016) 1662.

[32] G.S. Aluri, A. Motayed, A.V. Davydov, V.P. Oleshko, K.A. Bertness, N.A. Sanford, M.V. Rao, Nanotechnology 22 (2011) 295503.

[33] A. Haidry, P. Schlosser, P. Durina, M. Mikula, M. Tomasek, T. Plecenik, T. Roch, A. Pidik, M. Stefecka, J. Noskovic, M. Zahoran, Open Phys. 9 (2011) 1351.

[34] X. Zhang, J. Zhang, Y. Jia, P. Xiao, J. Tang, Sensors 12 (2012) 3302.

[35] Q. Zheng, B. Zhou, J. Bai, L. Li, Z. Jin, J. Zhang, J. Li, Y. Liu, W.E.I.M.I.N. Cai, X.I.N.Y.U.A.N. Zhu, Adv. Mater. 20 (2008) 1044.

[36] V. Etacheri, C. Di Valentin, J. Schneider, D.W. Bahnemann, S.C. Pillai, J. Photochem. Photobiol. C: Photochem. Rev. 25 (2015) 1.

[37] A.S. Barnard, P. Zapol, L.A. Curtiss, J. Chem. Theory Comput. 1 (2005) 107.

[38] H. Shi, R. Magaye, V. Castranova, J. Zhao, Part. Fibre Toxicol. 10 (2013) 15.

[39] P. Tao, Y. Li, A. Rungta, A. Viswanath, J. Gao, B.C. Benicewicz, R.W. Siegel, L.S. Schadler, J. Mater. Chem. 21 (2011) 18623.

[40] F.W. Mont, J.K. Kim, M.F. Schubert, E.F. Schubert, R.W. Siege, J. Appl. Phys. 103 (2008) 083120.

[41] D.O. Scanlon, C.W. Dunnill, J. Buckeridge, S.A. Shevlin, A.J. Logsdail, S.M. Woodley, C.R.A. Catlow, M.J. Powell, R.G. Palgrave, I.P. Parkin, G.W. Watson, Nat. Mater. 12 (2013) 798.

[42] N. Serpone, J. Phys. Chem. B 110 (2006) 24287.

[43] R. Levinson, P. Berdahl, H. Akbari, Sol. Energy Mater. Sol. Cells 89 (2005) 319.

[44] R. Asahi, Y. Taga, W. Mannstadt, A.J. Freeman, Phys. Rev. B 61 (2000) 7459.

[45] S.C. Pillai, P. Periyat, R. George, D.E. McCormack, M.K. Seery, H. Hayden, J. Colreavy, D. Corr, S.J. Hinder, J. Phys. Chem. C 111 (2007) 1605.

[46] P. Periyat, K.V. Baiju, P. Mukundan, P.K. Pillai, K.G.K. Warrier, J. Sol-Gel Sci. Technol. 43 (2007) 299.

[47] R. Asahi, T. Morikawa, H. Irie, T. Ohwaki, Chem. Rev. 114 (2014) 9824.

[48] S.A. Ansari, M.M. Khan, M.O. Ansari, M.H. Cho, New J. Chem. 40 (2016) 3000.

[49] G. Li, L. Chen, N.M. Dimitrijevic, K.A. Gray, Chem. Phys. Lett. 45 (2008) 75.

[50] H. Wang, J.P. Lewis, J. Phys..: Condens. Matter 18 (2006) 421.

[51] X. Chen, C. Burda, J. Am. Chem. Soc. 130 (2008) 5018.

[52] Y. Zhou, C. Chen, N. Wang, Y. Li, H. Ding, J. Phys. Chem. C 120 (2016) 6116.

[53] J. Zheng, Y. Liu, G. Ji, P. Zhang, X. Cao, B. Wang, C. Zhang, X. Zhou, Y. Zhu, D. Shi, ACS Appl Mater. Interfaces 7 (2015) 23431.

[54] Q. Zhu, Y. Peng, L. Lin, C.M. Fan, G.Q. Gao, R.X. Wang, A.W. Xu, J. Mater. Chem. A 2 (2014) 4429.

[55] Z. Pei, L. Ding, W. Feng, S. Weng, P. Liu, PCCP 16 (2014) 21876.

[56] J. Qiu, S. Li, E. Gray, H. Liu, Q.F. Gu, C. Sun, C. Lai, H. Zhao, S. Zhang, J. Phys. Chem. C 118 (2014) 8824.

[57] G. Zhu, Y. Shan, T. Lin, W. Zhao, J. Xu, Z. Tian, H. Zhang, C. Zheng, F. Huang, Nanoscale 8 (2016) 4705.

[58] E. Omurzak, T. Mashimo, C. Iwamoto, Y. Matsumoto, S. Sulaimankulova, J. Nanosci. Nanotechnol. 9 (2009) 6372.

[59] Y. Chen, Y. Xu, S. Jiao, X. Wang, L. Li, Z. Fang, S. Feng, Dyes Pigm. 129 (2016) 191.

[60] J. Zheng, G. Ji, P. Zhang, X. Cao, B. Wang, L. Yu, Z. Xu, Chem. Eur. J. 21 (2015) 18309.

[61] L. Kong, C. Wang, H. Zheng, X. Zhang, Y. Liu, J. Phys. Chem. C 119 (2015) 16623.

[62] S. Sakthivel, M. Janczarek, H. Kisch, J. Phys. Chem. B 108 (2004) 19384.

[63] M. Wang, B. Nie, K.K. Yee, H. Bian, C. Lee, H.K. Lee, B. Zheng, J. Lu, L. Luo, Y.Y. Li, Chem. Commun. 52 (2016) 2988.

[64] M. Xing, J. Zhang, B. Qiu, B. Tian, M. Anpo, M. Che, Small 2015 (1920) 11.

[65] J. Zhao, L. Zhang, W. Xing, K. Lu, J. Phys. Chem. C 119 (2015) 7732.

[66] G. Liu, L.C. Yin, J. Wang, P. Niu, C. Zhen, Y. Xie, H.M. Cheng, Energy Environ. Sci. 5 (2012) 9603.

[67] C. Sun, D.J. Searles, J. Phys. Chem. C 117 (2013) 26454.

[68] X. Yu, B. Kim, Y.K. Kim, ACS Catal. 3 (2013) 2479.

[69] G. Li, Z. Zhang, H. Peng, K. Chen, RSC Adv. 3 (2013) 11507.

[70] X. Zou, J. Liu, J. Su, F. Zuo, J. Chen, P. Feng, Chem. Eur. J. 19 (2013) 2866.

[71] D. Cronemeyer, M. Gilleo, Phys. Rev. 82 (1951) 975.

[72] L. Tian, J. Xu, M. Just, M. Green, L. Liu, X. Chen, J. Mater. Chem. C 5 (2017) 4645.

[73] T. Xia, Y. Cao, N.A. Oyler, J. Murowchick, L. Liu, X. Chen, ACS Appl Mater. Interfaces 7 (2015) 10407.

[74] L. Tian, X. Yan, J. Xu, P. Wallenmeyer, J. Murowchick, L. Liu, X. Chen, J. Mater. Chem. A 3 (2015) 12550.

[75] T. Xia, C. Zhang, N.A. Oyler, X. Chen, J. Mater. Res. 29 (2014) 2198.

[76] T. Xia, C. Zhang, N.A. Oyler, X. Chen, Adv. Mater. 25 (2013) 6905.

[77] X. Chen, L. Liu, Y.Y. Peter, S.S. Mao, Science 331 (2011) 746.

[78] X. Chen, L. Liu, F. Huang, Chem. Soc. Rev. 2015 (1861) 44.

[79] Y. Ma, X. Wang, Y. Jia, X. Chen, H. Han, C. Li, Chem. Rev. 114 (2014) 9987.

[80] M. Kapilashrami, Y. Zhang, Y.-S. Liu, A. Hagfeldt, J. Guo, Chem. Rev. 114 (2014) 9662.

[81] Y. Fu, D. Sun, Y. Chen, R. Huang, Z. Ding, X. Fu, Z. Li, Angew. Chem. Int. Ed. Engl. 51 (2012) 3364.

[82] M. Dahl, Y. Liu, Y. Yin, Chem. Rev. 114 (2014) 9853.

[83] X.D. Jiang, Y.P. Zhang, J. Jiang, Y.S. Rong, Y.C. Wang, Y.C. Wu, C.X. Pan, J. Phys. Chem. C 116 (2012) 22619.

[84] C. Sun, Y. Jia, X.H. Yang, H.G. Yang, X. Yao, G.Q. Lu, S.C. Smith, J. Phys. Chem. C 115 (2011) 25590.

[85] T. Leshuk, R. Parviz, P. Everett, H. Krishnakumar, R.A. Varin, F. Gu, ACS Appl Mater. Interfaces 2013 (1892) 5.

[86] H. Lu, B. Zhao, R. Pan, J. Yao, J. Qiu, L. Luo, Y. Liu, RSC Adv. 4 (2014) 1128.

[87] G. Wang, H. Wang, Y. Ling, Y. Tang, X. Yang, R.C. Fritzmorris, Y. Li, Nano Lett. 11 (2011) 3026.

[88] A. Naldoni, M. Allieta, S. Santangelo, M. Marelli, F. Fabbri, S. Cappelli, V. Dal Santo, J. Am. Chem. Soc. 134 (2012) 7600.

[89] K. Zhang, W. Zhou, X. Zhang, Y. Qu, L. Wang, W. Hu, K. Pan, M. Li, Y. Xie, B. Jiang, G. Tian, RSC Adv. 6 (2016) 50506.

[90] N. Liu, C. Schneider, D. Freitag, M. Hartmann, U. Venkatesan, J. Müller, P. Schmuki, Nano Lett. 14 (2014) 3309.

[91] T. Leshuk, S. Linley, F. Gu, Can. J. Chem. Eng. 91 (2013) 799.

[92] Z. Lu, C.T. Yip, L. Wang, H. Huang, L. Zhou, ChemPlusChem 77 (2012) 991.

[93] A. Sinhamahapatra, J.P. Jeon, J.S. Yu, Energy Environ. Sci. 8 (2015) 3539.

[94] L. Li, Y. Chen, S. Jiao, Z. Fang, X. Liu, Y. Xu, G. Pang, S. Feng, Mater. Des. 100 (2016) 235.

[95] S. Wei, R. Wu, X. Xu, J. Jian, H. Wang, Y. Sun, Chem. Eng. J. 299 (2016) 120.

[96] Y. Zhu, D. Liu, Chem. Commun. 50 (2014) 6049.

[97] M.C. Wu, I.C. Chang, K.C. Hsiao, W.K. Huang, J. Taiwan Inst. Chem. Eng. 63 (2016) 430.

[98] L. Han, Z. Ma, Z. Luo, G. Liu, J. Ma, X. An, RSC Adv. 6 (2016) 6643.

[99] H. Zhang, Z. Xing, Y. Zhang, Z. Li, X. Wu, C. Liu, Q. Zhu, W. Zhou, RSC Adv. 5 (2015) 107150.

[100] L.R. Grabstanowicz, S. Gao, T. Li, R.M. Rickard, T. Rajh, D.J. Liu, T. Xu, Inorg. Chem. 52 (2013) 3884.

[101] S.T. Myung, M. Kikuchi, C.S. Yoon, H. Yashiro, S.J. Kim, Y.K. Sun, B. Scrosati, Energy Environ. Sci. 6 (2013) 2609.

[102] Z. Wang, C. Yang, T. Lin, H. Yin, P. Chen, D. Wan, M. Jiang, Adv. Funct. Mater. 23 (2013) 5444.

[103] F. Teng, M. Li, C. Gao, G. Zhang, P. Zhang, Y. Wang, E. Xie, Appl. Catal. B: Environ. 148 (2014) 339.

[104] Y. Yan, B. Hao, D. Wang, G. Chen, E. Markweg, A. Albrecht, P. Schaaf, J. Mater. Chem. A 1 (2013) 14507.

[105] Y. Yan, M. Han, A. Konkin, T. Koppe, D. Wang, T. Andreu, G. Chen, U. Vetter, J.R. Morante, P. Schaaf, J. Mater. Chem. A 2 (2014) 12708.

[106] G. Panomsuwan, A. Watthanaphanit, T. Ishizaki, N. Saito, PCCP 17 (2015) 13794.

[107] Y. Ishida, W. Doshin, H. Tsukamoto, T. Yonezawa, Chem. Lett. 44 (2015) 1327.

[108] Q. Kang, J. Cao, Y. Zhang, L. Liu, H. Xu, J. Ye, J. Mater. Chem. A 1 (2013) 5766.

[109] H. Tan, Z. Zhao, M. Niu, C. Mao, D. Cao, D. Cheng, P. Feng, Z. Sun, Nanoscale 6 (2014) 10216.

[110] Z. Wang, C. Yang, T. Lin, H. Yin, P. Chen, D. Wan, F. Xu, F. Huang, J. Lin, X. Xie, M. Jiang, Energy Environ. Sci. 6 (2013) 3007.

[111] H. Cui, W. Zhao, C. Yang, H. Yin, T. Lin, Y. Shan, F. Huang, J. Mater. Chem. A 2 (2014) 8612.

[112] J. Zhi, C. Yang, T. Lin, H. Cui, Z. Wang, H. Zhang, F.Q. Huang, Nanoscale 8 (2016) 4054.

[113] T. Lin, C. Yang, Z. Wang, H. Yin, X. Lü, F. Huang, M. Jiang, Energy Environ. Sci. 7 (2014) 967.

[114] J. Xu, G. Zhu, T. Lin, Z. Hong, J. Wang, F. Huang, RSC Adv. 5 (2015) 85928.

[115] S.G. Ullattil, P. Periyat, Nanoscale 7 (2015) 19184.

[116] M.W. Shah, Y. Zhu, X. Fan, J. Zhao, Y. Li, S. Asim, C. Wang, Sci. Rep. 5 (2015) 15084.

[117] S. Chen, J. Tao, H. Tao, C. Wang, Y. Shen, J. Jiang, L. Zhu, X. Zeng, T. Wang, J. Nanosci. Nanotechnol. 16 (2016) 3146.

[118] G. Li, Z. Lian, X. Li, Y. Xu, W. Wang, D. Zhang, F. Tian, H. Li, J. Mater. Chem. A 3 (2015) 3748.

[119] C. Xu, Y. Song, L. Lu, C. Cheng, D. Liu, X. Fang, D. Li, Nanoscale Res. Lett. 8 (2013) 1.

[120] Z. Zhang, M.N. Hedhili, H. Zhu, P. Wang, PCCP 15 (2013) 15637.

[121] H. Li, Z. Chen, C.K. Tsang, Z. Li, X. Ran, C. Lee, B. Pan, J. Mater. Chem. A 2 (2014) 229.

[122] H. Zhou, Y. Zhang, J. Phys. Chem. C 118 (2014) 5626.

[123] L. Zheng, H. Cheng, F. Liang, S. Shu, C.K. Tsang, H. Li, Y.Y. Li, J. Phys. Chem. C 116 (2012) 5509.

[124] B. Chen, J.A. Beach, D. Maurya, R.B. Moore, S. Priya, RSC Adv. 4 (2014) 29443.

[125] J. Dong, J. Han, Y. Liu, A. Nakajima, S. Matsushita, S. Wei, W. Gao, ACS Appl Mater. Interfaces 6 (2014) 1385.

[126] C. Fan, C. Chen, J. Wang, X. Fu, Z. Ren, G. Qian, Z. Wang, Sci. Rep. 5 (2015) 11712.
[127] X. Chen, D. Zhao, K. Liu, C. Wang, L. Liu, B. Li, D. Shen, ACS Appl Mater. Interfaces 7 (2015) 16070.
[128] K. Li, J. Xu, X. Yan, L. Liu, X. Chen, Y. Luo, J. He, D.Z. Shen, Appl. Phys. Lett. 108 (2016) 183102.
[129] T. Nakajima, T. Nakamura, K. Shinoda, T. Tsuchiya, J. Mater. Chem. A 2 (2014) 6762.
[130] H. Huang, H. Zhang, Z. Ma, Y. Liu, X. Zhang, Y. Han, Z. Kang, J. Mater. Chem. A 1 (2013) 4162.
[131] S.G. Ullattil, P. Periyat, J. Mater. Chem. A 4 (2016) 5854.
[132] L. Li, K. Shi, R. Tu, Q. Qian, D. Li, Z. Yang, X. Lu, Chin. J. Catal. 2015 (1943) 36.
[133] J. Duan, H. Hou, X. Liu, C. Yan, S. Liu, R. Meng, Z. Hao, Y. Yao, Q. Liao, J. Porous Mater. 23 (2016) 837.
[134] H.-R. An, S.Y. Park, H. Kim, C.Y. Lee, S. Choi, S.C. Lee, S. Seo1, E.C. Park, Y.-K. Oh, C.-G. Song, J. Won, Y.J. Kim, J. Lee, H.U. Lee, Y.-C. Lee, Sci. Rep. 6 (2016) 29683.
[135] K. Han, X. Zhang, H. Wang, Y. Liu, A. Cao, J. Nanosci. Nanotechnol. 16 (2016) 9823.
[136] M.K. Hossain, A.R. Koirala, U.S. Akhtar, M.K. Song, K.B. Yoon, Chem. Mater. 27 (2015) 6550.
[137] X. Liu, Z. Xing, Y. Zhang, Z. Li, X. Wu, S. Tan, X. Yu, Q. Zhu, W. Zhou, Appl. Catal. B 201 (2017) 119.
[138] M. Ye, J. Jia, Z. Wu, C. Qian, R. Chen, P.G. O'Brien, W. Sun, Y. Dong, G.A. Ozin, Adv. Energy Mater. 7 (2017) 1601811–1601821.
[139] C. Fan, X. Fua, L. Shia, S. Yua, G. Qiana, Z. Wanga, RSC Adv. 6 (2016) 67444.
[140] Z. Tian, H. Cui, G. Zhu, W. Zhao, J. Xu, F. Shao, J. He, F. Huang, J. Power Sources 325 (2016) 697.
[141] C.-C. Wang, P.-H. Chou, Nanotechnology 27 (2016) 325401.
[142] X. Yuan, X. Wang, X. Liu, H. Ge, G. Yin, C. Dong, F. Huang, ACS Appl Mater. Interfaces 8 (2016) 27654.
[143] X. Zhang, J. Wang, W. Hu, K. Zhang, B. Sun, G. Tian, B. Jiang, K. Pan, W. Zhou, ChemCatChem 8 (2016) 1.
[144] J. Zheng, L. Liu, G. Ji, Q. Yang, L. Zheng, J. Zhang, ACS Appl Mater. Interfaces 8 (2016) 20074.
[145] J. Xu, Z. Tian, G. Yin, T. Lin, F. Huang, Dalton Trans. 46 (2017) 1047.
[146] G. Zhu, J. Xu, W. Zhao, F. Huang, ACS Appl Mater. Interfaces 8 (2016) 31716.
[147] C. Burda, Y. Lou, X. Chen, A.C.S. Samia, J. Stout, J.L. Gole, Nano Lett. 3 (2003) 1049.
[148] H. Irie, Y. Watanabe, K. Hashimoto, J. Phys. Chem. B 107 (2003) 5483.
[149] T. Ihara, M. Miyoshi, Y. Triyama, O. Marsumato, S. Sugihara, Appl. Catal. B 42 (2003) 403.
[150] R. Asahi, T. Morikawa, T. Ohwaki, K. Aoki, Y. Taga, Science 293 (2001) 269.
[151] J. Zhang, W. Dang, Z. Ao, S.K. Cushing, N. Wu, PCCP 17 (2015) 8994.
[152] L. Liu, Y.Y. Peter, X. Chen, S.S. Mao, D. Shen, Phys. Rev. Lett. 111 (2013) 065505.
[153] D. Cronemeyer, Phys. Rev. 113 (1959) 1222.
[154] X. Chen, L. Liu, Z. Liu, M.A. Marcus, W.C. Wang, N.A. Oyler, M.E. Grass, B. Mao, P.A. Glans, P.Y. Yu, J. Guo, S.S. Mao, Sci. Rep. 3 (2013) 1510.
[155] P. Raghunath, W.F. Huang, M.C. Lin, J. Chem. Phys. 138 (2013) 154705.
[156] E. Finazzi, C.D. Valentin, G. Pacchioni, A. Selloni, J. Chem. Phys. 129 (2008) 154113.
[157] Z. Wang, B. Wen, Q. Hao, Li-M. Liu, C. Zhou, X. Mao, X. Lang, Wen-J. Yin, D. Dai, A. Selloni, X. Yang, J. Am. Chem. Soc. 137 (2015) 9146.
[158] M.I. Nandasiri, V. Shutthanandan, S. Manandhar, A.M. Schwarz, L. Oxenford, J.V. Kennedy, S. Thevuthasan, M.A. Henderson, J. Phys. Chem. Lett. 6 (2015) 4627.
[159] J.F. Ziegler, J.P. Biersack, M.D. Ziegler, The Stopping and Range of Ions in Matter, (2008) Morrisville, NC.
[160] H. Wang, T. Lin, G. Zhu, H. Yin, X. Lü, Y. Li, F. Huang, Catal. Commun. 60 (2015) 55.
[161] X. Xin, T. Xu, J. Yin, L. Wang, C. Wang, Appl. Catal. B: Environ. 176 (2015) 354.
[162] Z. Zhao, H. Tan, H. Zhao, Y. Lv, L.J. Zhou, Y. Song, Z. Sun, Chem. Commun. 50 (2014) 2755.
[163] J.F. Porter, Y.G. Li, C.K. Chan, J. Mater. Sci. 34 (1999) 1523.
[164] L. Xin, X. Liu, RSC Adv. 5 (2015) 71547.
[165] F. Zuo, L. Wang, T. Wu, Z. Zhang, D. Borchardt, P. Feng, J. Am. Chem. Soc. 132 (2010) 11856.
[166] A. Turković, M. Ivanda, A. Drasner, V. Vranesa, M. Persin, Thin Solid Films 198 (1991) 199.
[167] W.F. Zhang, Y.L. He, M.S. Zhang, Z. Yin, Q. Chen, J. Phys. D: Appl. Phys. 33 (2000) 912.
[168] S.M. Prokes, J.L. Gole, X. Chen, C. Burda, W.E. Carlos, Adv. Funct. Mater. 15 (2005) 161.
[169] W. Li, C. Liu, Y. Zhou, Y. Bai, X. Feng, Z. Yang, L. Lu, X. Lu, K.Y. Chan, J. Phys. Chem. C 112 (2008) 20539.
[170] J. Cai, Y. Wang, Y. Zhu, M. Wu, H. Zhang, X. Li, Z. Jiang, M. Meng, ACS Appl Mater. Interfaces 7 (2015) 24987.
[171] A. Lepcha, C. Maccato, A. Mettenbörger, T. Andreu, L. Mayrhofer, M. Walter, K. Meerholz, J. Phys. Chem. C 119 (2015) 18835.
[172] P.M. Kumar, S. Badrinarayanan, M. Sastry, Thin Solid Films 358 (2000) 122.
[173] S.H. Szczepankiewicz, A.J. Colussi, M.R. Hoffmann, J. Phys. Chem. B 104 (2000) 9842.
[174] P. Jonsen, Colloids Surf. 36 (1989) 127.
[175] H.M. Ruud, J. Chem. Soc., Faraday Trans. 92 (1996) 2791.
[176] P. Jonsen, Catal. Lett. 2 (1989) 345.
[177] M.S. Lazarus, T.K. Sham, Chem. Phys. Lett. 92 (1982) 670.
[178] Z. Zheng, B. Huang, J. Lu, Z. Wang, X. Qin, X. Zhang, Y. Dai, M.H. Whangbo,

[179] J. Pan, G. Liu, G.Q.M. Lu, H.M. Cheng, Angew. Chem. Int. Ed. 50 (2011) 2133.
[180] G. Zhu, T. Lin, X. Lü, W. Zhao, C. Yang, Z. Wang, J. Lin, J. Mater. Chem. A 1 (2013) 9650.
[181] W. Qingli, Z. Zhaoguo, C. Xudong, H. Zhengfeng, D. Peimei, C. Yi, Z. Xiwen, J. CO₂ Util 12 (2015) 7.
[182] M. Zimbone, G. Cacciatoa, R. Sanz, R. Carles, A. Gulino, V. Privitera, M.G. Grimaldi, Catal. Commun. 84 (2016) 11.
[183] X. Lu, A. Chen, Y. Luo, P. Lu, Y. Dai, E. Enriquez, P. Dowden, H. Xu, P.G. Kotula, A.K. Azad, D.A. Yarotski, Nano Lett. 16 (2016) 5751.
[184] W. Zhou, W. Li, J.Q. Wang, Y. Qu, Y. Yang, Y. Xie, D. Zhao, J. Am. Chem. Soc. 136 (2014) 9280.
[185] J.Y. Eom, S.J. Lim, S.M. Lee, W.H. Ryu, H.S. Kwon, J. Mater. Chem. A 3 (2015) 11183.
[186] R. Sanz, L. Romano, M. Zimbone, M.A. Buccheri, V. Scuderi, G. Impellizzeri, M. Scuderi, G. Nicotra, J. Jensen, V. Privitera, J. Appl. Phys. 117 (2015) 074903.
[187] J. Tian, X. Hu, H. Yang, Y. Zhou, H. Cui, H. Liu, Appl. Surf. Sci. 360 (2016) 738.
[188] T. Xia, X. Chen, J. Mater. Chem. A 1 (2013) 2983.
[189] W. Hu, W. Zhou, K. Zhang, X. Zhang, L. Wang, B. Jiang, G. Tian, D. ZhaO, H. Fu, J. Mater. Chem. A 4 (2016) 7495.
[190] Y.J. He, J.F. Peng, W. Chu, Y.Z. Li, D.G. Tong, J. Mater. Chem. A 2 (2014) 1721.
[191] X. Liu, Z. Xing, H. Zhang, W. Wang, Y. Zhang, Z. Li, X. Wu, X. Yu, W. Zhou, ChemSusChem 9 (2016) 1.
[192] K. Shankar, J.I. Basham, N.K. Allam, O.K. Varghese, G.K. Mor, X. Feng, M. Paulose, J.A. Seabold, K.-S. Choi, C.A. Grimes, J. Phys. Chem. C 113 (2009) 6327.
[193] C. Mao, F. Zuo, Y. Hou, X. Bu, P. Feng, Angew. Chem. Int. Ed. 53 (2014) 10485.
[194] B. Qiu, Y. Zhou, Y. Ma, X. Yang, W. Sheng, M. Xing, J. Zhang, Sci. Rep. 5 (2015) 8591.
[195] X. Liu, S. Gao, H. Xu, Z. Lou, W. Wang, B. Huang, Y. Dai, Nanoscale 2013 (1870) 5.
[196] M. Tian, M. Mahjouri-Samani, G. Eres, R. Sachan, M. Yoon, M.F. Chisholm, K. Wang, A.A. Puretzky, C.M. Rouleau, D.B. Geohegan, G. Duscher, ACS Nano 9 (2015) 10482.
[197] S. Tominaka, Inorg. Chem. 51 (2012) 10136.
[198] Y. Zhang, Z. Jiang, J. Huang, L.Y. Lim, W. Li, J. Deng, D. Gong, Y. Tang, Y. Lai, Z. Chen, RSC Adv. 5 (2015) 79479.
[199] M. Ge, C. Cao, J. Huang, S. Li, Z. Chen, K.-Q. Zhang, S.S. Al-Deyab, Y. Lai, J. Mater. Chem. A 4 (2016) 6772.
[200] P. Roy, S. Berger, P. Schmuki, Angew. Chem. Int. Ed. 50 (2011) 2904.
[201] E.M. Samsudin, S.B.A. Hamid, J.C. Juan, W.J. Basirun, A.E. Kandjani, Appl. Surf. Sci. 359 (2015) 883.
[202] M. Ge, J. Cai, J. Iocozzia, C. Cao, J. Huang, X. Zhang, J. Shen, S. Wang, S. Zhang, K.-Q. Zhang, Y. Lai, Z. Lin, Int. J. Hydrog. Energy 42 (2017) 8418.
[203] M. Ge, Q. Li, C. Cao, J. Huang, S. Li, S. Zhang, Z. Chen, K. Zhang, S.S. Al-Deyab, Y. Lai, Adv. Sci. 4 (2017) 1600152.
[204] B. Wang, S. Shen, S.S. Mao, J. Materiomics 2 (2017) 96.
[205] L. Shen, Z. Xing, J. Zou, Z. Li, X. Wu, Y. Zhang, Q. Zhu, S. Yang, W. Zhou, Sci. Rep. 7 (2017) 41978.
[206] M. Coto, G. Divitini, A. Dey, S. Krishnamurthy, N. Ullah, C. Ducati, R.V. Kumar, Mater. Today Chem. 4 (2017) 142.
[207] N. Liu, H.-G. Steinrück, A. Osvet, Y. Yang, P. Schmuki, Appl. Phys. Lett. 110 (2017) 072102.
[208] Y. Zhang, Z. Xing, J. Zou, Z. Li, X. Wu, L. Shen, Q. Zhu, S. Yang, W. Zhou, RSC Adv. 7 (2017) 453.
[209] C. Yang, Z. Wang, T. Lin, H. Yin, X. Lü, D. Wan, X. Xie, J. Am. Chem. Soc. 135 (2013) 17831.
[210] N. Liu, V. Häublein, X. Zhou, U. Venkatesan, M. Hartmann, M. Mackovic, T. Nakajima, E. Spiecker, A. Osvet, L. Frey, P. Schmuki, Nano Lett. 15 (2015) 6815.
[211] B. Li, Z. Zhao, Q. Zhou, B. Meng, X. Meng, J. Qiu, Chem-Eur J. 20 (2014) 14763.
[212] B. Yan, P. Zhou, Q. Xu, X. Zhou, D. Xu, J. Zhu, RSC Adv. 6 (2016) 6133.
[213] J. Zhao, Y. Li, Y. Zhu, Y. Wang, C. Wang, Appl. Catal. A: Gen. 510 (2016) 34.
[214] K. Carlson, C. Elliott, S. Walker, M. Misra, S. Mohanty, J. Electrochem. Soc. 163 (2016) H395.
[215] X. Xin, T. Xu, L. Wang, C. Wang, Sci. Rep. 6 (2016) 23684.
[216] C. Zhang, Y. Xie, J. Ma, J. Hu, C. Zhang, Chem. Commun. 51 (2015) 17459.
[217] S.G. Ullattil, A.V. Thelappurath, S.N. Tadka, J. Kavil, B.K. Vijayan, P. Periyat, Sol. Energy 155 (2017) 490.
[218] T. Xia, W. Zhang, W. Li, N.A. Oylera, G. Liu, X. Chen, Nano Energy 2 (2013) 826.
[219] T. Xia, W. Zhang, J. Murowchick, G. Liu, X. Chen, Nano Lett. 13 (2013) 5289.
[220] T. Xiaa, W. Zhangb, Z. Wang, Y. Zhanga, X. Song, J. Murowchick, V. Battaglia, G. Liu, X. Chen, Nano Energy 6 (2014) 109.
[221] J. Bae, D.S. Kim, H. Yoo, E. Park, Y.G. Lim, M.S. Park, Y.J. Kim, H. Kim, ACS Appl Mater. Interfaces 8 (2016) 4541.
[222] J. Chen, Z. Ding, C. Wang, H. Hou, Y. Zhang, C. Wang, G. Zou, X. Ji, ACS Appl Mater. Interfaces 8 (2016) 9142.
[223] A.L.M. Reddy, S. Ramaprabhu, J. Phys. Chem. C 111 (2007) 7727.
[224] C. Kim, S. Kim, J. Lee, J. Kim, J. Yoon, ACS Appl Mater. Interfaces 7 (2015) 7486.
[225] Y. Shan, Y. Yang, Y. Cao, H. Yin, N.V. Long, Z. Huang, RSC Adv. 5 (2015) 34737.
[226] W. Ren, Y. Yan, L. Zeng, Z. Shi, A. Gong, P. Schaaf, D. Wang, J. Zhao, B. Zou, H. Yu, G. Chen, E.M.B. Brown, A. Wu, Adv. Healthcare Mater. 4 (2015) 1526.
[227] J. Mou, T. Lin, F. Huang, H. Chen, J. Shi, Biomater. 84 (2016) 13.
[228] Y. Kim, H.M. Hwang, L. Wang, I. Kim, Y. Yoon, H. Lee, Sci. Rep. 6 (2016) 25212.

Chem. Commun. 48 (2012) 5733.

Dr. Sanjay Gopal Ullattil received his PhD in Chemistry (2017) from the Department of Chemistry, University of Calicut, Kerala, India under the supervision of Dr. Pradeepan Periyat. Currently he is working as an assistant professor at the Department of Nanoscience and Technology in the same University. He is an author of 10 international publications and 3 book chapters and is a professional member of the international associations such as Young International Solar Energy Society (ISES) and International Association of Advanced Materials (IAAM). His current research interests are novel materials for energy conversion, storage and environmental remediation.

Dr. Soumya B. Narendranath obtained her Ph.D. degree in 2016 from CSIR-National Chemical Laboratory (NCL), Pune, where she studied photocatalytic water splitting activity of layered metal oxides. She received National Post Doctoral Research Fellowship (NPDF) from DST-SERB, Govt. of India, and currently she is continuing her research as NPDF in the Department of Chemistry, Central University of Kerala. Her research interests include design and development of metal oxide nanoparticles for solar energy utilization and its mechanistic studies.

Prof. Suresh C. Pillai obtained his PhD in the area of Nanotechnology from Trinity College Dublin and then performed postdoctoral research at California Institute of Technology (Caltech), USA. Upon the completion of this appointment he returned to Trinity College Dublin as a Research Fellow before joining CREST-DIT as a Senior Research Manager in April 2004. Suresh joined IT Sligo as a Senior Lecturer in Nanotechnology in October 2013. He is an elected fellow of the UK's Royal Microscopical Society (FRMS) and the Institute of Materials, Minerals and Mining (FIMMM). Suresh was responsible for acquiring more than €4 million direct R&D funding. He has published several scientific articles in leading peer reviewed journals and has presented papers in several international conferences. He has delivered over fifty international invited talks including several key-note and plenary talks. His research work was featured in the BBC London, BBC World Radio, Times UK, 'The Investigators (RTE TV)' programme, RTE-1 TV News, Aljazeera TV, Ocean FM Radio and a number of national and international news media. He was also the recipient of the 'Hothouse Commercialisation Award 2009' from the Minister of Science, Technology and Innovation and also the recipient of the 'Enterprise Ireland Research Commercialization Award 2009'.

Dr. Pradeepan Periyat currently working as an Assistant Professor, Department of Chemistry, University of Calicut, Kerala, India. He completed PhD from Dublin Institute of Technology, Ireland under the supervision of Prof. Suresh Pillai and Prof. Declan McCormack. He completed two post-doctoral fellowship at University of Limerick, Ireland and Monash University, Melbourne, Australia. He was awarded the prestigious Marie-Curie Fellowship from 2009 to 2012. He is an Associate Member of Royal Society of Chemistry (RSC), London. He received the Young Scientist Award-2017 from Kerala State Government Council for Science, Technology and Environment. He has published 40 scientific articles in leading peer reviewed journals, ten book chapters, presented in several national and international conferences and delivered many invited talks. His research group focuses on the synthesis, characterisation and applications of semiconductor nanomaterials for dye sensitised solar cells, photocatalysis, battery, electrochromic applications *etc*.